Investigations of Equatorial F-region plasma instabilities under different background conditions

A THESIS

submitted for the Award of Ph.D degree of

Mohan Lal Sukhadia University

in the

Faculty of Science

BY

Esfhan Alam Kherani

Thesis-in-charge

Ramanathan Sekar
Reader, Physical Research Laboratory

Department of Planatory Atmosphere and Aeronomy
PHYSICAL RESEARCH LABORATORY, AHMEDABAD.

MOHANLAL SUKHADIA UNIVERSITY, UDAIPUR

Year of submission: 2001

Submitted on: 24 May 2001

CERTIFIED that the work incorporated in the thesis

Investigations of Equatorial F-region plasma instabilities under different background conditions

submitted by **Esfhan Alam Kherani** was carried out by the candidate under my guidance at the Physical Research Laboratory, Ahmedabad. The work presented in this thesis is original and has not formed basis for the award of any degree or diploma by any university or institution.

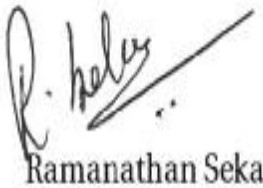

Ramanathan Sekar
(Thesis-in-charge)

And walk not on the earth with conceit and arrogance. Verily, you can neither rend nor penetrate the earth, nor can you attain a stature like the mountains in height.

Contents

Acknowledgment iii

1 Introduction 1
- 1.1 Ionosphere as a partially ionized plasma . . . 1
  - 1.1.1 Chemical processes in E and F region . . . 1
  - 1.1.2 Transport processes . . . 2
- 1.2 Plasma instabilities in the ionosphere . . . 4
  - 1.2.1 F region plasma instabilities or Equatorial Spread F (ESF) . . . 4
  - 1.2.2 Macroinstability processes for ESF . . . 5
  - 1.2.3 Generalized RT (GRT) instability . . . 6
  - 1.2.4 Nonlinear stage of CRT instability . . . 7
  - 1.2.5 Microinstability processes and 3-m scale size irregularities . . . 8
  - 1.2.6 Variabilities in ESF . . . 9
- 1.3 Objective and outline of the thesis . . . 10
- 1.4 Figure captions . . . 11

2 Effects of molecular ions on the GRT instability: Linear analysis 12
- 2.1 Introduction . . . 12
- 2.2 The steady state current density and electron scale height for two ions-electron plasma . . . 12
  - 2.2.1 The zonal current density . . . 12
  - 2.2.2 The plasma scale heights in two ions-electron plasma . . . 13
- 2.3 First order perturbation analysis of GRT instability in two ions-electron plasma . . . 14
  - 2.3.1 The comparison of growth rates of CRT instability for two ions-electron and one ion-electron plasma . . . 20
  - 2.3.2 The cause for the reduction of the growth rate . . . 21
  - 2.3.3 The comparison of growth rate with damping rate . . . 23
  - 2.3.4 The comparison of time scale associated with instability and life time of both the ions . . . 24
- 2.4 Role of Fe^+ ions . . . 25
- 2.5 Summary and Conclusion . . . 26
- 2.6 Figure captions . . . 27

3 Effects of molecular ions on the GRT instability : Nonlinear evolution 28
- 3.1 Numerical simulation model . . . 28
  - 3.1.1 Set of equations . . . 28
  - 3.1.2 The simulation plane . . . 30

3.1.3 The boundary conditions and initial conditions . . . 30
3.1.4 The numerical scheme . . . 31
3.1.5 The inputs for simulation . . . 31
3.1.6 The form of initial perturbation . . . 31
3.1.7 Cases considered for investigation . . . 32
3.2 Results corresponding to case 1 . . . 32
3.3 Discussion . . . 34
3.3.1 The upwelling structures as O^+ depletions or bubbles . . . 34
3.3.2 The upwelling structures as NO^+ enhancement . . . 35
3.3.3 Transport process vs. chemical process . . . 36
3.3.4 Modified polarization velocity in the presence of NO^+ ions . . . 39
3.3.5 The importance of O^+ scale height below the base . . . 41
3.3.6 Investigations with other cases . . . 41
3.4 Summary and conclusion . . . 43
3.5 Figure captions . . . 43

4 The radar observations of 2.8m scale size irregularities associated with ESF 45
4.1 Introduction . . . 45
4.2 Principle of radar and System Description . . . 45
4.2.1 Principle of radar . . . 45
4.2.2 system Description . . . 46
4.2.3 Data processing . . . 47
4.3 General features . . . 48
4.3.1 Morphology of ESF . . . 48
4.3.2 Day-to-day variabilities . . . 49
4.3.3 Vertical erect and tilted plume structures . . . 50
4.3.4 The topside electron density . . . 50
4.3.5 The absence of backscatter in the valley region . . . 50
4.3.6 The Doppler velocities . . . 51
4.3.7 ESF event of 23 march, 99 . . . 55
4.3.8 Late emergence of plume . . . 55
4.3.9 The bottomside ESF event . . . 56
4.4 summary and conclusion . . . 56
4.5 Figure captions . . . 57

5 The simulation of multiwavelength morphology and downwelling of plasma bubbles 58
5.1 Introduction . . . 58
5.2 Numerical simulation model . . . 59
5.2.1 The simulation plane . . . 59
5.2.2 The boundary conditions and initial conditions . . . 59
5.2.3 The numerical scheme . . . 60
5.2.4 The inputs for simulation . . . 60
5.2.5 The form of initial perturbation . . . 60
5.2.6 Cases considered for investigation . . . 60
5.2.7 Method of illustrations . . . 60
5.3 The general features of interaction of two wave modes . . . 61
5.3.1 Results . . . 61

5.3.2 Discussion 62
5.4 A case study 65
5.5 summary and conclusion 67
5.6 Figure captions 67

Conclusions and Future Outlook **69**

Acknowledgment

I deeply acknowledge all my batch mates, hostel mates for their unforgettable cooperation during my non-academic troubles over last one year, which otherwise would have affected my academics a lot. I acknowledge my teachers, Dr. Supre and Prof. Thakur, who motivated me to do research. I deeply acknowledge Prof. A.C. Das, Prof. Prasanna, Prof. Sridharan, Prof. Raghavarao, Prof. Agarwal and Dr. Sekar for their efforts to keep my academic carrier alive. The deep knowledge of Prof. Prasanna, Dr. Jitash Bhatt, Dr. Sekar, Prof. P.B. Rao and Prof. Raghavarao on plasma astrophysics and ionospheric physics made me to learn some thing from them during the research. I deeply acknowledge my seniors Gautam, Devashish, Ramachandran, Sivakumaran Jyoti and Tarun pant for their valuable advises and constant encouragement over last five years.

Esfhan Alam Kherani

Chapter 1

Introduction

1.1 Ionosphere as a partially ionized plasma

The Earth's ionosphere is a partially ionized plasma that envelops the earth and in some sense forms the interface between the atmosphere and space. The electron number density is sufficient to affect the radio wave propagation but still three to five order less than the neutrals. One needs to have knowledge of both atmospheric dynamics and space plasma physics to understand various ionospheric processes. The existence of charge particles is mainly due to the photo-ionization of neutrals by solar UV radiation and energetic particle impact on neutrals. The latter is important at high latitudes whereas former is the important mechanism over the equator and low latitudes. Its not only the ionization which decides the existence of plasma , but its the chemical and transport processes which also play decisive roles in the ionosphere. All the three mechanisms control the dynamics of the plasma in the ionosphere. Their relative strength considerably varies depending on the altitudes, latitudes, local time, seasons and solar activity. The equatorial, mid-latitude and high-latitude ionosphere exhibit different phenomenon which have been monitored through radar, optical measurements and *in-situ* probes. The present investigation deals with some interesting aspects of equatorial ionosphere.

The radio sounding experiments reveal that the equatorial ionosphere is organized into the layered structure over the thermospheric altitudes. These layers are termed as E and F regions of the ionosphere and arises due to the varying strength of three processes mentioned above. In the E region, the chemical processes dominate over transport processes whereas in the F region, reverse situation takes place. The dominant transport processes in the F region cause the electron density to be maximum there. It is to be emphasized that both the processes not only decide the electron density (or total ion density) but also the ion composition. Its therefore worth in this stage to discuss the chemical and transport processes in E and F region.

1.1.1 Chemical processes in E and F region

The dominant neutral composition O_2 and O in E and F regions respectively are photoionized by solar UV-EUV radiation and gives corresponding ions in E and F regions.

$$O_2 + h\nu \rightarrow O_2^+ + e^-$$
$$O + h\nu \rightarrow O^+ + e^-$$

However the primary atomic ion, O^+, undergoes charge-exchange process further causing the secondary ions:

$$O^+ + O_2 \xrightarrow{\beta} O_2^+ + O,$$
$$O^+ + N_2 \xrightarrow{\beta} NO^+ + N,$$

Here β is the reaction rate. The primary molecular ion, O_2^+, and secondary molecular ions, O_2^+, NO^+, are lost by dissociative recombination with electrons:

$$O_2^+ + e \xrightarrow{\alpha} O + O$$
$$NO^+ + e \xrightarrow{\alpha} O + N,$$

The reaction rate of these reactions is defined as αn_e where n_e is the electron density. The life time of the ions which are taking part in either of the reactions is just the reciprocal of the corresponding reaction rate. It is obvious that the charge-exchange mainly alters the composition but not the total ion density while the dissociative recombination alters both. Its also evident that the molecular ions (O_2^+, NO^+) are dominated in the E region where neutral molecules, N_2 and O_2, are dominant while the atomic oxygen (O^+) ions dominate in the F region. However, during evening hours, the dominant NO^+ ions are often seen up to the base of the F region [10, 63, 95]. Anderson and Rusch [3] brought the importance of transport along with the following reaction :

$$O_2^+ + N(^4S) \rightarrow NO^+ + O \tag{1.1}$$

to explain such observations. We will discuss this aspect more elaborately in next section.

1.1.2 Transport processes

The ionospheric plasma being a partially ionized plasma exhibits distinct interesting behaviour compared to fully ionized plasma. The low ion density compared to neutrals make coulombic collisions less effective than elastic collisions of particles with neutrals. Moreover these collisions, unlike in fully ionized plasma, are binary in nature which greatly alters the transport processes in ionospheric plasma. Unlike in the fully ionized plasma, the normal and ambipolar diffusions processes occur in ionospheric plasma. On the other hand the electric field can be developed in ionospheric plasma similar to the fully ionized plasma if finite non-divergence current flows. The transport processes in the ionospheric plasma can be realized with the existence of driving forces such as mechanical and electromagnetic forces and by the existence of any gradient in the basic plasma fluid quantities. The mechanical force includes the gravitational force $\vec{g}$ and drag force $\nu_{in}\vec{W}$ by neutral winds ($\vec{W}$) where ν_{in} is the ion- neutral collision frequency. The response to all these forces are valued by mobility tensor (μ) which is anisotropy in nature owing to the existence of Earth's magnetic field (B). It has component parallel to B, perpendicular to B but parallel to driving forces and perpendicular to both B and forces which are named respectively as Direct, Pedersen and Hall mobility.

$$\mu_{a0} = \frac{q_a}{m_a \nu_{an}} \tag{1.2}$$

$$\mu_{aP} = \mu_{a0} \frac{\nu_{an}^2}{\nu_{an}^2 + \omega_a^2} \tag{1.3}$$

$$\mu_{aH} = \mu_{a0} \frac{\nu_{an}\omega_a}{\nu_{an}^2 + \omega_a^2} \tag{1.4}$$

Here 'a' stands for ions and electrons, q_a, m_a are corresponding charge and mass and ω_a, ν_{an} are corresponding gyrofrequency and collision frequency with neutrals. The conductivity (σ) and diffusion (D) tensors are defined as:

$$\sigma = \sum_a n_a q_a \mu_a, \quad D = \sum_a \frac{kT_a}{q_a} \mu_a$$

here 'k' is the Boltzmann constant and T_a is the temperature of species 'a' .
Over ionospheric altitudes, the direct conductivity is much larger than the other two. Its large value prevents the generation of any potential difference along the field lines making it to be equipotential lines. The relative strength of Pedersen and Hall conductivity depends mainly on the ratio of gyro to collision frequency, (k_a), which vary with altitudes for both ions and electrons. In E region $k_i < 1$ while $k_e > 1$ so that the dominant conductivity is Hall conductivity and current is mainly driven by electrons owing to their highly magnetized nature. In F region both the ratios are greater than one so that the dominant conductivity is Pedersen and current is mainly driven by ions owing to their large mass.

Generation of electric field

The currents in both E and F regions are not merely flowing $\perp$ to B, but also varies considerably over the altitudes either due to the variations in conductivities or spatially varying driving forces or both. The electric field is what it builds up vary quickly in response to any divergence of $\vec{J}$. When an electric field is created by winds or tides blowing across the B, the process is often called the dynamo. The E and F regions are linked by the highly conducting field lines and depending on the relative conductivities, one acts as generator and another acts as load. Owing to its large conductivities during daytime, the E region acts as generator and F region acts as load. The global electric filed generated by global tides in the E region then mapped to the F region from off-equatorial E region. Such mapped field has both vertical and zonal components causing F region plasma to move as a whole with $\frac{\vec{E}\times\vec{B}}{B^2}$ velocity in zonal and vertical direction respectively. Such ionospheric movements have been observed by means of incoherent scatter radar [108, 18] and HF Doppler radar [62, 46]. Though, the zonal drift is found to be much larger than the vertical drift, the latter play a vital role in restructuring and redistributing the plasma owing to the vertical gradients exist in the ionosphere. The vertical F region plasma drift becomes very large during postsunset time. Such enhanced transport brings O_2^+ and NO^+ from E region to F region heights where O_2^+ converts into NO^+ by reaction 1.1 [3]. Such effects causes existence of considerable NO^+ ions up to the base of the F region [3] as frequently observed.

The comparative study of chemical and transport processes reveals that the former process dominate in the E region whereas latter process dominates in the F region. In the nighttime, E region is eaten away by recombination while the F region is maintained by transport process like diffusion and vertical drift. The steep positive plasma density gradient is what is created on the bottomside of F region which offer the generation of interchange instability well known in plasma physics [11, 94].
In brief the ionosphere is a natural plasma laboratory, organized in certain density structure, allows flow of currents and generation of electric fields, allows normal and ambipo-

lar diffusions, offer plasma instabilities and lot more.

1.2 Plasma instabilities in the ionosphere

Like astrophysical and lab plasma, the ionospheric plasma possesses the inhomogeneities and dc electric field and offers plasma instabilities to grow under suitable conditions. The wave-like structures in density and electric fields are frequently observed by various measurements. The considerable development in the radar observation has made it possible to investigate these instabilities great in depth. The instabilities can be grouped under E region plasma instability and F region plasma instability. These plasma instability processes are extensively discussed in the literature [50]. Both E and F region instability processes are equally of interest however in present thesis some of the interesting aspects of F region plasma instabilities are dealt.

1.2.1 F region plasma instabilities or Equatorial Spread F (ESF)

Plasma instability phenomenon occurring in the equatorial F region ionosphere are grouped under the generic name Equatorial Spread F (ESF). This stems from the earliest observations using ionosondes [8], which showed that on occasion the reflected echo did not display a well behave pattern but was spread in range or frequency. The phenomenon occurs primarily at night, although isolated day time events occur [110]. In the early 1970s, grey-scale radar maps came into vogue as a method of following the position and intensity of ESF plasma density irregularities. The probing MHz frequencies are backscattered from the fluctuations having meter scale size and amplitude much larger than the thermal fluctuations. The RTI (Range-Time-Intensity) maps by coherent radar observation [109, 100, 101, 45, 42, 68, 69] often reveal the amplitude modulation of bottomside backscatter (AMBB) and towering plume structures which penetrate to topside. Although the high-altitude excursion of structured plasma are certainly spectacular, there is ample evidence that the process begins at low altitudes [55, 17, 100, 103]. Several rockets and satellites have now penetrated both the irregularity layers and the plume structures. The plume structures are collocated with density depletions [75, 98, 103]. Moreover the depleted regions are elongated along the direction of the magnetic field for hundreds of kilometers [105, 99]. The *in situ* plasma drift detector reveal that the plasma inside the bubble moves upward with hundreds of meter per second velocity [60, 47, 4]. Occasionally the bubble uprise velocities are found to be more than 1 km/s [1, 42]. The power spectrum [49, 42, 43] reveal that spread F related turbulent structures occur over seven orders of magnitude in spatial scale, from more than 10^5 m to less than 0.1 m. It exhibits two regions that obey k^{-n} scaling, where n is approximately equal to 2 at wavelengths greater than 80-100 m and approximately equal to 5 at shorter wave lengths.
In order to explain different aspects of ESF, the linear and nonlinear theories are proposed over last 30 years. Dungey [16] was first to proposed the gravitational Rayleigh-Taylor (RT) instability as the process driving ESF. The observation over Jicamarca [17] puts the proposed theory and many other theories under suspicion as they fail to explain the observed feature mainly the observed irregularities both on bottom and top

side. Moreover though the turbulent spectrum follows the negative power law index like neutral turbulence, the mechanism is thought not to be just the cascading of large scale to smaller scale structures. It was Haerendel [25] who suggested that the ESF is driven by a hierarchy of multi-step plasma processes involving macroinstability processes such as collisional RT **(CRT)** , EXB and microinstability processes like drift wave instability processes. The CRT instability being a initiative mechanism causes the generation of large scale **plasma depletions (bubbles)** having steep plasma boundaries. The microinstabilities like gradient driven plasma instabilities could be excited on such walls and responsible for the turbulent spectrum. The scenario is similar to what one encounter in the astrophysical plasma and we now discuss these macro-microinstability processes one after another in the perspective of the ionospheric plasma. Both the macro and micro instability processes arises due to the inhomogeneity and the currents which act as sources of free energy in the ionospheric plasma. However the scales at which they operate are different and one need to adopt different approach (fluid or kinetic) to analyze them.

1.2.2 Macroinstability processes for ESF

The gravitational Rayleigh-Taylor (RT) instability named also as the interchange instability [94] is being known in fully ionized plasma for long time. The condition for the generation of this instability is:

$$\vec{g}.\nabla n \; < \; 0$$

which is also applicable in weakly ionized plasma like ionospheric plasma. Here 'n' is the plasma density. Moreover one need to take finite collisions into account for the generation of RT instability in weakly ionized plasma which is named as collisional RT (CRT) instability. In the F region of ionosphere, upward plasma density gradient exists on the bottomside. Near the equator, where Earth's magnetic field helps to support the plasma against gravity, both collisional and collisionless RT instabilities can then be excited on the bottomside. However, conditions are ideal just after sunset, when recombination simultaneously reduces the conductivity of the end plates in the E region and steepens the upward directed density gradients. If the density inhomogeneity and the gravity have component perpendicular to the B($\| \hat{b}$), then ions and electrons acquire drifts :

$$\vec{V}_{da} = \frac{v_{tha}^2}{\Omega_a} \frac{\nabla n_a}{n_a} \times \hat{b}$$

$$\vec{V}_{ga} = \frac{\vec{g}}{\Omega_a} \times \hat{b}$$

where a stands for ions and electrons and v_{tha}, Ω_a are corresponding thermal velocity and gyrofrequency. Though both drifts give finite current ($\vec{J}$) in the ionosphere but the first one doesn't produce any electric field as the divergence in $\vec{J}$ is always perpendicular to the gradient itself [50]. However it plays an important role in the generation of microinstabilities where the free energy is dissipated in different way. Its obvious that the current driven by gravity is in the zonal direction and mainly carried by ions. When there is perturbation (say sinusoidal) along the zonal direction, then finite divergence in $\vec{J}$ causes the generation of polarization electric field E_p. In the collisional limit the field is sustained by collisions while in collisionless limit it is sustained by ion inertia. The less density (depletion) plasma then moves upward with $\vec{v}_p = \frac{\vec{E}_p}{B} \times \hat{b}$ velocity to achieve a uniform

state of thermodynamic equilibrium. However at the same time the plasma is extracted from it at the rate of $v.\frac{\nabla n}{n}$ since gradient is upward. Thus the depleted volume gets more depleted with time and instability sets in. Meanwhile the shape of the bubble also gets distorted. If one start with two dimensional circular bubble then since initial flow is in vertical direction, the bubble gets elongated in that direction. At later time it gets more and more elongated as the degree of depletion and so the vertical flow increases. When bubble reaches at the F_{peak} altitude, it is still less than the plasma above that altitude and continue to rise though the density gradient above that altitude is downward. The rising bubble travels through both collisional (lower altitudes) and collisionless regime (higher altitudes) which are defined as [67]:

$$\text{Collisional region} : \nu_{in}^2 \gg \frac{g}{L}$$
$$\text{Collisionless region} : \nu_{in}^2 \ll \frac{g}{L}$$

where ν_{in} is the ion-neutral collision frequency and L is the plasma scale height. The growth rates in these regime are respectively given by [22, 77, 67]:

$$\gamma_{col} = \frac{g}{\nu_{in} L}$$
$$\gamma_{in} = \sqrt{(\frac{g}{L})}$$

and these modes propagate perpendicular to the magnetic field, in the zonal direction with the phase velocity:

$$\frac{\omega}{k_\perp} = \frac{g}{\Omega_i}$$

Although quite simple, the treatment offers explanations for a number of properties of ESF. First, in the initial development of spread F there is a strong tendency for VHF radar to obtain echoes confined to the height range where the density gradient is upward [109, 100, 103]. It is in this region where the liner theory predicts the instability. Another feature predicted by the theory is a height dependence for γ_{col} due to ν_{in}. The higher the F layer, large the growth rate. Farley et al [17] and Jaychandran et al [46] noted a strong tendency for ESF to be generated when the layer was at a high altitude consistent with the theory.

1.2.3 Generalized RT (GRT) instability

The sources of free energy for the generation of GRT instability are the zonal current and the upward gradient in the density. In the F region, there are forces like electric field and winds other than gravity, which can also drive the significant zonal currents. If the electric field is the driving force for currents then the instability is called $E \times B$ instability [92]. The effect of wind driven currents can be taken account just by replacing the electric field in the rest frame to the neutral frame. The electric field usually drives the Pedersen current in the ionosphere while the neutral wind drives currents perpendicular to itself. Thus the zonal electric field [29] and vertical neutral winds [82] can excite the instability. The instability resulting from all three forces, $\vec{g}$, $\vec{E}$, $\nu_{in}\vec{W}$, is called the *Generalized*

Rayleigh-Taylor instability and the corresponding growth rate expression is [82]:

$$\gamma_{GRT} = \frac{1}{L}\left(\frac{g}{\nu_{in}} + \frac{E}{B} + W\right) \tag{1.5}$$

The zonal electric field at the equator often increases to a large eastward value after the sunset, driving the F layer to very high altitude. This uplift contributes in two ways to the destabilization of the plasma. Not only is the electric field is in the right direction for the instability, but also the g/ν_{in} in term becomes large due to the high altitude of the layer.

1.2.4 Nonlinear stage of CRT instability

The nonlinear stage of CRT instability proposed by Haerendel [25] has been verified by various numerical simulation models over the years [81, 66, 71, 33]. The plasma bubbles are indeed seen on the topside with very large velocities and having their origin on the bottomside. The simulations [52, 114] have also been used to predict the power spectrum of the density structures for comparison with experiments. The simulation [114] shows a very strong anisotropy in the development of the irregularities, with nearly sinusoidal structures developing horizontally and shock-like structures in the direction of ∇n. The shock-like structures or steepening is a consequence of plasma advection and occurs on the vertical (up-down) leading edges of depletion wedges. The predicted waveforms and their spectra are in excellent agreement with the experiments at intermediate scales (10 km - 100 m). The simulation of steepened structures is the verification of the earlier observation [14] and the recent observation [43]. These observations reveal that the nighttime F region is characterized by propagating steepened structures. One of the most remarkable features of equatorial spread F is that the plasma structuring it creates seems to exhibit a degree of self-similar scale invariance. That is, the small-scale structuring is reminiscent in form of the large-scale structuring and of the structuring at all scales in between. The scale variance is one of the signatures of inertial range turbulence in neutral gases. However there are subtle differences between turbulence associated with spread F and the neutral turbulence. The preferred direction of plasma advection in spread F makes the turbulence to be highly anisotropic and inhomogeneous. Most importantly, one can not regard the phases of the modes that compose spread F irregularities to be random since the irregularities take the form of distinct, coherent, steepened structures as observation indicates [14]. The steepened structures with scale as small as 80 m are observed [14]. Thus the intermediate scale CRT instability process could give rise steep structures which descend from large scale to scale as short as 100 m by following the power spectrum with n $\approx$ -2. Its not only the power index which favours the CRT instability as the mechanism for turbulence above 100 m, but its the simultaneous density and electric field power spectrum measurements [59, 43] which also favours it. This measurement reveal that unlike the density power spectrum, the electric field spectrum doesn't show any break near 100 m but have n $\approx$ -2.5 nearly same as density power spectrum irrespective of the wavelength. Under the CRT instability process, the electric field fluctuation, δE, is related to density fluctuation, δn, by relation:

$$\delta E = -\left(\frac{gB}{\nu_{in}}\right)\frac{\delta n}{n}$$

Hence the power spectrum of the two quantities, δE and δn, predicted by CRT instability induced turbulence is same which indeed is what observations reveal.

1.2.5 Microinstability processes and 3-m scale size irregularities

The hierarchy model [25] suggests that the growth of long wavelength instabilities, macroinstabilities, produces density gradients (steepened structures) upon which shorter wavelength microinstability like drift instabilities arise. These enhanced micro fluctuations scatter particles and lead to wave-particle dissipation that can rapidly remove energy from the longer wavelength modes and may cause the steep power spectra in shorter wave length region. The VHF radar, which is extensively used for the study of ESF phenomenon mainly detect the small scale size irregularities though it also reveal the features of the long and intermediate wavelengths. The interchange instability gets stabilize at small scales owing to the classical perpendicular diffusion. A problem recognized early in the study of ESF involves the generation of small-scale irregularities. Some early theoretical research focused on the possible role of the drift instability as a primary process generating short-scale irregularities [41]. In this picture the drift instability grows on the zero-order density gradient in the unstable ionosphere. At long wavelength, λ. the growth of the irregularities is dominated by the CRT mode, but at short wavelength the CRT process is inefficient and the dominant growth rate might be due to the drift instability. They investigated a collisional drift mode and found that there may exist a subrange in which the drift mode acts as a primary process; however, even the primary drift instability would not be unstable at 3 m. Chaturvedi and Kaw [12] worked out the nonlinear physics and determined that a secondary drift wave mode cannot grow on a primary drift wave since the mode-mode coupling for such a process is very weak. Thus they concluded that the important process in ESF is the generation of large scale irregularities by the CRT process followed by the excitation of drift waves on the gradients associated with the primary process.

A variety of drift wave modes may or may not be excited as a secondary process in ESF. Among these are the high-frequency drift cyclotron mode and lower hybrid drift mode, which have been invoked to explain the very short wavelength structure observed with Altair and Tradex radars [37]. Huba and Ossakow [38, 40] have shown these modes to be stable in most conditions except for very low densities and relatively high altitudes for which ion-neutral collisions are unimportant.

Among the low frequency drift waves there exist collisional (resistive) drift wave modes as well as the collisionless (universal) mode. Most of the low frequency drift wave modes have finite wavelength parallel to the B; therefore since the electrons are free to move along B, the drift wave density irregularities (δn) must be supported by a perturbed electric field ($-\nabla\phi$), which to first order is governed by the Boltzmann relation in low frequency domain ($\omega < \Omega_i$):

$$\frac{\delta n}{n} = \frac{e\phi}{K_b T_e} \tag{1.6}$$

In the collisionless plasma such polarization field would not sustained and corresponding instability is universal drift instability [14, 15] mainly driven by electrons owing to their larger diamagnetic drift. However if collisions are significant then the polarization field would be created causing another mode of instability called collisional density drift instability [23]. The major difference between these two low frequency wave modes are that the collisions stabilizes the former but destabilize the later. Costa and Kelley [15] argue that there is a regime in altitude and wavenumber for which the universal drift instability should play an important role in the ionosphere.

In general, the drift instabilities act to destroy the free energy source that drive them i.e., the density gradient by anomalous diffusion of plasma across the B. While describing the power spectra one need to take the proper diffusion into account. In hierarchy of small-scale irregularities responsible for the radar backscatter measurements, the smaller the irregularity size, the steeper the density gradient scale length required to support it. Since the time scale associated with any diffusion process is $\tau_D \approx \lambda^2/D$ (λ is scale length and D is the diffusion coefficient), the shortest density gradient scale lengths diffuse away first. Thus, one would expect the smallest scale irregularities to disappear first in the decay phase of ESF and this, in fact, seems to be the case [5, 6]. By using the anamolous diffusion for universal drift instability mechanism derived by Gary [21], Bernhardt et al [7] have produced the power spectrum with $n \geq 4$ consistent with the observations. From equation (1.6) it follows that the drift wave induced electric fluctuations spectrum should have n value smaller by 2 of the density fluctuations n value i.e.; it is less steepen than the density spectrum which is indeed the case as pointed out earlier. Its interesting to note that the diffusion induced fluctuations also follow the similar relation between δn and δE as drift wave induced fluctuations.

One of the important quantity which one can inferred from the VHF radar is the Doppler velocities of the small scale size irregularities. It is debatable whether these velocities correspond to phase velocities of the drift waves or the the guiding center drifts induced by CRT instability. The velocity expressions derived by [64, 67] for CRT instability explain the large velocities, 200-300 m/s, observed by *in situ* measurements. The drift wave velocities associated with the observed steep gradients [14] is on the other hand restricted to the 20-100 m/s range. Recent simultaneous observation of 3m and 8m irregularities over Indian zone [87] reveal the dispersive nature of Doppler velocities and found that the ratio of velocities at these scale sizes is nearly equal to the reciprocal of corresponding wavelength ratio which is what one would expect from the drift waves.

1.2.6 Variabilities in ESF

So far so we discussed the generation of macro-micro instabilities responsible for ESF phenomenon. ESF phenomenon is highly variable in nature as it exhibits the day-to-day variabilities in the occurrence as well as in the morphology as revealed by radar observations. Some night one observe the spread F while very next night one doesn't. Some night spectacular spread F is seen while the very next night one sees the bottomside spread F. The satellite and *in situ* measurements moreover reveal that the ion compositions in the ionosphere is highly variable during ESF [60, 63, 97]. It has been experienced that such variabilities and unpredictability are the consequence of variabilities occur in the background ionosphere. The numerical simulation of GRT instability [65, 113, 112, 35, 36, 83, 88] deal with the effects of the background conditions on the evolution of spread F. The nature of seeding perturbation for GRT instability has also been a subject of great interest after the observations [78, 79, 80] of large scale wave-like structures of ESF. The VHF observation [48, 45] reveal the bottomside undulation over which plumes ride. Kelley et al [48] argued that the GRT instability mechanism is the most important mechanism for production of plumes but that gravity waves are an extremely efficient source to seed perturbations for excitation of large-scale GRT instability. The spatial resonance proposed by Whitehead [106] and Klostermeyer [54] which may oc-

cur during postreversal or prereversal [45] is not the necessary condition for the efficient seeding and so for the excitation of GRT instability. The numerical simulation by Huang et al [33, 34, 35, 36] confirm it and unfold many interesting aspects regarding gravity wave as a seeding perturbation for CRT instability. Their investigation with two seeding gravity waves reveal that the large-scale gravity wave determines the outer scale of ESF irregularities and the small-scale perturbation results in multiple plumes preferentially located on the west wall. It is also found by them that the timing of the seed gravity wave is crucial for ESF generation. If a gravity wave exists in the F region during the prereversal of electric field, the gravity wave can initiate the GRT instability and result in topside bubble. In contrast, gravity-wave-induced perturbations in a descending ionosphere evolve with large scale bottomside wave-like structures but not bubbles. They also argue that the only gravity waves propagating in small angle to the zonal direction are expected to be capable of generating ESF bubbles. These factors are all in variable from day-to-day and their variation must cause variation of resulting ESF.

1.3 Objective and outline of the thesis

As it is discussed in last section that the ESF exhibits variabilities owing to the varying background conditions. It is therefore essential to study the ESF phenomena under different background conditions. The objective of this research work is to investigate the effects of background conditions on the plasma instabilities in order to understand the variabilities in ESF phenomena.

One of the varying background condition is the relative ion compositions in the F region. The satellite observation [60] shows the presence of NO^+ ions inside the depletion on the topside [fig. 1(a)]. However its not always the case [60, 63] also. The early ion composition observation [26, 27] reveal the significant Fe^+ ions on the topside too. If no other mechanism is involved then its the GRT instability induced transport which should bring NO^- ions and Fe^+ ions on to the topside provided they are available on the bottomside. The *in situ* ion composition measurements [63, 95, 10] indeed reveal the presence of considerable NO^+ ions on the bottomside which was earlier thought to be mainly consist of O^+ ions [fig. 1(b,c,d)]. The theoretical investigation [3] reveal that prereversal enhancement causes the existence of considerable NO^+ ions on the bottomside. Since prereversal itself is highly variable in nature the ion composition in bottomside also varies. In view of these measurements, it is therefore essential to study the role of molecular ions in the growth of GRT instability and its further evolution. So far the GRT instability is investigated in the presence of O^+ ions. In present work linear theory is developed by considering both O^- and NO^+ dynamics. The theory is further extended for Fe^+ ions as well. The nonlinear evolution of GRT instability in the presence of both O^+ and NO^+ ions is discussed thereafter.

The observations of small scale size irregularities by VHF radar also reveal interesting aspects of large scale GRT instability. The observation of 3m scale size irregularities by Indian MST radar is presented. Few interesting aspects regarding morphology and bubble velocities which stem out from our observations are discussed on the basis of existing theories.

Interaction of two simultaneous seeding perturbations under nonlinear GRT instability is studied further to understand the features emerged from our observations.

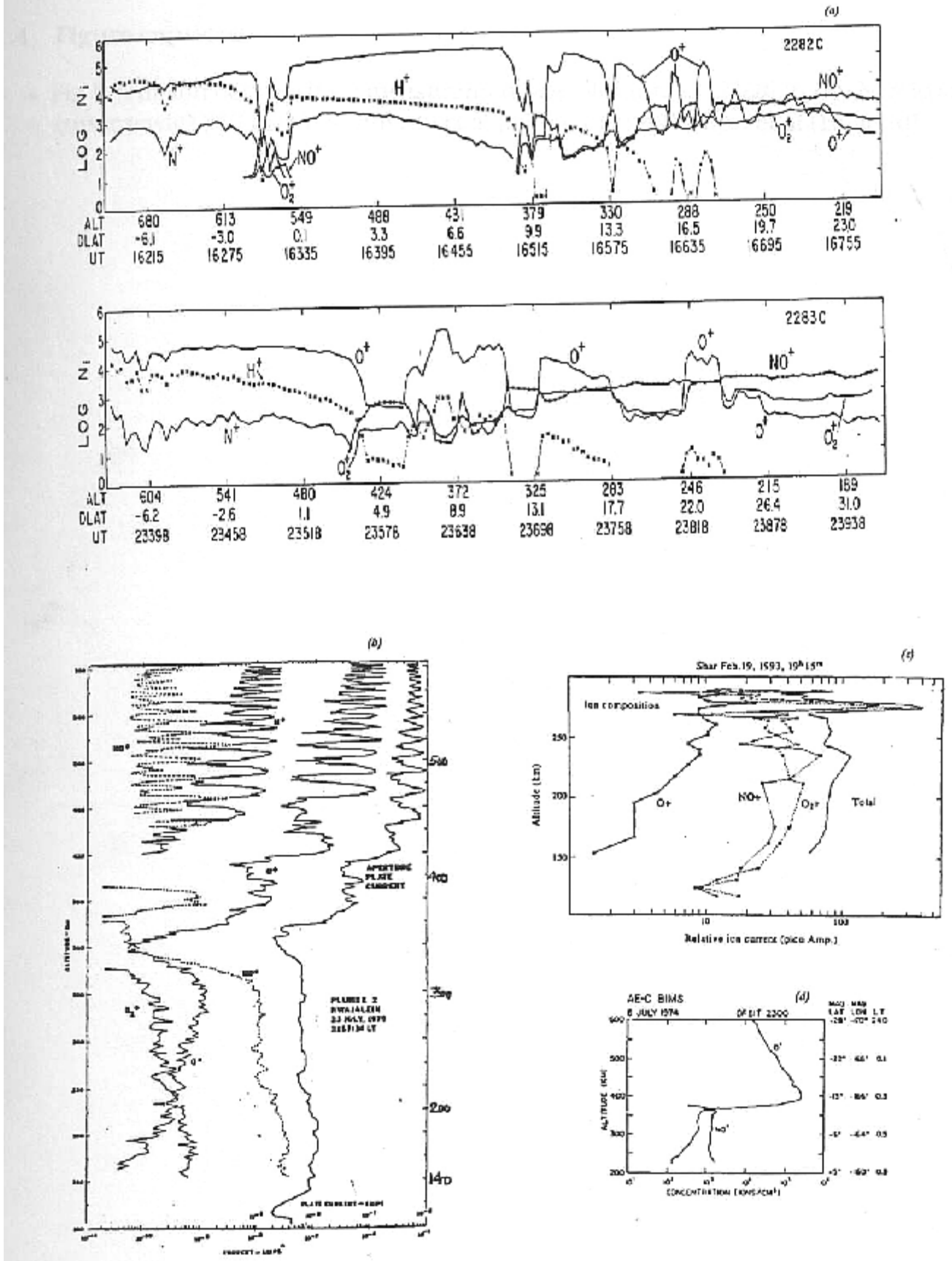

Figure 1.

1.4 Figure captions

- Fig 1. :The ion composition measurements by McClure et al [60] in (a), Narcisi and szuszczewicz [63] in (b), Sridharan et al [95] in (c) and Brinton et al [10] in (d).

Chapter 2

Effects of molecular ions on the GRT instability: Linear analysis

2.1 Introduction

As discussed in Introduction, plasma instability processes play a crucial role in the development of irregularities in electron and ion densities in the nighttime of equatorial ionosphere. The GRT instability driven by gravity, electric field and wind is believed to be causative mechanism for initiation of large scale plasma irregularities. The linear analysis [25, 29, 82] of GRT instability deals with the dynamics of O^+ ion alone by assuming the F-region plasma as single ion-electron plasma. However the ion composition measurements of undisturbed ionosphere [10] and during spread F [63, 95] reveal that the molecular ions (NO^+, O^+) are dominant up to the base of the F region and above the base O^+ ions become dominant. Thus the region near the base acts as two ions-electron plasma. Since entire bottomside is susceptible to become unstable under GRT instability, the investigation of the instability by considering the F region as two ions-electrons plasma becomes important.
In the present chapter, the linear growth rate of the GRT instability for two ions-electron plasma is derived by solving the set of fluid equations under the first order perturbation analysis. Before describing the analysis, it is worth to discuss the changes expected to occur in steady state ionospheric quantities such as current density and plasma scale height which act as the sources of free energy for the instability.

2.2 The steady state current density and electron scale height for two ions-electron plasma

2.2.1 The zonal current density

The differential velocities among the dominant species give rise the steady state current in the ionosphere,

$$\vec{J} = \sum n_a . q_a . \vec{V}_a$$

where n_a, q_a *and* $\vec{V}_a$ are the number density, charge and velocity of the charged particle. The forces (gravity, electric fields, drag forces due to winds) acting on the ionosphere are responsible for the differential velocities of the species. Under the action of these forces separately, the charge particle with mass m_a and charge q_a moves with velocities:

$$\vec{V}_a = \left(\frac{m_a}{q_a}\right)\frac{\vec{g}\times\vec{B}}{B^2}, \quad \vec{V}_a = \left(\frac{q_a}{m_a}\right)\left(\frac{\nu_{an}}{\Omega_a^2}\right)\vec{E}, \quad \vec{V}_i = \left(\frac{\nu_{an}}{\Omega_a}\right)\frac{\vec{W}\times\vec{B}}{B} \tag{2.1}$$

These velocities are the Hall drift due to gravity $\vec{g}$, Pedersen drift due to electric field $\vec{E}$ and Hall drift due to drag force, $\nu_{an}\vec{W}$ respectively. Since they are proportional to the ratio (m_a/q_a), finite current flows due to the differential motions of particles of different masses and charges. Such current is mainly carried by ions owing to their large masses. Obviously the large current would flow in two ions-electron plasma as compared to one ion-electron plasma owing to the contribution from another ion, NO^+. Its expression in two ions-electron plasma can be written as:

$$\vec{J} = n_1\vec{V}_1 + n_2\vec{V}_2 - n_e\vec{V}_e$$

where subscripts 1,2 and e stands for O^-, NO^+ and electrons respectively.
If $+\hat{x}$ axis represents westward direction and for simplicity if only gravity driven velocities are considered then it becomes:

$$\vec{J} = -(n_1m_1 + n_2m_2)\frac{g}{B}(\hat{x})$$

The negative sign indicates that the current is in eastward direction. However, the earlier investigation of CRT instability for one ion-electron plasma [25, 64, 50] reveal that its the divergence of $\vec{J}$, rather than $\vec{J}$ itself which is important for the generation of the instability , since it generates the polarization electric field. In the presence of density inhomogeneity along the current direction, the expression for divergence, δJ, of $\vec{J}$ in two ions-electron plasma becomes:

$$\delta J = -(m_1\delta n_1 + m_2\delta n_2)\frac{g}{B} \tag{2.2}$$

where δn_a is the gradient in number density of ion 'a'. For one ion-electron plasma, the corresponding expression is:

$$\delta J_o = -m_1\delta n_c\frac{g}{B}$$

The ratio of these two divergence then becomes:

$$\frac{\delta J}{\delta J_o} = \frac{(m_1\delta n_1 + m_2\delta n_2)}{m_1(\delta n_1 + \delta n_2)} \tag{2.3}$$

Depending on the relative sign of δn_1 and δn_2, the current density divergence in two ions-electron plasma may become larger or smaller than its value for one ion-electron plasma. The nature of δn_1 and δn_2 can be known only by the first order perturbation analysis which is treated in the next section.

2.2.2 The plasma scale heights in two ions-electron plasma

In general, the scale heights of ions and electrons are defined as:

$$L_a = \left[\frac{1}{n_a}\frac{dn_a}{dy}\right]^{-1} \tag{2.4}$$

It is known [25, 13, 82] that the growth rate for one ion-electron plasma is inversely proportional to the O^+ scale height L_1. Owing to charge neutrality condition, it takes the

value equals to electron scale height, L_e. For two ions-electron plasma, the electron scale height can be defined as:

$$\frac{1}{L_e} = \frac{1}{(n_1 + n_2)}\left[\frac{n_1}{L_1} + \frac{n_2}{L_2}\right] \tag{2.5}$$

where L_2 is the NO^+ scale height. Thus the L_1 takes the value:

$$L_1 = \left\{\frac{n_1}{(n_1 + n_2) - n_2(L_e/L_2)}\right\} L_e \tag{2.6}$$

which is less than L_e since L_2 is negative [10, 3, 63]. Thus for given L_e and L_2, the value of L_1, which directly enters into the growth rate of one ion-electron plasma, adjusts itself according to the charge neutrality condition and becomes less than L_e. One expect the growth rate for present case to be inversely proportional to L_e as we have derived in section 2.3.2 later. Hence effect of scale height is to reduce the growth rate in present case as compared to one ion-electron plasma.
In this section we have discussed the changes occur in sources of free energy for GRT instability when F region is considered as composed of two ions (O^+ and NO^+) rather than just of single ion O^+. It is however emphasized that the first order perturbation analysis is required to understand the complete nature of such changes and their impact on the growth rate of GRT instability. These aspects are now discussed subsequently.

2.3 First order perturbation analysis of GRT instability in two ions-electron plasma

The night-time equatorial ionosphere is considered in a slab geometry which means that the curvature of the Earth's magnetic field is ignored. The positive unit vectors $\hat{x}$, $\hat{y}$ *and* $\hat{z}$ of the Cartesian co-ordinate system are directed along westward, upward and northward respectively. The following plasma fluid equations, that govern the motions of the two positive ions (dominant ion is denoted by suffix 1 while the second ion is denoted by suffix 2) and electrons (denoted by suffix e) whose masses are represented as m_1, m_2 and m_e respectively, are considered:

$$\left(\frac{\partial \vec{v}_1}{\partial t}\right) = \left(\frac{e}{m_1}\right).\left(\vec{E} + \vec{v}_1 \times \vec{B}\right) - \nu_{in}.\left(\vec{v}_1 - \vec{W}\right) + \vec{g} \tag{2.7}$$

$$\left(\frac{\partial \vec{v}_2}{\partial t}\right) = \left(\frac{e}{m_2}\right).\left(\vec{E} + \vec{v}_2 \times \vec{B}\right) - \nu_{in}.\left(\vec{v}_2 - \vec{W}\right) + \vec{g} \tag{2.8}$$

$$\left(\frac{\partial \vec{v}_e}{\partial t}\right) = \left(\frac{-e}{m_e}\right).\left(\vec{E} + \vec{v}_e \times \vec{B}\right) - \nu_{en}.\left(\vec{v}_e - \vec{W}\right) + \vec{g} \tag{2.9}$$

$$\frac{\partial n_1}{\partial t} = p_1 - l_1 - \nabla.(n_1.\vec{v}_1) \tag{2.10}$$

$$\frac{\partial n_2}{\partial t} = p_2 - l_2 - \nabla.(n_2.\vec{v}_2) \tag{2.11}$$

$$\frac{\partial n_e}{\partial t} = p_e - l_e - \nabla.(n_e.\vec{v}_e) \tag{2.12}$$

$$\vec{E} = -\nabla\phi \tag{2.13}$$

$$\nabla.\vec{J} = 0 \tag{2.14}$$

where,

$$\vec{J} = e.(n_1.\vec{v}_1 + n_2.\vec{v}_2 - n_e.\vec{v}_e) \tag{2.15}$$

The symbols n_1, n_2 and n_e represent number densities of dominant atomic oxygen ions, molecular ions and electrons respectively, while their velocities, in the same order, are represented by $\vec{v}_1$, $\vec{v}_2$ and $\vec{v}_e$. Here e corresponds to the magnitude of the charge. The ion-neutral collision frequency, ν_{in}, is taken to be same for both the ions.
Equation (2.13) describes the electrostatic nature of the problem while equation (2.14) describes the current conservation where the total current density ($\vec{J}$) is given by equation (2.15).
The steady state drift velocities of the ions are obtained by solving the equations (2.7) and (2.8).

$$\vec{v}_1 = \frac{\vec{E}\times\vec{B}}{B^2} + \frac{\nu_{in}}{\Omega_1^2}.\frac{e}{m_1}\vec{E} + \frac{m_1}{e}.\frac{\vec{g}\times\vec{B}}{B^2} + \frac{\nu_{in}}{\Omega_1}.\frac{\vec{W}\times\vec{B}}{B} + \frac{\nu_{in}}{\Omega_1^2}.\vec{g} + \frac{\nu_{in}^2}{\Omega_1^2}.\vec{W} \tag{2.16}$$

$$\vec{v}_2 = \frac{\vec{E}\times\vec{B}}{B^2} + \frac{\nu_{in}}{\Omega_2^2}.\frac{e}{m_2}\vec{E} + \frac{m_2}{e}.\frac{\vec{g}\times\vec{B}}{B^2} + \frac{\nu_{in}}{\Omega_2}.\frac{\vec{W}\times\vec{B}}{B} + \frac{\nu_{in}}{\Omega_2^2}.\vec{g} + \frac{\nu_{in}^2}{\Omega_2^2}.\vec{W} \tag{2.17}$$

The first term corresponds to the dominant Hall drift which is the same for both the species as the Hall drift is independent of charge and mass. The second term is the Pedersen drift associated with the electric field due to the finite collisions and depends on mass of the species. The third and fourth terms are the drifts due to the applied forces (gravity and wind respectively in this case) in the Hall direction which also depend on the mass of the species. The fifth and the last terms correspond to the drifts due to the applied forces in the Pedersen direction and since their magnitudes in the F region ionosphere are relatively small these terms are neglected for further calculation.
Similarly, the steady state velocity of electrons in the F region of the ionosphere is obtained by solving (2.9) as

$$\vec{v}_e = \frac{\vec{E}\times\vec{B}}{B^2} \tag{2.18}$$

the contribution from the other terms are negligible as $\Omega_e >> \nu_{en}$.
First order perturbation analysis is carried out by assuming the perturbations in the variables $(\delta\vec{v}_1, \delta\vec{v}_2, \delta\vec{v}_e, \delta\phi, \delta n_1, \delta n_2, \delta n_e)$ over the corresponding steady state values $(\vec{v}_1, \vec{v}_2, \vec{v}_e, \phi, n_1, n_2, n_e)$. The perturbations are assumed to be in the zonal direction in the form of $exp(ikx - i\omega t)$, where ω and k are the angular frequency and zonal wavenumber of the perturbation respectively. The steady state parameters are assumed to have significant altitude variations only. The following expressions for perturbed velocities are obtained by substituting the respected perturbed quantities and after subtracting the steady state velocities :

$$\delta\vec{v}_1 = \frac{e}{m_1}.\frac{[i(kv_{1x}-\omega)+\nu_{in}]}{\Omega_1^2 + [i(kv_{1x}-\omega)+\nu_{in}]^2}.(-ik\delta\phi)\hat{x} - \frac{e}{m_1}.\frac{\Omega_1}{\Omega_1^2 + [i(kv_{1x}-\omega)+\nu_{in}]^2}.(-ik\delta\phi)\hat{y} \tag{2.19}$$

$$\delta\vec{v}_2 = \frac{e}{m_2}.\frac{[i(kv_{2x}-\omega)+\nu_{in}]}{\Omega_2^2+[i(kv_{2x}-\omega)+\nu_{in}]^2}.(-ik\delta\phi)\hat{x} - \frac{e}{m_2}.\frac{\Omega_2}{\Omega_2^2+[i(kv_{2x}-\omega)+\nu_{in}]^2}.(-ik\delta\phi)\hat{y} \tag{2.20}$$

$$\delta\vec{v}_e = \frac{e}{m_e}.\frac{\Omega_e}{(\Omega_e^2-\omega^2)}.(-ik\delta\phi)\hat{y} \tag{2.21}$$

Here the perturbation electric field $\vec{\delta E}$ is assumed to be electrostatic and hence can be obtained by scalar potential $\delta\phi$ using the relation $\delta\vec{E} = -\nabla\delta\phi$.
Similarly, perturbation analysis is carried out with continuity equations and the following relations are obtained:

$$(ikv_{1x}-i\omega).\delta n_1 + i.kn_1\delta v_{1x} + \frac{n_1}{L_1}.\delta v_{1y} = 0. \tag{2.22}$$

$$(ikv_{2x}-i\omega).\delta n_2 + ikn_2\delta v_{2x} + \frac{n_2}{L_2}.\delta v_{2y} = 0. \tag{2.23}$$

$$(ikv_{ex}-i\omega).\delta n_e + ikn_e.\delta v_{ex} + \frac{n_e}{L_e}.\delta v_{ey} = 0. \tag{2.24}$$

Perturbation analysis with the current conservation equation yields,

$$ik(n_1\delta v_{1x}+n_2\delta v_{2x}-n_e\delta v_{ex}) + (\frac{n_1}{L_1}.\delta v_{1y}+\frac{n_2}{L_2}.\delta v_{2y}-\frac{n_e}{L_e}.\delta v_{ey}) + ik(\delta n_1 v_{1x}+\delta n_2 v_{2x}-\delta n_e v_{ex}) = 0 \tag{2.25}$$

where L_1, L_2 and L_e are the plasma scale lengths of atomic oxygen ions, molecular ions and electrons respectively defined by eq. (2.4).

Substitution of $\delta\vec{v}_1$, δv_2 and $\delta\vec{v}_e$ in the above four perturbed equations yields a set of four linear equations involving the variables $\delta n_1, \delta n_2, \delta n_e$ and $\delta\phi$. The necessary and sufficient condition to obtain a non-trivial solution for these variables is to set the determinant of the co-efficient matrix to be zero,

$$\begin{vmatrix} kv_{1x}-\omega & 0 & 0 & \frac{n_1}{L_1}-ikn_1\frac{\nu_{in}}{\Omega_1} \\ 0 & kv_{2x}-\omega & 0 & \frac{n_2}{L_2}-ikn_2\frac{\nu_{in}}{\Omega_2} \\ 0 & 0 & kv_{ex}-\omega & \frac{n_e}{L_e} \\ kv_{1x} & kv_{2x} & -kv_{ex} & \frac{n_1}{L_1}-ikn_1\frac{\nu_{in}}{\Omega_1}+\frac{n_2}{L_2}-ikn_2\frac{\nu_{in}}{\Omega_2}-\frac{n_e}{L_e} \end{vmatrix} = 0 \tag{2.26}$$

$$\begin{vmatrix} kv_{1x}-\omega & 0 & 0 & \frac{n_1}{L_1}-ikn_1\frac{\nu_{in}}{\Omega_1} \\ 0 & kv_{2x}-\omega & 0 & \frac{n_2}{L_2}-ikn_2\frac{\nu_{in}}{\Omega_2} \\ 0 & 0 & kv_{ex}-\omega & \frac{n_e}{L_e} \\ \omega & \omega & -kv_{ex} & -\frac{n_e}{L_e} \end{vmatrix} = 0 \tag{2.27}$$

We drop out suffix 'x' in velocities for further investigation and let

$$a_i = \frac{\nu_i}{L_i}, b_i = km_i\frac{\nu_{in}}{\Omega_i}$$

then the above equation becomes

$$(kv_1 - w)[(kv_2 - w)(wA_e - kv_eA_e) + (A_2 - iB_2)w^2] - (a_1 - ib_1)[-(k_2v_2 - w)w^2]$$

$= 0$ since $kv_e << w$,

$$(kv_1 - w)(kv_2 - w)A_e + (kv_1 - w)(a_2 - ib_2)w + (kv_2 - w)(a_1 - ib_1)w = 0$$

or,

$$(kv_1kv_2 - wkv_1 - wkv_2w^2)A_e + kv_1a_2w - ikv_1b_2w - a_2w^2 + ib_2w^2 = 0$$

We decompose the frequency w to real part w and imaginary part γ such that $\gamma << \omega$, i.e,

$$\omega = \omega + i\gamma \ and \ \omega^2 = \omega^2 + 2i\omega\gamma$$

After substituting it, and setting real part and imaginary part of the above equation separately equals to zero, we get coupled algebraic equations

$$kv_1kv_2A_e - w(kv_1 + kv_2)A_e + kv_1a_2w + kv_1b_2\gamma - 2b_2w\gamma + kv_2a_1w + kv_2b_1\gamma - 2b_1w\gamma = 0 \quad (2.28)$$

$$-\gamma k(v_1 + v_2)a_e + 2a_ew\gamma + kv_1a_2\gamma - kv_1b_2w - 2a_2w\gamma + b_2w^2 + kv_2a_1\gamma - kv_2b_1w - 2a_1w\gamma + b_1w^2 = 0 \quad (2.29)$$

With the use of equality

$$a_e = a_1 + a_2$$

the equation (2.29) becomes

$$-\gamma k(v_1a_1 + kv_2a_2) - kv_1b_2w + b_2w^2 - kv_2b_1w + b_1w^2 = 0$$

The local approximation

$$kL_1 >> 1 \quad or \quad \frac{\gamma a_1}{wb_1} << 1$$

further reduces it to,

$$(b_1 + b_2)w - k(v_1b_2 + v_2b_1) = 0$$

which gives the expression for the phase velocity of the perturbation as,

$$\frac{w}{k} = \frac{(v_1b_2 + v_2b_1)}{(b_1 + b_2)} \quad (2.30)$$

It can also be written as

$$\frac{w}{k} = \frac{(v_1b_1 + v_2b_2)}{(b_1 + b_2)} + \frac{(v_1 - v_2)(b_2 - b_1)}{(b_1 + b_2)}$$

the last term is $\sim O[(m_1 - m_2)^2]$ and can be neglected compared to first term. Thus the expression for phase velocity becomes,

$$\boxed{\frac{w}{k} = \frac{(v_1 b_1 + v_2 b_2)}{(b_1 + b_2)}} \tag{2.31}$$

By knowing the expression for phase velocity, the growth rate expression can be derived from Eq. (2.28). In equation (2.28) the second term is $\sim O[k(v_1^2 + v_2^2 + 2v_1 v_2)A_e]$ and so the first term can be neglected compared to it. With the use of expression of phase velocity given by Eq. (2.31), it becomes

$$-w(kv_1 + kv_2)a_e + w(kv_1 a_2 + kv_2 a_1) + w(b_1 + b_2)\gamma - 2w(b_1 + b_2)\gamma = 0$$

which can be derived for growth rate, γ, as:

$$\gamma = \frac{1}{(b_1 + b_2)}[-k(v_1 + v_2)a_e + k(v_1 a_2 + v_2 a_1)] \tag{2.32}$$

The substitution of $a_e = a_1 + a_2$ brings it to the form:

$$\gamma = -\frac{k}{(b_1 + b_2)}[v_1 a_1 + v_2 a_2]$$

where

$$v_1 = \frac{\nu_{in}}{\Omega_1}.\frac{E_{x0}}{B} - \frac{g}{\Omega_1} + \frac{\nu_{in}}{\Omega_1}.W_y \text{ and } v_2 = \frac{\nu_{in}}{\Omega_2}.\frac{E_{x0}}{B} - \frac{g}{\Omega_2} + \frac{\nu_{in}}{\Omega_2}.W_y \tag{2.33}$$

are the x-components of the velocities given by eqs. (2.16) and (2.17) respectively. E_{x0} and W_y are ambient westward electric field and upward wind respectively. In equation (2.33), the dominant differential velocities which contributes for the growth of the plasma instabilities are included. However for simplicity the henceforth discussion considers the velocities driven by gravity only. The expression for growth rate then takes the form:

$$\boxed{\gamma = \frac{g}{\nu_{in}(n_1 m_1 + n_2 m_2)}\left[n_1 \frac{m_1}{L_1} + n_2 \frac{m_2}{L_2}\right]} \tag{2.34}$$

Another interesting form of γ which retains all three scale heights, can be derived from equation (2.32). By multiplying and dividing it by $(b_1 + b_2)$ and rearranging the terms, we

get an expression for growth rate as:

$$\gamma = \frac{1}{(n_1\frac{\nu_{in}}{\Omega_1} + n_2\frac{\nu_{in}}{\Omega_2})^2}\left[-v_1\frac{n_e}{L_e}n_1\frac{\nu_{in}}{\Omega_1} - v_2\frac{n_e}{L_e}n_2\frac{\nu_{in}}{\Omega_2} + (v_2 - v_1)(\frac{n_1}{L_1}n_2\frac{\nu_{in}}{\Omega_2} - \frac{n_2}{L_2}n_1\frac{\nu_{in}}{\Omega_1})\right] \quad (2.35)$$

Many interesting aspects of γ with this form are discussed by us [89]. However Owing to its simple form, the expression (2.34) for growth rate is here considered for further discussion. In this expression the two terms in square bracket correspond to O^+ and NO^+ ions respectively. Both the terms are proportional to their corresponding number densities and inverse of scale heights. The number density dependence is quite distinct feature from the growth rate of one ion-electron plasma which is independent of number density. The scale height dependence however is similar but now it comes along with some weighting factors. The ion composition measurements and theoretical investigation reveal [63, 3] reveal that both number densities and scale heights considerably vary within the F region. Below the base, NO^+ ions dominate with very large positive scale height, i.e. $n_2 > n_1$, $L_2 > L_1$ whereas above the base, L_2 becomes negative and O^+ ions dominate, i.e. $n_2 < n_1$, $L_2 < 0$. However near the base, either situation $n_2 \sim n_1$ or $n_2 < n_1$ may exist depending on whether cross over from NO^+ ions to O^+ ions take place at or below the base. In either of the situation, the L_2 is negative near the base. Thus at and above the base, the second term in γ is negative. In order to have positive growth of perturbation, the ratio of the two terms then

$$r = \frac{n_2 m_2/L_2}{n_1 m_1/L_1}$$

must be less than unity, i.e.,

$$\frac{L_1}{L_2} < (\frac{n_1}{n_2})(\frac{m_1}{m_2})$$

This condition is easily satisfied by ionosphere above the base where $n_1 > n_2$. The interesting point to note that the condition is adjustable to its own so far as $n_1 > n_2$. If L_2 is small causing the large value of left hand side of inequality then since n_2 will also becomes small causing right hand side to increase. If cross over doesn't takes place at the base then near the base $n_1 > n_2$ and so inequality is easily satisfied at the base. However if the cross over takes place just near the base then $n_1 \sim n_2$ there, the condition becomes

$$\frac{L_1}{L_2} < (\frac{m_1}{m_2})$$

which looks to be severe. It requires the O^+ density profile to be steeper, at least twice, than NO^+ density profile which is what usually observed [63]. Thus in normal circumstances, growth rate is positive throughout the bottomside. Nonthless the growth rate would be smaller at the base as compared at any altitude above the base. In fig. 1(a,b), the growth rate given by expression (2.34) and growth rate for one ion-electron plasma, $\gamma_o = \frac{g}{\nu_{in}L_1}$, are plotted respectively. Since both density ratio, n_2/n_1, and ν_{in} varies with altitude, both the variations are simultaneously taken into account. At 340 km altitude, both the ion densities, n_1 and n_2, are 10^3 cm^{-3} and with altitude they vary exponentially with their corresponding scale heights which are 7.5 km and -30 km respectively. The

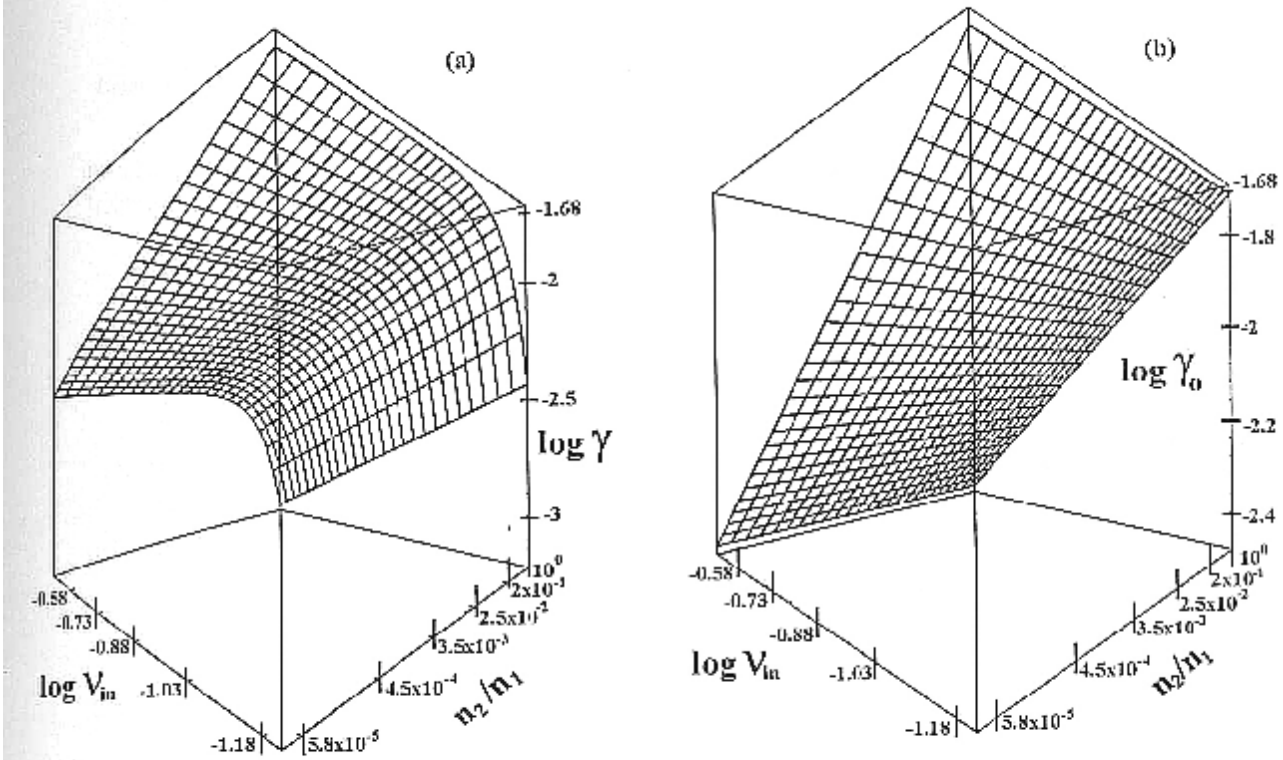

Figure 1.

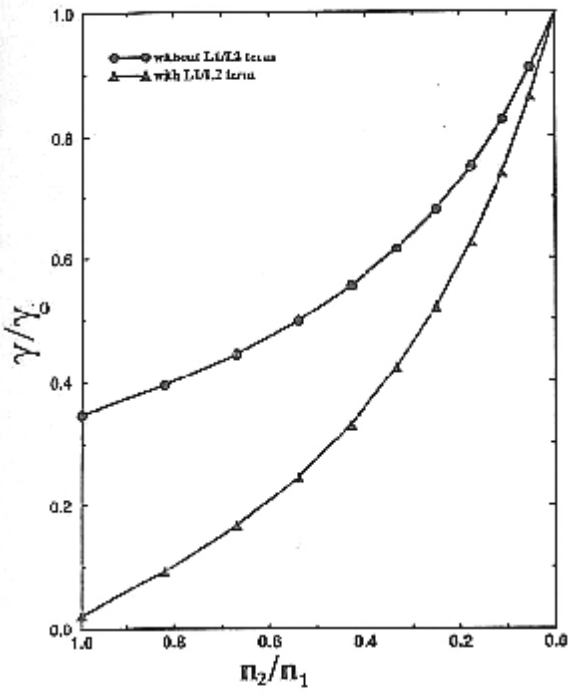

Figure 2.

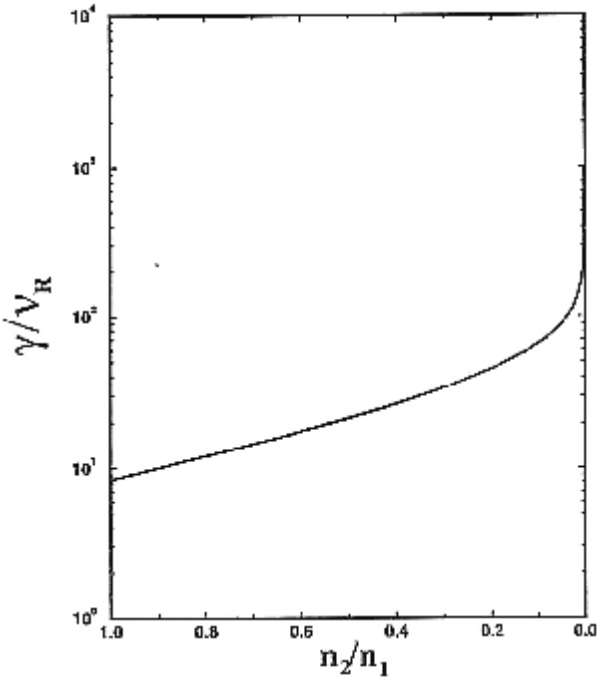

Figure 3.

suitable altitude profile of ν_{in} is chosen. The altitude varies from 340 km to 405 km. Following points are evident from the plots:

- The growth rate, γ_o, doesn't show any dependence on density ratio, as expected. However, the growth rate, γ does show dependence on it and its effect is even more pronounced than the effect of ν_{in} for its value closer to unity. Within the change in density ratio by almost one order from unity to, γ is changed by 80%, while within the change in ν_{in} by almost two order, the γ is changed by same amount.
- The growth rate, γ, is positive but smaller than the growth rate , γ_o, for given ν_{in}. The reduction is considerable, however, for values of density ratio closer to unity. Within the reduction in density ratio by one order from unity, the growth rate is increased considerably and attains the value almost equal to γ_o. For further reduction in density ratio, it remains constant.

2.3.1 The comparison of growth rates of CRT instability for two ions-electron and one ion-electron plasma

In contrast to the growth rate of CRT instability for one ion-electron plasma

$$\gamma_o = \frac{g}{\nu_{in} L_1}$$

the growth rate for two ions-electron plasma

$$\gamma = \frac{g}{\nu_{in}(n_1 m_1 + n_2 m_2)}[n_1 \frac{m_1}{L_1} + n_2 \frac{m_2}{L_2}]$$

explicitly depends on number densities and masses of both the ions. The ratio of the growth rates is:

$$\frac{\gamma}{\gamma_o} = \frac{1}{(n_1 m_1 + n_2 m_2)}[n_1 m_1 + n_2 m_2 (\frac{L_1}{L_2})]$$

$$\frac{\gamma}{\gamma_o} = 1 - \frac{n_2 m_2}{n_1 m_1 + n_2 m_2}(1 - \frac{L_1}{L_2}) \tag{2.36}$$

The last term in left hand side is always positive since L_2 is negative at and above the base. Thus
the growth rate for two ions-electron plasma is less than the growth rate for one ion-electrons plasma.
If we neglect L_1/L_2 compared to unity for a moment then

$$\frac{\gamma}{\gamma_o} = 1 - \frac{n_2 m_2}{n_1 m_1 + n_2 m_2}$$

which can also be written as

$$\frac{\gamma}{\gamma_o} = 1 - \frac{1}{(\frac{n_1 m_1}{n_2 m_2} + 1)}$$

The last term in right side is maximum for ratio n_1/n_2 equals to unity. Thus the maximum reduction in growth occurred for ratio n_1/n_2 equals to unity. In fig.2, this ratio is plotted for decreasing values of ratio n_2/n_1. The features driven by this plot are same as driven by plots shown in fig. 1. In reality however the scale height ratio never vanishes. At the same time its easier to uniquely evaluate the L_c from the observation or theoretical

calculation rather than L_1. The NO^+ ions specifically follow the neutral profile N_2 above the base [3], and so it can be uniquely define. In terms of scale height ratio $\frac{L_e}{L_2}$, rather than $\frac{L_1}{L_2}$, the ratio of growth rates, (2.36), can be written as:

$$\frac{\gamma}{\gamma_o} = 1 - \frac{n_2 m_2}{n_1 m_1 + n_2 m_2}\left\{1 - \frac{L_e/L_2}{[(1 + n_2/n_1) - (n_2/n_1)(L_e/L_2)]}\right\} \tag{2.37}$$

In fig. 2, this ratio is plotted by taking the L_e and L_2 values as 20 and -30 km which are deduced from the observation and theoretical calculation [63, 3]. Note that the assumption of zero scale height ratio $\frac{L_1}{L_2}$ implies $\frac{L_e}{L_2}$ also to be zero. By comparing the two plots in fig. 2, it follows that the growth rate is considerably reduced for finite negative value of L_e/L_2 as compared to its value equals to zero. In fact by assuming the scale height ratio equals to zero we assume either the electron has very large positive density gradient or NO^+ has very small negative gradient. Both the situations are conducive for enhanced growth rate. The fig. 1 in last section indicates the highly sensitive nature of growth rate, γ to the density ratio. The fig. 2 further reveal that the growth rate is highly sensitive to the scale height ratio also. By taking the small scale height ratio, $\frac{L_e}{L_2}$, the γ can be made large, though never greater than γ_o. The plot shown in fig. 2 is different from corresponding plot presented in paper [89] which was plotted with deduced values of all the scale heights from observation [63] and using growth rate expression (2.35). The L_1 value was 15 km while L_e and L_2 were taken to be same as in present case. Obviously these values don't satisfy the condition (2.5) which is otherwise used to obtain L_1, for given L_e and L_2, in present case. We feel that there is uncertainty in calculating the L_1 from density profile given by [63] since it was taken during spread F condition.

2.3.2 The cause for the reduction of the growth rate

In last section we found that the growth rate is considerably reduced with the introduction of second dominant ion NO^+. The cause for reduction can be inferred from the perturbed equations (2.22 - 2.25). The substitution of ω as $\omega + i\gamma$ in perturbed continuity equations leads to there real parts as:

$$\gamma \delta n_1 + \frac{n_1}{L_1}\delta v_{1y} = 0$$
$$\gamma \delta n_2 + \frac{n_2}{L_2}\delta v_{2y} = 0$$
$$\gamma \delta n_e + \frac{n_e}{L_e}\delta v_{ey} = 0$$

Here $\delta v_{(1,2,e)y}$ are the perturbed vertical velocities given by y-components of velocity expressions (2.19 - 2.21). With valid F region approximation ($\Omega_{(1,2)} >> \nu_{in} >> \omega$), vertical velocities of both the ions and electron become same in magnitude

$$\delta v_{1y} = \delta v_{2y} = \delta v_{ey} = -(1/B)(-ik\delta\phi) = -(1/B)\delta E = -v_{pol} \ \ (say)$$

and electron continuity equation becomes:

$$\gamma\, \delta n_e = -\frac{n_e}{L_e}\frac{\delta E}{B} \tag{2.38}$$

Using x-component of unperturbed and perturbed velocities given by (2.16-2.21) , the expression for δE can be obtained from the perturbed current conservation equation (2.25) as:

$$\delta E = \frac{(m_1\delta n_1 + m_2\delta n_2)(g/B)}{\sigma} \tag{2.39}$$

where σ is Pedersen conductivity given by:

$$\sigma = \sum_a \frac{\nu_{in}}{\Omega_a^2}\frac{n_a q_a}{m_a} \tag{2.40}$$

In expression of δE, the numerator on the right hand side is nothing but the divergence of current density derived in section (2.2.1). The electron continuity equation further gives the relation among perturbed quantities and growth rate:

$$\boxed{\gamma\delta n_e = \frac{n_e}{L_e}\frac{\delta J}{\sigma\ B}} \tag{2.41}$$

It is obvious that for given amplitude of perturbation δn_e, the growth rate is:
(1) proportional to divergence of current density $\delta\vec{J}$,
(2) inversely proportional to conductivity σ,
(3) inversely proportional to electron scale height L_e.

The same relationship holds in one ion-electron plasma also. However, these quantities are significantly different in magnitudes in two cases.

The reduction in divergence of current density

In section (2.2.1), the ratio of divergence of current density for two ions-electron plasma to one ion-electron plasma was derived as:

$$\frac{\delta J}{\delta J_o} = \frac{(m_1\delta n_1 + m_2\delta n_2)}{m_1(\delta n_1 + \delta n_2)}$$

which can also be written as:

$$\frac{\delta J}{\delta J_o} = \frac{(1 + \frac{m_2}{m_1}\frac{\delta n_2}{\delta n_1})}{(1 + \frac{\delta n_2}{\delta n_1})} \tag{2.42}$$

The expression for δn_1 and δn_2 can be obtained from the perturbed continuity equations as :

$$\delta n_1 = \frac{n_1}{L_1}\frac{v_{pol}}{\gamma}, \quad \delta n_2 = \frac{n_2}{L_2}\frac{v_{pol}}{\gamma} \tag{2.43}$$

Since above the base, L_2 is negative whereas L_1 is positive, the value of δn_2 and δn_1 are negative and positive respectively. The ratio of δn_1 to δn_2 is thus:

$$\frac{\delta n_2}{\delta n_1} = \left(\frac{n_2}{n_1}\right)\left(\frac{L_1}{L_2}\right) \tag{2.44}$$

It is clear from expression (2.42) that above the base, ratio is less than unity since $m_2/m_1 > 1$. It means that though the current density is larger for the two ions-electron plasma, the divergence in current density is less than its value for one ion-electron plasma. It leads to the reduction in the growth rate according to (2.41). Note that the reduction in δJ is maximum for density ratio equals to unity, as similar to the growth rate.

The increase in conductivity

The Pedersen conductivity for two ions-electron plasma is given by eq. (2.40). Obviously the conductivity is increased with the introduction of second massive dominant ion NO^+. Since the enhanced conductivity causes more shielding of polarization field which drives the instability, it is obvious that the growth rate is reduced in present case. The effect of scale height is already discussed in section (2.2.2). In the presence of NO^+ with negative scale height, O^+ scale height, which enters into the one ion-electron growth rate, becomes smaller than electron scale height. It otherwise assumes value equals to electron scale height.

It follows from above discussion that less divergence of current density and more conductivity causes the reduction in growth rate when NO^+ ions are introduced with negative scale height above the base.

2.3.3 The comparison of growth rate with damping rate

In order to know whether the reduction in growth rate discussed above imposes any severe condition on onset of instability, we need to compare it with the damping rate which arises due to the chemical loss of the ions. Based on the analysis of [76], for the region where both the atomic and molecular ions are present and also the perturbation analysis by Huba et al; [39], we believe that the following rate can be taken as the damping rate (ν_R)

$$\nu_R = \frac{\beta.\alpha(n_e + n_2)}{\beta + \alpha(n_e + n_2)} \tag{2.45}$$

where β is the loss rate of atomic oxygen ion controlled by charge exchange process while α is the reaction rate constant for dissociative recombination reaction. The effective recombination rate ν_R reduces to $2.\alpha.n_e$ in the region where molecular ions are dominant and to β in the region where atomic ions are dominant, which are similar to the analysis of Huba et al; [39]. The ratio of growth rate given by expression (2.34) to damping rate is:

$$\frac{\gamma}{\nu_R} = \frac{g}{\nu_{in}}\left[\frac{(\beta + \alpha(n_1 + 2n_2))}{\beta.\alpha(n_1 + 2n_2)}\right]\left[\frac{n_1\frac{m_1}{L_1} + n_2\frac{m_2}{L_2}}{n_1 m_1 + n_2 m_2}\right]$$

In fig. 3 the ratio is plotted for decreasing values of n_2/n_1. The decreasing value of n_2/n_1 correspond to increasing altitude. At 340 km altitude, both the ion densities are $10^3/cm^3$

and with altitude they vary exponentially with their corresponding scale heights which are 7.5 km and -30 km for O^+ and NO^+ ions respectively. The L_1 value is obtained by knowing L_e and L_2 and using eq.(2.5) with density ratio equals to unity. The suitable altitude profile of ν_{in} and β are taken. The growth rate is found to be larger than the damping rate. Moreover near the base, its value is one order larger than ν_R whereas at higher altitude it is of two order larger than ν_R.

2.3.4 The comparison of time scale associated with instability and life time of both the ions

Though the growth rate is found to be larger than the damping rate, it is yet far to state that the instability grows in all the constituents until one found it to be larger than the individual loss rates of these constituents. Above the base of F region, the O^+ ions life time β^{-1} is large compared to the time taken for its transportation by any mechanism. They respond to any transport process due to their long life time. However for NO^+ ions, scenario is quite different. It was shown by Anderson and Rusch [3] that they are in chemical equilibrium above the base while in dynamical equilibrium below the base. Above the base they are short lived ions with life time $\sim (\alpha n_e)^{-1}$ and they becomes even more short lived as altitude increases. The short life time of NO^+ ions makes it difficult for them to respond to any transport process. In order for them to respond to CRT instability, the linear growth rate γ given by expression (2.34) must be larger than the recombination rate $\alpha(n_1 + n_2)$. In fig. 4 the ratio

$$\frac{\gamma}{\alpha(n_1+n_2)} = \frac{g}{\nu_{in}\alpha}\frac{[n_1m_1/L_1 + n_2m_2/L_2]}{(n_1m_1+n_2m_2)(n_1+n_2)} \tag{2.46}$$

is plotted for decreasing value of ratio n_2/n_1. The ratio is found to be slightly larger than unity for unity density ratio. As the density ratio decreases, the ratio increases but remains always less than 10. For very small density ratio, the ratio decreases rapidly and even becomes less than unity. The two phases, increasing and decreasing, are caused by varying importance of growth rate and loss rate. Both the rates increase with decreasing density ratio. The increase in growth rate dominated for increasing phase while increase in loss rate dominates for decreasing phase as O^+ or electron density is large in this phase. Thus where NO^+ ions are significant both the rates are comparable and where it is insignificant the loss rate dominates over growth rate.
The investigation of last two sections implies that the instability can grow in the plasma densities because it is larger than damping rate. In spite that the NO^+ ions are short lived ions above the base and having negative scale height, the instability also grows in the profile of it. The reason for this result can be ascribed as follows: In the presence of steep (positive) gradients in the electron and O^+ ion density profiles, the plasma instability processes grow and the irregularities are generated in them. In order to maintain the charge neutrality, the perturbed potential structures in the plane perpendicular to Earth's magnetic field get altered suitably in the presence of negative molecular ion density profile, similar to the investigation by Sekar et al; [86] provided enough NO^+ ions are available to effect the potential. The altered potential structures redistribute the molecular ion densities to generate the irregularities in them.

In this context, it is of interest to recall the satellite measurements [60] which revealed the

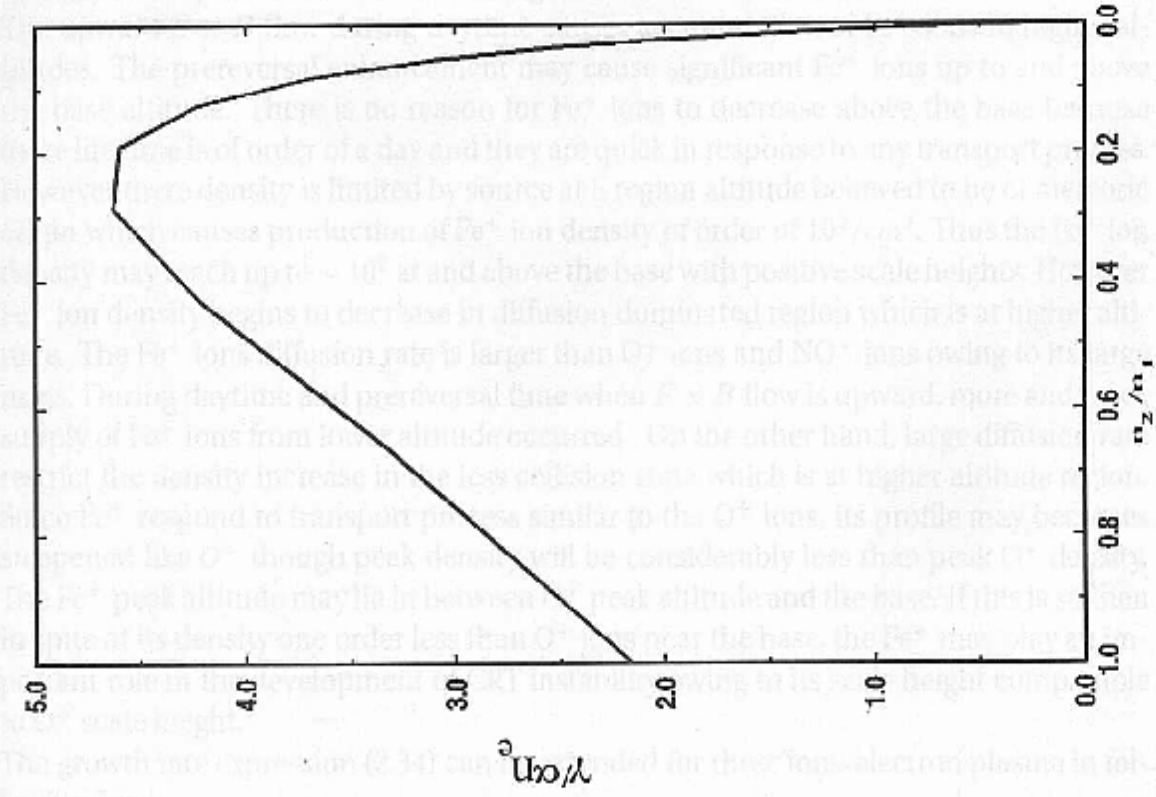

Figure 4.

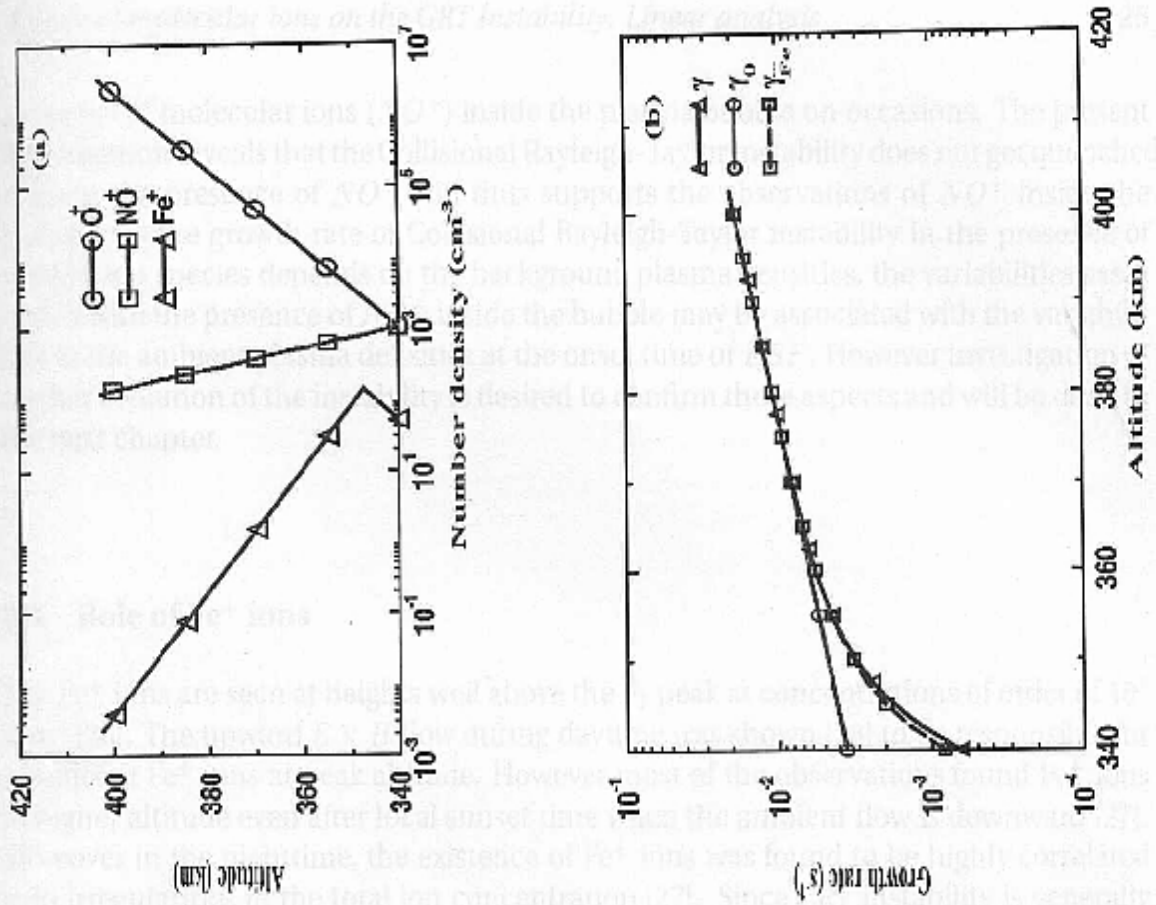

Figure 5.

presence of molecular ions (NO^+) inside the plasma bubble on occasions. The present investigation reveals that the Collisional Rayleigh-Taylor instability does not get quenched even in the presence of NO^+ and thus supports the observations of NO^+ inside the bubble. As the growth rate of Collisional Rayleigh-Taylor instability in the presence of double-ion species depends on the background plasma densities, the variabilities associated with the presence of NO^+ inside the bubble may be associated with the variabilities in the ambient plasma densities at the onset time of ESF. However investigation of further evolution of the instability is desired to confirm these aspects and will be dealt in the next chapter.

2.4 Role of Fe^+ ions

The Fe^+ ions are seen at heights well above the F_2 peak at concentrations of order of 10^2 /cm^3 [26]. The upward $E \times B$ flow during daytime was shown [28] to be responsible for significant Fe^+ ions at peak altitude. However most of the observations found Fe^+ ions to higher altitude even after local sunset time when the ambient flow is downward [27]. Moreover in the nighttime, the existence of Fe^+ ions was found to be highly correlated with irregularities in the total ion concentration [27]. Since CRT instability is generally believed to be the causative mechanism for irregularities in total ion concentration and transportation of plasma to topside during nighttime, it is of interest to deal with this instability in the presence of Fe^+ ions along with NO^+ and O^+ ions also.
The upward $E \times B$ flow during daytime causes accumulation of Fe^+ ions to higher altitudes. The prereversal enhancement may cause significant Fe^+ ions up to and above the base altitude. There is no reason for Fe^+ ions to decrease above the base because there life time is of order of a day and they are quick in response to any transport process. However there density is limited by source at E region altitude believed to be of meteoric origin which causes production of Fe^+ ion density of order of $10^2/cm^3$. Thus the Fe^+ ion density may reach up to $\sim 10^2$ at and above the base with positive scale heights. However Fe^+ ion density begins to decrease in diffusion dominated region which is at higher altitude. The Fe^+ ions diffusion rate is larger than O^+ ions and NO^+ ions owing to its large mass. During daytime and prereversal time when $E \times B$ flow is upward, more and more supply of Fe^+ ions from lower altitude occurred . On the other hand, large diffusion rate restrict the density increase in the less collision zone which is at higher altitude region. Since Fe^+ respond to transport process similar to the O^+ ions, its profile may becomes steepened like O^+ though peak density will be considerably less than peak O^+ density. The Fe^+ peak altitude may lie in between O^+ peak altitude and the base. If this is so then in spite of its density one order less than O^+ ions near the base, the Fe^+ may play an important role in the development of CRT instability owing to its scale height comparable to O^+ scale height.
The growth rate expression (2.34) can be extended for three ions-electron plasma in following form:

$$\gamma_{Fe} = \frac{g}{\nu_{in}(n_1 m_1 + n_2 m_2 + n_3 m_3)}\left[\frac{n_1 m_1}{L_1} + \frac{n_2 m_2}{L_2} + \frac{n_3 m_3}{L_3}\right] \tag{2.47}$$

where n_3, m_3 and L_3 are the number density, mass and scale height of Fe^+ ions. In fig. 5(b), the growth rate is plotted with the inclusion of Fe^+ ions as third dominant ions.

The density profiles of all three ions are shown in fig. 5(a). The Fe^+ density at the base is taken as 50 $/cm^3$ and upto 350 km its scale height is assumed to be equal to O^+ scale height which is 7.5 km. Above 350 km, its scale height is negative owing to the diffusion. The same ratio for two ions-electron plasma is also plotted. At the base (340 km), the density ratio n_2/n_1 is unity and as altitude increases the density ratio decrease. The variation in ν_{in} is similar to what was taken for earlier cases. Instead of plotting the variations of growth rate with both density ratio and ν_{in}, its variation with altitude is plotted in fig. 5(b) which takes both the variations into account. Moreover for comparison, growth rates ; γ and γ_o, are also plotted. Interestingly, the growth rate, γ_{Fe} is somewhat larger than γ near the base and as altitude increases, both merge to growth rate γ_o. The cause for the increase in γ_{Fe} near the base can be attributed to the enhanced current density divergence as compared to its value for two ions-electron plasma which takes the following form in present case:

$$\delta J = -(1/B)(m_1\delta n_1 + m_2\delta n_2 + m_3\delta n_3)g$$

where $\delta n_i's$ are inversely proportional to their corresponding scale heights as evident from eq. (2.43). Since L_3 is positive, δn_3 is also positive. Thus the inclusion of Fe^+ ions with positive scale height cause the enhancement in divergence of current density. The enhanced divergence in current density cause the increase in growth rate according to equation:

$$\gamma\delta n_e = \frac{n_e}{L_e}\frac{\delta J}{\sigma B}$$

derived in section (2.3.2). It is to be noticed that the conductivity is increased with the inclusion of third carrier, but its effect is not as pronounced to overcome the effect of divergence in current density.
It is interesting to note the observation by Hanson and Sanatini [27] where they found the presence of Fe^+ ions as a necessary condition for irregularities. It is shown here that indeed the inclusion of Fe^+ ions with positive scale height causes the increase in growth rate which otherwise would have decreased further owing to the presence of NO^+ ions with negative scale height. Further the irregularities in all three ions were seen on the topside. Since γ is greater than damping rate as found earlier, the growth rate, γ_{Fe} greater than γ means the instability indeed grow in all the ionic species causing irregularities in densities.

2.5 Summary and Conclusion

The growth rate expression for the GRT instability for two ions-electron plasma is derived by first order perturbation analysis. The further investigation with CRT instability reveals that:
(1)The growth rate is dependent on number densities of both the species. This is in contrast to the expression for one ion-electron plasma wherein the growth rate is independent of the number densities.
(2)The growth rate is found to be positive for all values of density ratio n_2/n_1 in the bottomside of F region.
(3) The result obtained using the expression with the equatorial night-time F region conditions, reveals that the growth rate of Collisional Rayleigh-Taylor instability reduces with

the introduction of second dominant ion species and never exceeds the growth rate corresponding to one ion-electron plasma.
(4) The maximum reduction is found for value of density ratio n_2/n_1 close to one, i.e, in the region where significant NO^+ ions are present.
(5) The causes for reduction in growth rate are the reduced divergence of current density and enhanced conductivity.
(6) The growth rate is found to be larger than the damping rate by an order of magnitude or more throughout the altitude region.
(7) The growth rate larger than the damping rate for density ratio closer to one implies that irregularities could be generated in NO^+ ion density in the altitude region where they are in significant amount. Moreover the growth rate is comparable to the loss rate of short lived NO^+ ions at altitudes where they are significant. Such situation may allow the irregularities in NO^+ ion density to grow nonlinearly. It calls for nonlinear investigation which is carried out in next chapter.
(8) Since the growth rate is highly sensitive to the density ratio and scale height ratio which are the varying parameter for F region of ionosphere, the day-to-day variability in the occurrence of NO^+ along with O+ ions can be attributed to these parameter. The nonlinear investigation is necessary to understand such characteristics which could possibly match the observations [10, 60, 63].
(9) The role of Fe^+ ions is discussed and they are found to increase the growth rate as compared to two ions-electron plasma under the circumstances which are quite possible in F region of ionosphere. The findings are consistent with the observations [26, 27].

2.6 Figure captions

- Fig. 1(a): The variation in growth rate, γ, with variations in density ratio, n_2/n_1 and ion-neutral collision frequency, ν_{in}.
- Fig. 1(b): The variation in growth rate, γ_o, with variations in density ratio, n_2/n_1 and ion-neutral collision frequency, ν_{in}.
- Fig. 2: The growth rate ratio, $\frac{\gamma}{\gamma_o}$, vs. the density ratio, n_2/n_1.
- Fig. 3: The growth rate to damping rate ratio vs. the density ratio, n_2/n_1.
- Fig. 4: The growth rate to NO^+ loss rate ratio vs. the density ratio, n_2/n_1.
- Fig. 5(a): The altitude profile of O^+, NO^+ and Fe^+ ion number densities.
- Fig. 5(b): The variations in growth rates , γ_o, γ and γ_{Fe} with altitude.

Chapter 3

Effects of molecular ions on the GRT instability : Nonlinear evolution

In previous chapter, the linear aspects of GRT instability are investigated by considering the bottomside of F region as two ions-electron plasma. The O^+ and NO^+ ions are considered as the dominant ionic species. The investigation reveal that the growth rate is larger than the O^+ loss rate throughout the altitudes while it is comparable to NO^+ loss rate of over the altitudes where they are significant. Moreover, the growth rate is found to be larger than the damping rate. Hence the instability grows in both the ion densities. However in order to know the evolution of the instability, the nonlinear investigation is required.
The earlier nonlinear simulation model [81, 83] of GRT instability deals with the dynamics of O^+ ions alone by considering it as the dominant ion in the F region. It was shown by these investigations that the GRT instability acts in such a way that regions of low plasma density below the F layer peak are transported to altitudes well above the F_{peak} and seen as plasma depletions or bubbles which confirm the observations [60, 109, 99, 97, 47]. The ion composition within the depletions has been the subject of a number of investigations. Typically, satellite-mass spectroscopic observations [60] has shown that the ion composition can be vastly different inside and outside the depletion. The atomic O^+ ions are depleted by as much as a factor of 10^3 to a concentration below that of the molecular NO^+ ions. The NO^+ ion was found to be in the topside and dominant in the O^+ depleted region. Since the O^+ depletions on the topside are caused by nonlinear evolution of GRT instability, it becomes important to study its evolution in presence of NO^+ ions also.
In present chapter, the nonlinear evolution of GRT instability for two ions-electron plasma is investigated. The numerical simulation model [71, 83] for one ion-electron plasma is suitably modified for two ions-electron plasma for present investigation.

3.1 Numerical simulation model

3.1.1 Set of equations

The night time equatorial ionosphere is considered in a slab geometry which means that the curvature of the Earth's magnetic field is ignored. The positive unit vectors $\hat{x}$, $\hat{y}$ and $\hat{z}$ of the Cartesian co-ordinate system are directed along westward, upward and northward respectively. The following plasma fluid equations, that govern the motions of the two positive ions (dominant ion is denoted by suffix 1 while the second ion is denoted by suffix 2) and electrons (denoted by suffix e) whose masses are represented as m_1, m_2 and

m_e respectively, are considered:

$$\left(\frac{\partial \vec{v}_1}{\partial t}\right) = \left(\frac{e}{m_1}\right).\left(\vec{E} + \vec{v}_1 \times \vec{B}\right) - \nu_{in}.\left(\vec{v}_1 - \vec{W}\right) + \vec{g} \tag{3.1}$$

$$\left(\frac{\partial \vec{v}_2}{\partial t}\right) = \left(\frac{e}{m_2}\right).\left(\vec{E} + \vec{v}_2 \times \vec{B}\right) - \nu_{in}.\left(\vec{v}_2 - \vec{W}\right) + \vec{g} \tag{3.2}$$

$$\left(\frac{\partial \vec{v}_e}{\partial t}\right) = \left(\frac{-e}{m_e}\right).\left(\vec{E} + \vec{v}_e \times \vec{B}\right) - \nu_{en}.\left(\vec{v}_e - \vec{W}\right) + \vec{g} \tag{3.3}$$

$$\frac{\partial n_1}{\partial t} = l_1 - \nabla.(n_1.\vec{v}_1) \tag{3.4}$$

$$\frac{\partial n_2}{\partial t} = p_2 + l_2 - \nabla.(n_2.\vec{v}_2) \tag{3.5}$$

$$n_e = n_1 + n_2 \tag{3.6}$$

$$\vec{E} = -\nabla\phi \tag{3.7}$$

$$\nabla.\vec{J} = 0 \tag{3.8}$$

where,

$$\vec{J} = e.(n_1.\vec{v}_1 + n_2.\vec{v}_2 - n_e.\vec{v}_e) \tag{3.9}$$

The symbols n_1, n_2 and n_e represent number densities of dominant atomic oxygen ions, molecular ions and electrons respectively, while their velocities, in the same order, are represented by $\vec{v}_1$, $\vec{v}_2$ and $\vec{v}_e$. Here 'e' corresponds to the magnitude of the charge. The potential, electric field and current density are denoted by ϕ, $\vec{E}$ and $\vec{J}$ respectively.
The continuity equation for electron is not considered because its number density can be derived from charge neutrality condition. The expressions for loss terms l_1 and l_2 are:

$$l_1 = -\beta n_1, l_2 = -\alpha(n_1 + n_2)n_2$$

where $\beta$is the rate of charge exchange reaction and α is the volume rate of dissociative recombination. The charge exchange reaction produces NO^+ ions with the rate p_2 = -l_1.
The momentum equations are used to obtained the steady state velocities in terms of forces:

$$\vec{v}_1 = \frac{\vec{E}\times\vec{B}}{B^2} + \frac{\nu_{in}}{\Omega_1^2}.\frac{e}{m_1}\vec{E} + \frac{m_1}{e}.\frac{\vec{g}\times\vec{B}}{B^2} + \frac{\nu_{in}}{\Omega_1}.\frac{\vec{W}\times\vec{B}}{B} + \frac{\nu_{in}}{\Omega_1^2}.\vec{g} + \frac{\nu_{in}^2}{\Omega_1^2}.\vec{W} \tag{3.10}$$

$$\vec{v}_2 = \frac{\vec{E}\times\vec{B}}{B^2} + \frac{\nu_{in}}{\Omega_2^2}.\frac{e}{m_2}\vec{E} + \frac{m_2}{e}.\frac{\vec{g}\times\vec{B}}{B^2} + \frac{\nu_{in}}{\Omega_2}.\frac{\vec{W}\times\vec{B}}{B} + \frac{\nu_{in}}{\Omega_2^2}.\vec{g} + \frac{\nu_{in}^2}{\Omega_2^2}.\vec{W} \tag{3.11}$$

$$\vec{v}_e = \frac{\vec{E}\times\vec{B}}{B^2} \tag{3.12}$$

For electrons, the contribution from the other terms are negligible as $\Omega_e >> \nu_{en}$. The last two terms in both the ion velocities are very small compared to other terms and can be neglected.
The current density, from eq. (3.9), can then be written as:

$$\vec{J} = \frac{(n_1m_1 + n_2m_2)}{B^2}(\vec{g} + \nu_{in}\vec{W}) \times \vec{B} + \frac{(n_1m_1 + n_2m_2)}{B^2}\nu_{in}\vec{E} \tag{3.13}$$

In obtaining the above expression the charge neutrality condition is used.

The electrostatic field $\vec{E}$ is given by eq. (3.7). With the perturbation $(-\nabla\phi)$ in the electric field over ambient field $\vec{E}_o$, the current conservation equation can be written as:

$$\nabla.\left\{\frac{(n_1m_1+n_2m_2)}{B^2}(\vec{g}+\nu_{in}\vec{W})\times\vec{B}+\frac{(n_1m_1+n_2m_2)}{B^2}\nu_{in}(\vec{E}_o-\nabla\phi)\right\}=0$$

For initial perturbation only in the zonal direction, the equation becomes,

$$\nabla.[\nu_{in}(n_1.m_1+n_2m_2)\nabla\phi]=B.[-g+W_y.\nu_{in}+(E_{xo}/B)\nu_{in}].\frac{\partial\sum_{i=1}^{2}(n_i.m_i)}{\partial x} \qquad (3.14)$$

where E_{xo} and W_y are the westward field and upward wind respectively. It describes the spatial variation of polarization potential. The temporal evolution of number densities of both the ions are obtained by solving the continuity equations separately:

$$\frac{\partial n_1.}{\partial t}-\frac{\partial}{\partial x}[(n_1/B).(E_{yo}+\frac{\partial\phi}{\partial y})]+\frac{\partial}{\partial y}[(n_1/B).(-E_{xo}+\frac{\partial\phi}{\partial x})]=-\beta.n_1 \qquad (3.15)$$

$$\frac{\partial n_2.}{\partial t}-\frac{\partial}{\partial x}[(n_2/B).(E_{yo}+\frac{\partial\phi}{\partial y})]+\frac{\partial}{\partial y}[(n_2/B).(-E_{xo}+\frac{\partial\phi}{\partial x})]=\beta.n_1-\alpha.(n_1+n_2).n_2 \qquad (3.16)$$

where E_{yo} is the vertical electric field. For present investigation, only the effects of gravity and zonal electric field E_{xo} are considered.

3.1.2 The simulation plane

The numerical calculations are performed in two-dimensional Cartesian plane where the positive $\hat{x}$ and $\hat{y}$ axes represent westward and upward direction respectively. The differential equations are solved over the region of 400 km east to 400 km west in zonal direction and over 182 to 532 km in vertical direction. The grid sizes are chosen to be uniform with the values of Δx = 5 km and Δy = 2 km. The vertical line corresponding to x=0 km is referred as the zero reference longitude for the future discussion.

3.1.3 The boundary conditions and initial conditions

As the problem of interest is to study the growth of the periodic perturbation in ion densities in zonal direction, periodic boundary conditions are imposed on both n_i (i=1,2) and ϕ in the zonal direction. In vertical direction, transmitive boundary conditions on number densities

$$\frac{\partial n_i}{\partial y}=0$$

and Neumann boundary conditions on ϕ

$$\frac{\partial\phi}{\partial y}=0$$

are imposed.

3.1.4 The numerical scheme

The numerical scheme adopted by sekar [90] for one ion-electron plasma is used for present investigation. The potential equation is solved using a line by line successive over relaxation method by maintaining the skew symmetry in the zonal direction.
The continuity equations are solved by explicit finite difference method (Lax-friedrichs and Lax-Wandroff schemes) with flux corrected transport (FCT) technique [111].

3.1.5 The inputs for simulation

The basic inputs required to the simulation are
(1) the altitude profile of ν_{in},
(2) the altitude profile of β,
(3) the altitude profile of number densities of both the ions,
(4) the temporal variation of zonal electric field E_{zo}.
(6) the value of α which is taken to be equal to $1.6 \times 10^{-7} cm^3 sec^{-1}$.
The altitude profiles of both the ions, ν_{in}, β and temporal variation of ambient drift $(= \frac{E_{zo}}{B})$ are shown in fig. 1.

The initial density profiles of O^+ and NO^+ are similar to the profiles observed by Narcisi and Szuszczewicz [63] during PLUMEX experiment. At the base (342 km), O^+ and NO^+ are 50%-50% with density equals to $3.9 \times 10^3 cm^{-3}$. At the F_{peak} (448 km), O^+ and NO^+ concentrations are $5.9 \times 10^5 cm^{-3}$ and $1.1 \times 10^2 cm^{-3}$ respectively.

3.1.6 The form of initial perturbation

The density perturbation is chosen of the form:

$$n_{1,2}(x, y) = n_{01,02}(y)(1. - a\cos[2\pi x/\lambda])$$

where

$$a = \frac{\delta n_1}{n_{01}} = \frac{\delta n_2}{n_{02}}$$

is the amplitude of initial perturbation defined as the fractional change in the number density. The λ is the wavelength of perturbation. The initial density perturbations in both the ions is shown in fig. 3(a). The isodensity contours shown in fig. 3(b,c), for O^+ and NO^+ ions respectively, is another way of representing these perturbations. For O^+ ions, starting from the lower most contour with density value 10^3, the density values of successive contours are $10^{3.5}$, 10^4, $10^{4.5}$ and 10^5 /cm^3. For NO^+ ions, starting from lower most contour with density value 1.5×10^3, the density values of successive contours are 10^3, 1.5×10^2 and 10^2 /cm^3. The similar choice is maintained throughout the investigation. The slight modulations, upwelling and downwelling, of contours in fig 3(b,c) correspond to initial amplitude of perturbation, 5%, with respect to reference density values at different altitudes. The characteristics of these modulations are remarkably different for those O^+ and NO^+ contours which fall on altitudes above the base. Wherever

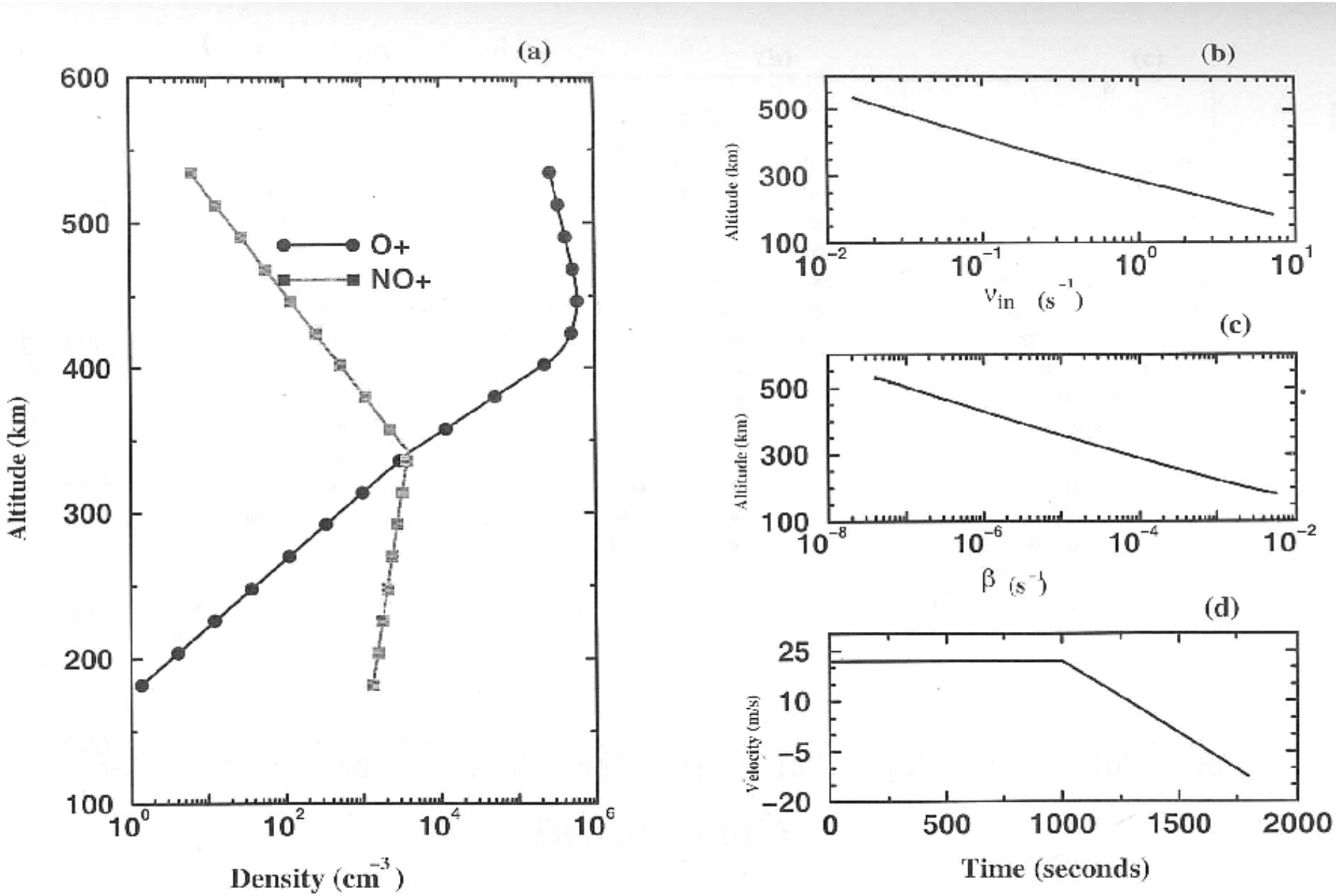

Figure 1.

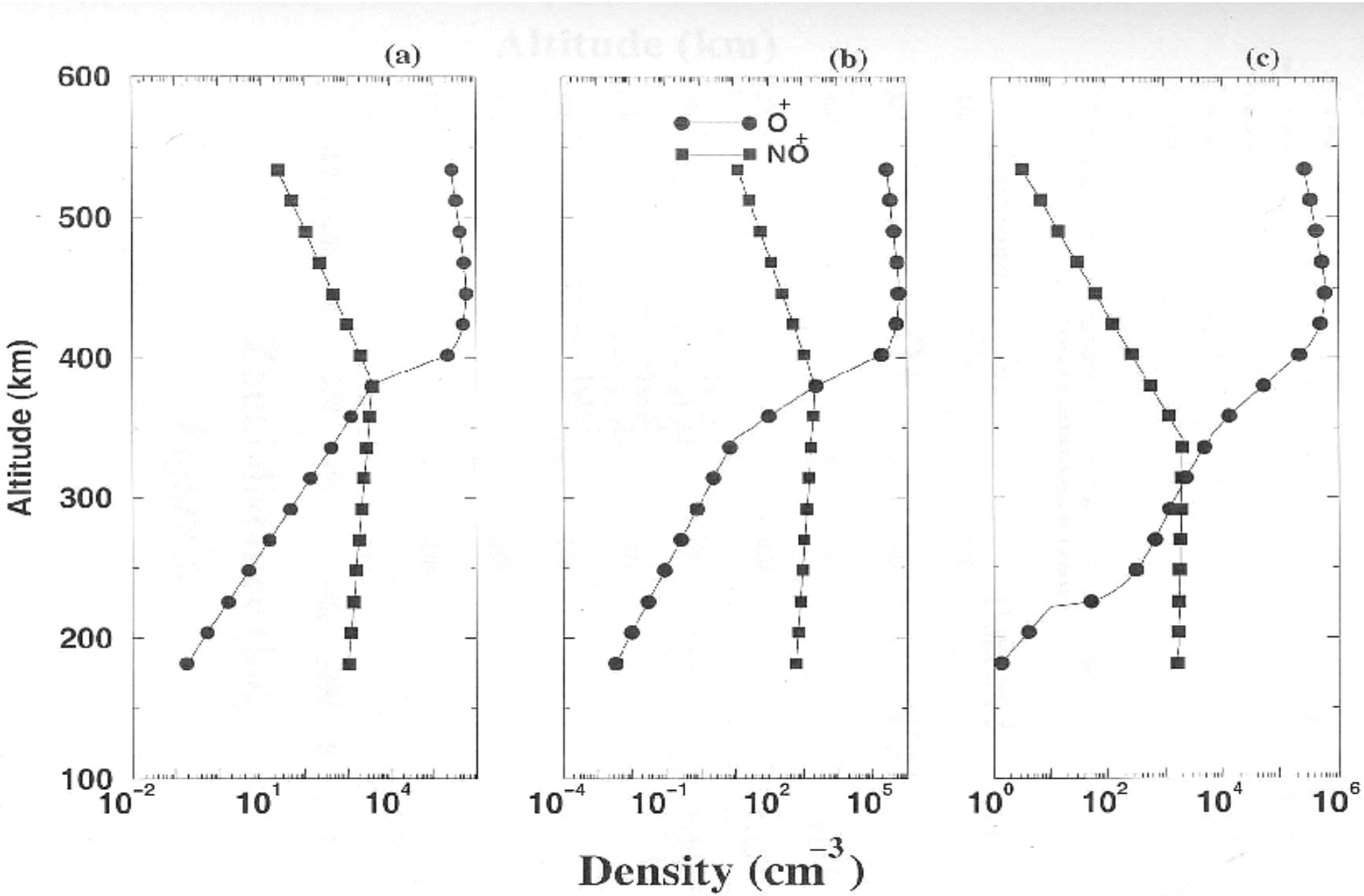

Figure 2.

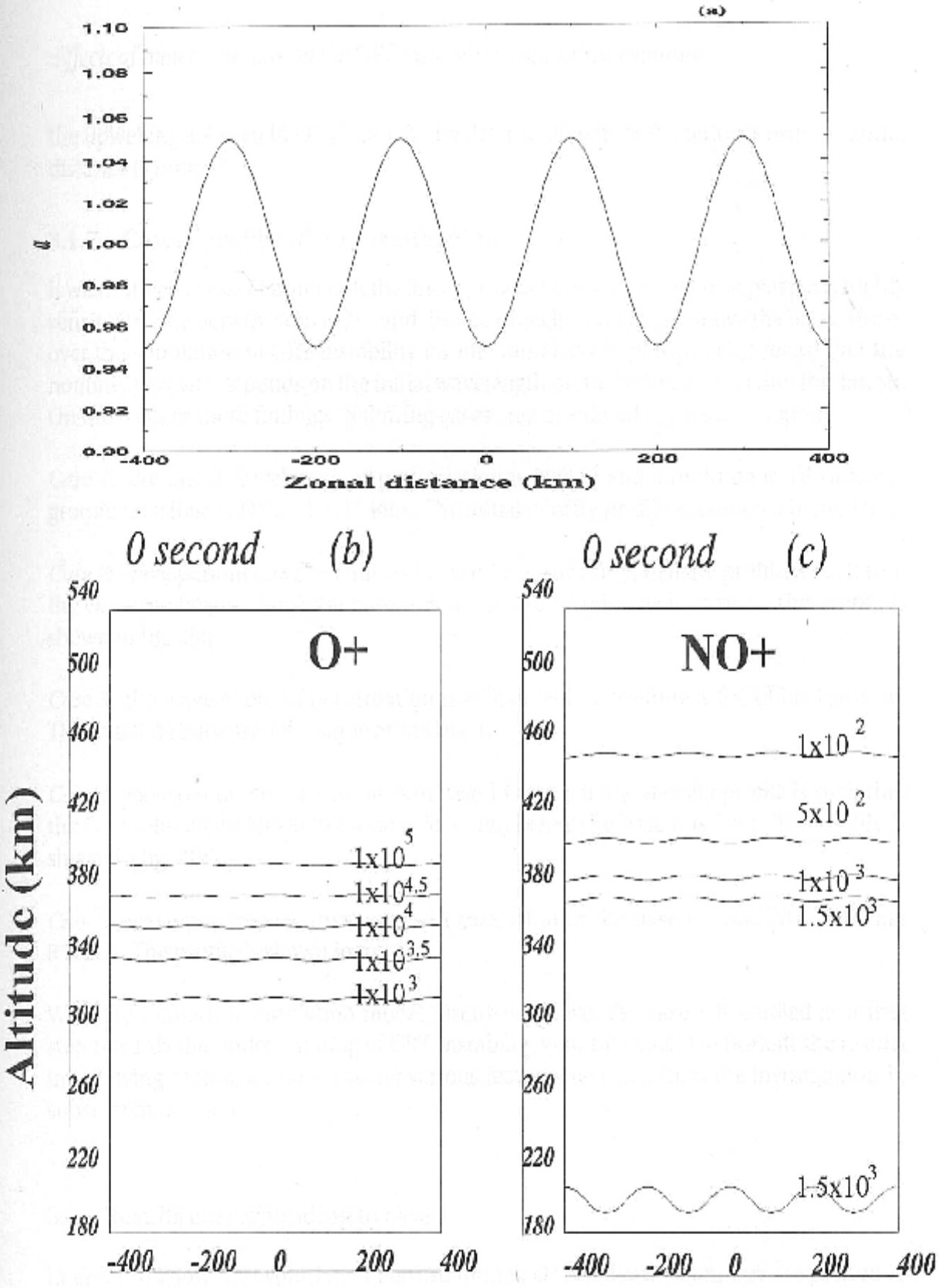

Figure 3.

the upwelling are seen in O^+ contours, the downwelling in NO^+ contours over the zonal distance is noticed.

3.1.7 Cases considered for investigation

It was noticed in last chapter that the linear growth for two ions-electron plasma is highly sensitive to the density ratio n_2/n_1 and the scale height ratio L_2/L_1 above the base. Moreover the simulation of GRT instability for one ion-electron plasma [112] reveal that the nonlinear growth depends on the initial wavelength perturbation used in the simulation. On the basis of these findings, following cases are considered in present chapter:

Case 1: the initial wavelength of perturbation is 200km and amplitude is 5% of background densities of O^+ and NO^+ ions. The initial density profile is as shown in fig. 1(a).

Case 2: wave parameters are same as in case 1 but the initial density profile is such that the O^+ scale height above the base is 5km instead of 15km as in case 1. The profile is shown in fig. 2(a).

Case 3: the wavelength of perturbation is 600km with amplitude is 5% of background. The initial density profile is same as in Case 1.

Case 4: wave parameters are same as in case 1 but the initial density profile is such that the O^+ scale height above the base is 5km and below the base it is 7km. The profile is shown in fig. 2(b).

Case 5: wave parameters are same as in case 1 but at the base O^+ and NO^+ ions are 85-15%. The profile is shown in fig. 2(c).

With the numerical simulation model discussed above, the case 1 is studied as a first step towards the understanding of GRT instability with two ions. We present the results in following section and discuss the various features revealed from the investigation in subsequent section.

3.2 Results corresponding to case 1

In order to know the evolution of perturbation in O^+, isodensity contours are plotted in fig. 4(a-f) for different phases of evolution. The different phases of evolution chosen for investigation are 100, 300, 500, 700, 900 and 1000 seconds which are written in the top of each plot. The growing upwelling and downwelling structures of contours are seen throughout the phase of evolution.
However, during first 500s, the structures are found to grow slowly while they grow rapidly later. The evolution thus can be divided into the two phases, initial phase of evolution ($<$ 500s) and later phase of evolution ($>$ 500s).
During initial phase, the structures are seen as slight modulation over initial isodensity contours. They grow slowly but not significantly to become prominent over the initial density contours. During later phase of evolution, these structures however grow rapidly

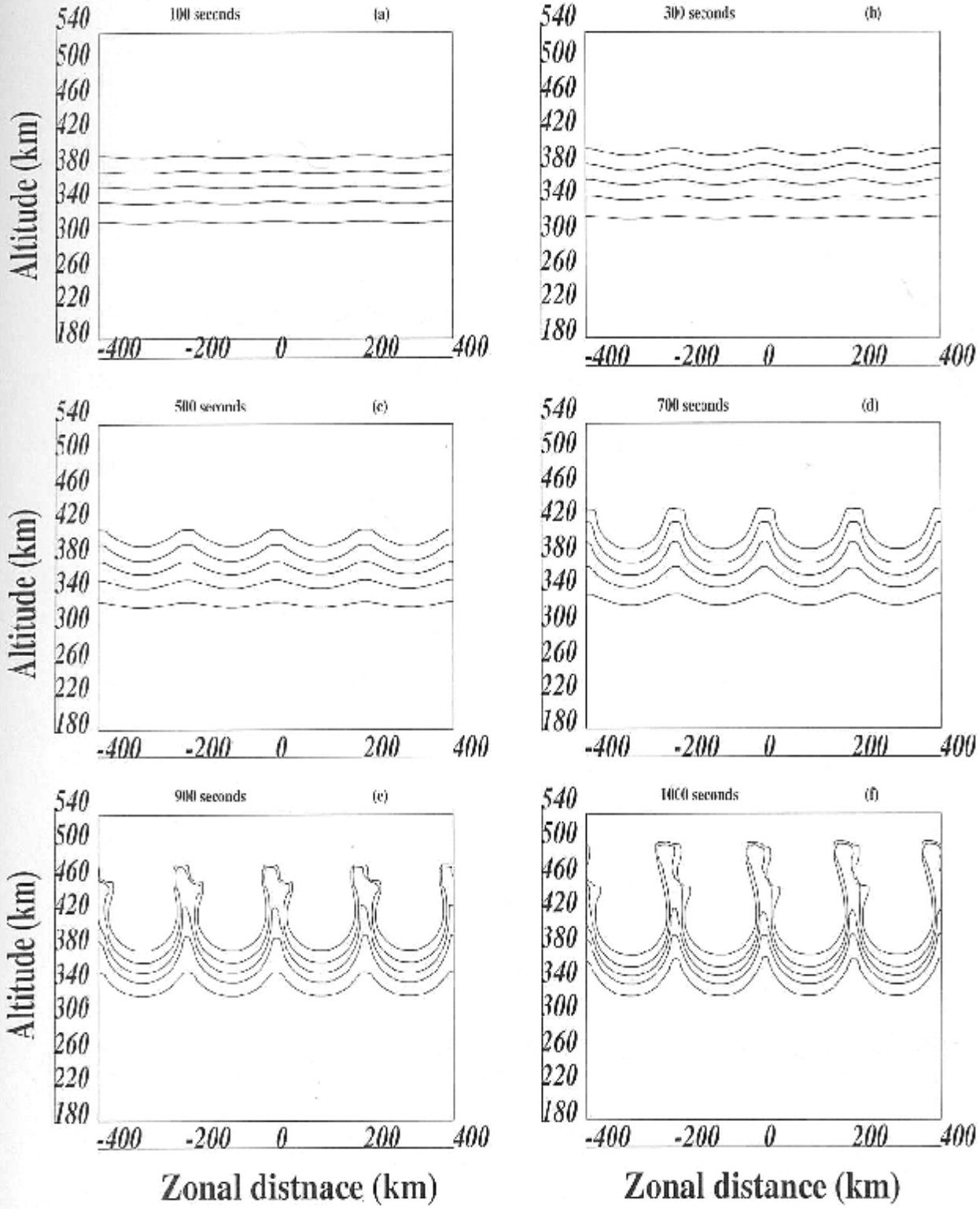

The values of isodensity contours from bottom to top are $1.0x10^{3}$, $1.0x10^{3.5}$, $1.0x10^{4}$, $1.0x10^{4.5}$ and $1.0x10^{5}$ cm^{-3}.

Figure 4

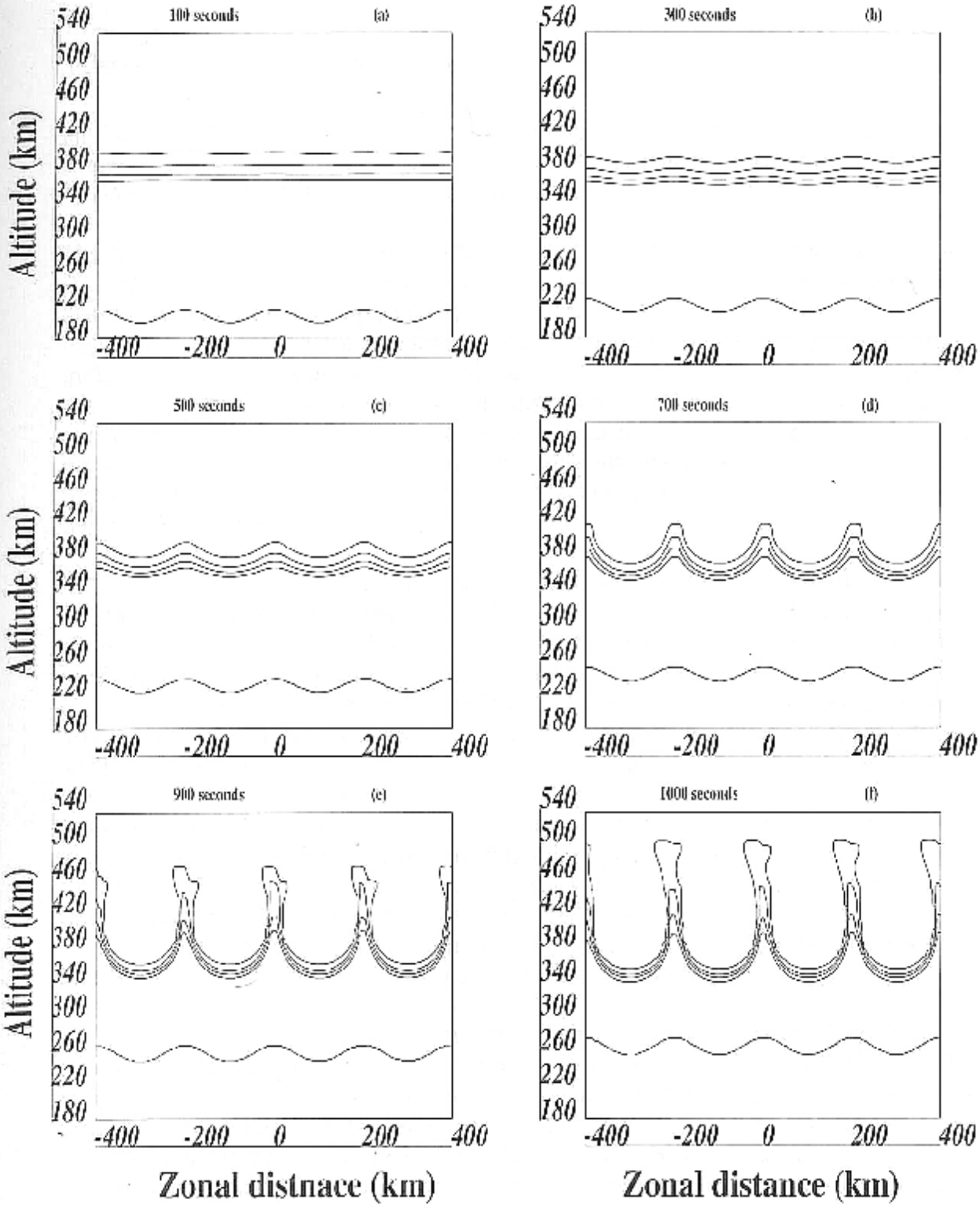

The values of isodensity contours from bottom to top are 1.5×10^3, 1.5×10^3, 1.0×10^3, 5.0×10^2 and 1.0×10^2 cm^{-3}.

Figure 5

and become prominent over initial density contours. In the upwelling structures corresponding to density contours of values $10^{4.5}$ and 10^5 just reached up to the F_{peak} altitude, 460 km, at 900s and at 1000s they moved to the topside.

The NO^+ isodensity contours are plotted in fig. 5 (a-f) for similar time sequence as for O^+. Interestingly the initially downwelling (upwelling) structures in fig. 3(c) above the base are now appeared as upwelling (downwelling) at 100s and continue to grow during subsequent times. However, the structures grow rapidly and become prominent over initial density contours only after 500s similar to the case for O^+ ions. More surprisingly these contours are confined to shorter altitude range at 100s than at 0s. They continue to confine further during initial phase but not during later phase of evolution. The later phase of evolution is similar to O^+ ions isodensity contours. At 900s, the upwelling structure corresponding to density value of 10^2 is reached up to F_{peak} altitude and at 1000s, they moved to the topside.

In fig.6 (a), the altitude profile of O^+ ion density inside the upwelling structure is shown for similar choice of time sequence as earlier. During initial phase of evolution, the profile is shifted to higher altitudes and no appreciable change is seen in the shape of the profile as compared to initial altitude profile shown in fig. 1(a).
However, at 700s during later phase, the O^+ density profile to becomes steepened above 400km altitude compared to initial density profile. Below this altitude, the profile is less steepened. In subsequent times, the profile becomes more and more steepened but the altitude above which it occurred also shifted to higher altitude.
In fig. 6 (b), the altitude profile of NO^+ ion density inside the upwelling structure is depicted. Strikingly, its shape changes during initial phase too unlike O^+ case. At 100s, the NO^+ ion density profile above the altitude of 350 km becomes steepened compare to initial density profile. At 300s, it is steepened than ever. At 500s, however the profile becomes less steepened again and continue for subsequent times. Moreover below 350km altitude, the density gradient decreases monotonically with time.

In fig. 7(a,b), the zonal density variation of O^+ ions at different phases of evolution are shown. The altitude is kept unchanged at 400km. Throughout the evolution, the periodic variations with respect to the reference density value are noticed. Moreover the densities are found to be depleted in the region where upwelling structures are seen. However the reference density value and the degree of depletion i.e. the fractional amount by which it is depleted from the reference value of density, varies with time. The reference density value decreases throughout the phase of evolution. On the other hand the degree of depletion increases with time. During initial phase of evolution, it increases slowly and its value is also less. In later phase its value increases rapidly to large value. For example, at 500s, the degree of depletion is 40% which is rapidly increased to 80% at 700s. At 900s, its value further increased to 95%.
In fig. 7 (c,d) the zonal density variations of NO^+ ions are depicted. The variation reveal that the NO^+ ion density are enhanced in the region where upwelling structures are seen. The reference density value and the degree of enhancement both varies with time. Both the values lower down up to 300s, just begin to increase at 500s and continue to increase during later times. At 900s, the degree of enhancement becomes 95 %.

The density variations of O^+ and NO^+ ions along the assumed path over the simula-

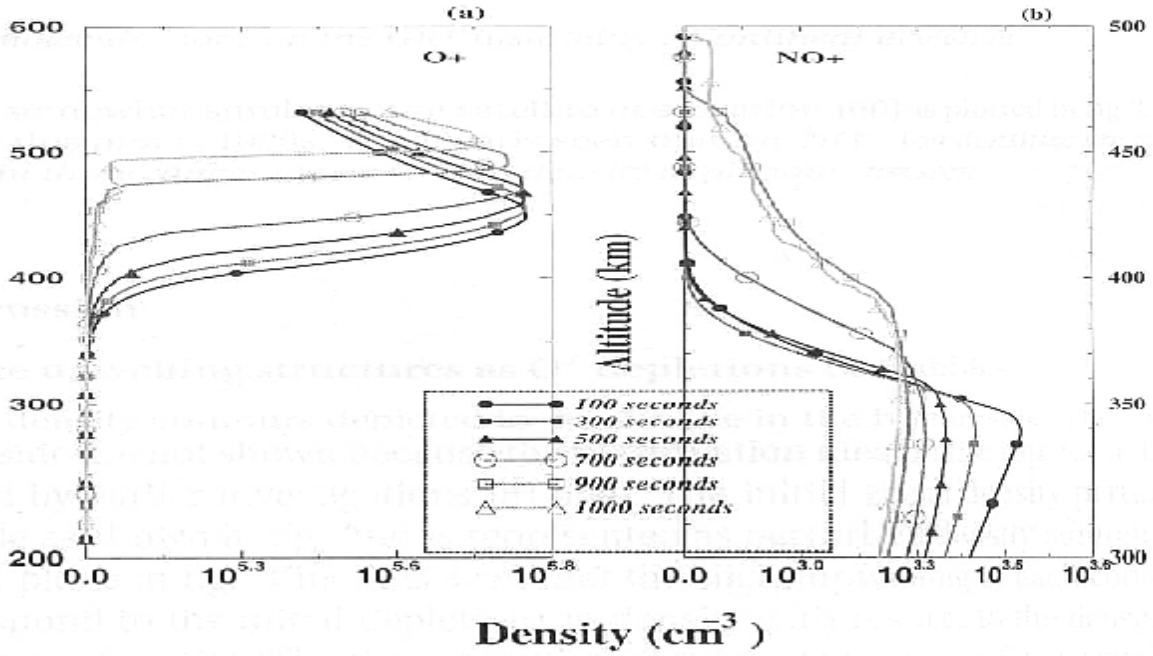

Figure 6.

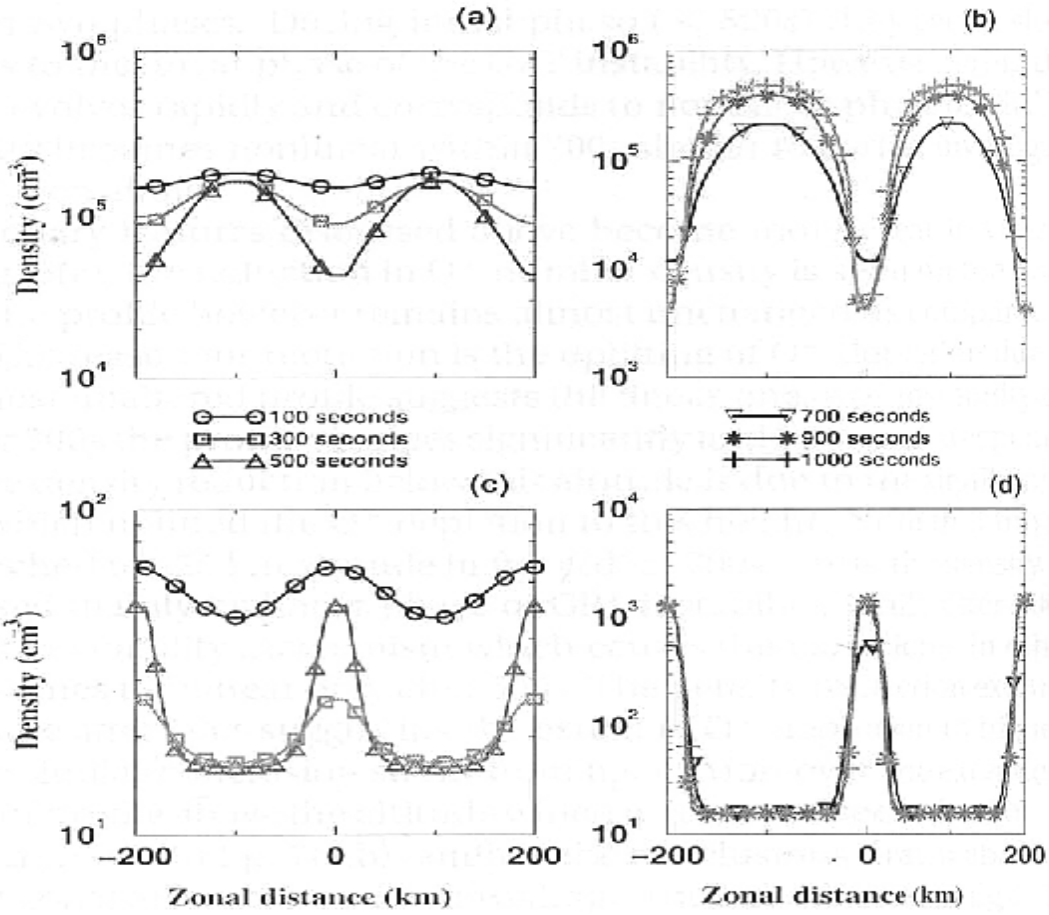

Figure 7.

tion plane somewhat similar to the satellite observation [60] is plotted in fig 8. The time chosen for this plot is 1000s. It is clearly seen that *the NO^+ ion densities are found to be enhanced in those ranges where O^+ ion density depletions are seen.*

3.3 Discussion

3.3.1 The upwelling structures as O^+ depletions or bubbles

All the O^+ density contours depicted in fig. 3(b) lie in the bottomside. The contours lie on the topside are not shown because the perturbation dies on the topside at later times as revealed by earlier investigations [81, 83]. The initial zonal density perturbation at any altitude as shown in fig. 3(a) is represented as perturbed density contours over the simulation plane in fig. 3(b). It is seen that the slight upwelling of each contour in fig. 3(b) correspond to the initial depletions in density with respect to the density value of that contour in fig. 3(a). The time evolution of these structures in fig. 4 reveals that the upwelling structures (or depleted regions) of all the bottomside contours grow to higher and higher altitude region. Since the O^+ number density increases with altitude in the bottomside, the initially depleted region of all the contours are regarded as the more depleted column (plasma bubble) in later phases of evolution. However these bubbles grow with time in two phases. During initial phase ($\leq$ 500s) they evolve slowly. This phase corresponds to the linear phase of the GRT instability. However during the later phase of evolution it evolves rapidly and corresponds to nonlinear phase of GRT instability. Thus the instability becomes nonlinear within 700s similar to earlier investigation [81, 66, 83] for single O^+ ion alone.

The evolutionary features discussed above become more clear in view of fig. 6(a) and 7(a,b). In fig. 6(a), the reduction in O^+ number density is seen on the bottomside during first 500s. The profile however remains almost unchanged as compared to initial profile in fig 1(a). The reason for reduction is the uplifting of O^+ depletion due to GRT instability. The almost unaltered profile suggests the linear phase of instability during this time. Its only after 700s the profile changes significantly and becomes steepened above 425 km altitude. The density reduction below this altitude is due to the significant growth of GRT instability which uplifted the O^- depletion to this height. Note that the upwelling structure just reached to 425 km altitude in fig. 4(d) at 700s. Thus the density variation in first 500s is caused mainly by linear phase of GRT instability, while after 500s, its nonlinear phase of GRT instability mechanism which causes the variations. In other words the instability becomes nonlinear only after 500s. The density reduction extends to higher and higher altitude after 700s suggesting the extent of O^+ depletion to higher and higher altitudes. The similar conclusion stems from fig. 4. Moreover the extended bubble causes steepening of profile above the altitude which it attains as seen after 500s. The zonal density variation shown in fig. 7(a,b) confirm the conclusions drawn above. The depletions are found at zonal distances where upwelling structure are seen in fig 4. Though the variation is taken at time 400km but the description is valid for all heights above the base. The increase in degree of depletion indicates that indeed the initial perturbation grows under the action of GRT instability.

It follows from the above discussion that the upwelling structures are seen as O+ depleted column or O+ bubble. Under the action of GRT instability mechanism, the initially perturbed O+ density evolves with time in two phases. In linear phase the depletion grow slowly while in later phase it grows rapidly to large value. These findings are similar to the nonlinear investigation of GRT instability for one ion-electron plasma [81, 64, 66, 83].

3.3.2 The upwelling structures as NO^+ enhancement

The initial downwelling of density contours lying above the base as depicted in fig. 3(c) correspond to depletion in NO^+ density as shown in fig. 3(a). The difference in initial morphology of O^+ (upwelling) and NO^+ is owing to their density gradients above the base which are positive and negative respectively. Interestingly the downwelling structure changes its morphology and becomes upwelling immediately within 100s. Since NO^+ number density decreases with altitude above the base, it implies that the initially depleted NO^+ region become enhanced region at 100s. As time progress the upwelling structures or enhanced regime move to higher altitudes and seen as more and more enhanced regime. The upwelling structures as the depleted O^+ and enhanced NO^+ is what the observation reveals [60] and reason was thought to be the GRT induced transport process [3, 63]. However, since the GRT instability induced transport becomes efficient only after 500s ,it was remained as a puzzle that what keeps the NO^+ ions to survive initially near F region peak where its life-time is 100s. We try to explain it in the next section on the basis of two distinguish features of NO^+ ions as compared to O^+ ions. The first feature is that the initially depleted NO^+ region becomes enhanced immediate after the beginning of the simulation and second is the confinement of contours of NO^+ lying above the base till 300s. We keep open the possible causes for these distinguish features also till next section.

These distinguish features become more evident in fig. 6(b) and 7(c,d) which provide some more insight towards the understanding. In fig. 6(b) the steepening of NO^+ profile is seen during first 300s above 350 km altitude. This feature is reflected as the confinement of contours in fig 5 and reduction in reference density value in fig. 7(c). As discussed in last section that the GRT instability is in linear phase during this time and any appreciable variation in profile is attributed to linear phase of instability . In case of O^+ ions it is the uplifting of O^+ depletion which causes the variation. However for NO^+ the this is not the cause for variation. If it is so then the density should increase at any altitude above 350km altitude due to the uplift of NO^+ ions by linear phase of GRT instability. But what is noticed during first 300s is opposite of it. Another process which may be important for NO^+ is the chemical process. This possibility will be explored in next section. After 300s, the profile begin to become less and less steepened with the reduction of NO^+ number density near the 350 km altitude region. It means that the NO^+ ions from lower altitude region are transported to higher altitude region significantly after 300s. Thus the transport process induced by linear GRT instability becomes dominant after 300s over the process which was more dominant during first 300s. After 500s, steepening reduces rapidly indicating the phase transition of GRT instability. The upwelling structures of NO^+ density contours seen in fig. 4 after 300s is thus due to the transportation of NO^+ from lower altitude to higher altitude. Under these circumstances the upwelling of NO^+ density contours seen during first 300s becomes interesting when the transport process

does not dominate. This aspect is discussed in next section.
The zonal density variation shown in fig 7(c,d) reveal that the enhancements are found at zonal distances throughout the phase of evolution where upwelling structures are seen in fig. 5. We expect this feature as explained in the beginning of the section. It is interesting to note that the enhancement are seen during first 300s when the neither ambient motion nor linear phase of GRT dominates. The feature is similar as to observe the upwelling structure for NO^+ ions during first 300s and will be discussed in next section. The decrease in reference density value at 400 km during 300s reflects as confinement of contours in fig. 5 or steepening of profile in fig. 6(b). The degree of enhancement also reduces for first 300s and then begins to increase. After 500s it increases rapidly corresponds to nonlinear phase of GRT. In between 300 and 500s, the increase in reference density value and degree of enhancement again indicate that the transport process, dominate over the process which was dominated during first 300s.

3.3.3 Transport process vs. chemical process

Some of the unexplained evolutionary aspects discussed in last two sections are:
(1) The upwelling structures of NO^+ contours in fig.5 or the enhancement in fig. 7(c) during initial 300s when the transport process is not dominant.
(2) The confinement of its contour in fig. 5 or steepening of its profile in fig. 6(b) or reduction in reference density value in fig. 7(c) during first 300s.
We feel that the different evolutionary aspects discussed above can be attributed to the varying importance of different processes, chemical and transport, with time and altitude. They decide the evolution of O^+ and NO^+ ion number densities according to continuity equations

$$\frac{\partial n_1}{\partial t} = -\vec{V}_{pol}.\nabla n_1 - \beta n_1$$

$$\frac{\partial n_2}{\partial t} = -\vec{V}_{pol}.\nabla n_1 + \beta n_1 - \alpha n_e n_2$$

The rate of chemical process for O^+

$$\omega_{cO} \sim \beta$$

The rate of chemical process for NO^+

$$\omega_{c_{NO}} \sim \alpha n_e$$

The rate of transport process for O^+

$$\omega_{t_O} \sim \frac{V_{pol}}{L_1}$$

The rate of transport process for NO^+

$$\omega_{t_{NO}} \sim \frac{V_{pol}}{L_2}$$

These rates vary with time and altitude. The values of scale heights, L_1 and L_2, can be

inferred from fig. 6 . In order to have knowledge of instantaneous velocity and its altitude profile, fig. 9 is plotted by using the equation:

$$\vec{V}_{pol} = \frac{\vec{E} \times \vec{B}}{B^2}$$

where $\vec{E} = -\nabla\phi$ and ϕ is the solution of eq. (3.14).
At the time of initial perturbation, the above mentioned rates have values:

at 350 km altitude:

$$\alpha \sim 10^{-7} cm^3/s, \beta \sim 5 \times 10^{-6} s^{-1}, n_e \sim 10^3, V_{pol} \sim 5m/s, L_1 = 15km, L_2 = 30km$$

thus,

$$\omega_{c_O} \sim 10^{-6}, \omega_{t_O} \sim 3 \times 10^{-4}, \omega_{c_{NO}} \sim 10^{-4}, \omega_{t_{NO}} \sim 10^{-4}\ s^{-1}$$

For O^+ ions, the transport rate is much larger than the chemical rate. Since velocity increases with time as well increases above 350 km altitude,
For O^+ the transport rate is much larger than chemical rate for all time and at all altitudes as expected on the basis of earlier investigation [81, 66, 83] for single ion case. The continuity equation for O^+ then can be approximated as:

$$\frac{\partial n_1}{\partial t} \simeq -V_{pol}\frac{n_1}{L_1}$$

Since L_1 is positive, the density is depleted more and more with time within the upwelling structure wherein velocity is upward. Moreover, since only one process is involved in the evolution of O^+ density perturbation, its feature doesn't change throughout the evolution.
For NO^+ ions, the scenario is quite different. Both the rates are of comparable magnitude at 350 km altitude during initial time. At the F_{peak} (448 km), chemical rate dominates over transport rate.

$$\omega_{c_{NO}} \sim 10^{-2},\ \omega_{t_{NO}} \sim 10^{-4}\ s^{-1}$$

Here we would like to recall the results obtained by linear analysis in section (2.3.4) that the linear growth rate is comparable to loss rate where NO^+ ions are significant i.e; near the base and it is less than loss rate where NO^+ ions are insignificant i.e; near the F_{peak}. Thus the results obtained by linear analysis are consistent with the simulation results. *Its the chemical process which decide the evolution of number density during initial time for NO^+ ions throughout the altitude except near the base.*
Since chemical process is the dissociative recombination process through which NO^+ ions are lost, more and more NO^+ ions are lost as altitude increases above the base. It causes the confinement of contours, steepening of its profile or reduction in reference density at 100s. The steepening of profile and increase in the velocity at 100s makes transport rate to be larger by factor 4 than its value at 0s near the base.

$$V_{pol} \sim 8m/s, L_2 \sim 20km \Rightarrow \omega_{t_{NO}} \sim 4 \times 10^{-4} s^{-1}$$

Thus the transport rate becomes dominant over loss rate near the base immediately after the initiation of GRT instability. Above the base situation becomes more interesting. The

inferred from fig. 6 . In order to have knowledge of instantaneous velocity and its altitude profile, fig. 9 is plotted by using the equation:

$$\vec{V}_{pol} = \frac{\vec{E} \times \vec{B}}{B^2}$$

where $\vec{E} = -\nabla\phi$ and ϕ is the solution of eq. (3.14).
At the time of initial perturbation, the above mentioned rates have values:

at 350 km altitude:

$$\alpha \sim 10^{-7} cm^3/s, \beta \sim 5 \times 10^{-6} s^{-1}, n_e \sim 10^3, V_{pol} \sim 5m/s, L_1 = 15km, L_2 = 30km$$

thus,

$$\omega_{c_O} \sim 10^{-6}, \omega_{t_O} \sim 3 \times 10^{-4}, \omega_{c_{NO}} \sim 10^{-4}, \omega_{t_{NO}} \sim 10^{-4}\ s^{-1}$$

For O^+ ions, the transport rate is much larger than the chemical rate. Since velocity increases with time as well increases above 350 km altitude,
For O^+ the transport rate is much larger than chemical rate for all time and at all altitudes as expected on the basis of earlier investigation [81, 66, 83] for single ion case. The continuity equation for O^+ then can be approximated as:

$$\frac{\partial n_1}{\partial t} \simeq -V_{pol}\frac{n_1}{L_1}$$

Since L_1 is positive, the density is depleted more and more with time within the upwelling structure wherein velocity is upward. Moreover, since only one process is involved in the evolution of O^+ density perturbation, its feature doesn't change throughout the evolution.
For NO^+ ions, the scenario is quite different. Both the rates are of comparable magnitude at 350 km altitude during initial time. At the F_{peak} (448 km), chemical rate dominates over transport rate.

$$\omega_{c_{NO}} \sim 10^{-2},\ \omega_{t_{NO}} \sim 10^{-4}\ s^{-1}$$

Here we would like to recall the results obtained by linear analysis in section (2.3.4) that the linear growth rate is comparable to loss rate where NO^+ ions are significant i.e; near the base and it is less than loss rate where NO^+ ions are insignificant i.e; near the F_{peak}. Thus the results obtained by linear analysis are consistent with the simulation results. *Its the chemical process which decide the evolution of number density during initial time for NO^+ ions throughout the altitude except near the base.*
Since chemical process is the dissociative recombination process through which NO^+ ions are lost, more and more NO^+ ions are lost as altitude increases above the base. It causes the confinement of contours, steepening of its profile or reduction in reference density at 100s. The steepening of profile and increase in the velocity at 100s makes transport rate to be larger by factor 4 than its value at 0s near the base.

$$V_{pol} \sim 8m/s, L_2 \sim 20km \Rightarrow \omega_{t_{NO}} \sim 4 \times 10^{-4} s^{-1}$$

Thus the transport rate becomes dominant over loss rate near the base immediately after the initiation of GRT instability. Above the base situation becomes more interesting. The

depletion in O^+ or in electron density continuously increases as GRT instability evolves . It reduces the NO^+ loss rate within the depletion as compared to background. However the effect is pronounced only above 380 km and after 300s where considerable depletion occur. Thus at 100s and 300s the loss rate still remain larger than the transport rate at higher altitudes in spite the increase in transport rate. It again steepens the profile during 300-500s . Moreover V_{pol} also increases with time. Both steepening and increase in V_{pol} cause the increase in transport rate during 300-500s. Meanwhile the degree of depletion at 500s increase to 50 % near 400 km causing 50% reduction in loss rate.

$$V_{pol} \sim 50m/s, L_2 \sim 10km \Rightarrow \omega_{tNO} \sim 5 \times 10^{-3} s^{-1}$$

$$\omega_{cNO} \sim 5 \times 10^{-3} s^{-1}$$

Hence both the rates become comparable even at 400km altitude at 500s. Since O^+ density at F_{peak} is not much differ from its value at 400 km we can say that the both the rates become comparable throughout the altitudes above the base. It ceases the further steepening in the NO^+ profile as evident in fig 6(b) after 300s. After 500s its the transport process which mainly decides the evolution of NO^+ density.

The continuity equation of NO^+ ion density in two time regime can be approximated as:

$$\frac{\partial n_1}{\partial t} \simeq -\alpha n_e n_2, t < 500s$$

$$\frac{\partial n_1}{\partial t} \simeq -V_{pol} \frac{n_1}{l_2}, t > 500s$$

The features listed in the beginning of the section are now explained as follows:
(1)At the zonal distances where O^+ depletions are found the NO^+ life time is larger than outside the depletions. It causes the upwelling of NO^+ density contour in fig. 5 or the enhancement in its density in fig. 7(c) during first 300s when chemical process dominates.
(2) Since NO^+ ion life time is smaller at higher altitude than at near the base, the bottomside profile becomes steepened which is also seen as confinement of density contours and reduction in reference density.
Once the transport process dominates, more and more NO^+ ions move to higher altitudes causing enhancement in its density even after 300 s.
An analysis of AE-C satellite data by Szuszczewicz [96] suggested that the chemical process alone can not explain the observation and transport processes are required to transfer the significant amount of both the ions to higher altitudes. The present investigation reveals that:

The evolution of NO^+ density is dominated by chemical process during first 300s. It causes the reduction in scale height which increases the transport rate. The increase in velocity due to the dominant O^+ positive scale height further enhances the transport rate. On the other hand, O^+ density is depleted more and more within the upwelling structure causing the increase in NO^+ ion life time or decrease in chemical rate. These effects make the transport process to rapidly overcome the chemical loss process for NO^+ ions within the depleted O^+ region. Even when the chemical process dominates, the NO^+ is enhanced in

the upwelling structures since its life-time is larger within it as compared to outside. The larger life-time makes them to available for transport process within the upwelling structure during later times.

Once the transport process dominates the NO^+ ions near the base is supplied to higher altitude. Note that the $10^3 NO^+ ions/cm^3$ from near the base at 300s are transported to 420 km at 1000s. This point is more clear from the density variation of O^+ and NO^+ ions shown in fig. 8. The O^+ depletion and NO^+ enhancement are collocated up to the topside. Moreover $6 \times 10^2 NO^+ ions/cm^3$ are reached to topside through the peak at 1000s. The density variations of both the ions are nearly similar to the satellite observation [60]. So far we are able to explain the transport of significant NO^+ ions on the topside and its enhanced morphology along with O^+ depletion on the basis of chemical loss and GRT induced transport process. However we are yet far to explain one of the rare observation [60] which reveal the NO^+ ions more than O^+ ions inside the depletion on the topside. It indicates that the NO^+ ions below the base are transported to the topside. Below the base, electron density scale height becomes very large and one expect the GRT instability to not to work there as was earlier thought [3]. In order to resolve such discrepancy, the zonal O^+ and NO^+ density variation at 340 km altitude just below the base is plotted in fig. 10(a,b). Most importantly what we see is 70% enhancement in NO^+ at 1200s just below the base. It means that instability indeed worked there. We throw more light on this aspect in subsection 3.3.5.

3.3.4 Modified polarization velocity in the presence of NO^+ ions

The increase in the polarization velocity with time is one of the reason for transport process to dominate over chemical process within few hundred seconds. Obviously it is due to the positive scale height of the O^+ ions which becomes dominant ions above the base. Its of interest to find out the analytic expression of nonlinear polarization velocity on the similar line as Ossakow and Chaturvedi [64] have done for GRT instability with O^+ ion alone. Here we make use of their velocity expression for analogy, once we obtained the linear expressions from the investigation presented in previous chapter. The polarization electric field given by eq. (2.39) of chapter 1 can be used for deriving the linear velocity of bubble by the equation:

$$V_{pol} = \frac{\delta E}{B}$$

which becomes

$$V_{pol} = \frac{(m_1 \delta n_1 + m_2 \delta n_2)}{(m_1 n_1 + m_2 n_2)} \frac{g^*}{\nu_{in}} \tag{3.17}$$

where,

$$g^* = g - \nu_{in} \frac{E_{xo}}{B}$$

E_{xo} is the westward electric field. and

$$\frac{\delta n_2}{\delta n_1} = \left(\frac{n_2}{n_1}\right) \left(\frac{L_1}{L_2}\right) \tag{3.18}$$

For given δn_1, the value for δn_2 can be calculated from above expression. Ossakow and Chaturvedi [64] have derived the linear and nonlinear bubble velocity for one ion-electron plasma:

$$V_{lin} = \frac{\delta n_e}{n_e} \frac{g^*}{\nu_{in}}$$

$$V_{non} = \frac{a(\frac{\delta n_e}{n_e})}{b + a\left[1 - \left(\frac{\delta n_e}{n_e}\right)\right]} \frac{g^*}{\nu_{in}} \tag{3.19}$$

where 'b' and 'a' are the horizontal and vertical dimensions of the bubble.
With the analogy between linear velocity expression in present case and their case, the nonlinear bubble velocity for two ions-electron plasma can be written as:

$$V_{pol} = \frac{a\left[\frac{\delta n_1 . m_1 + \delta n_2 . m_2}{n_1 . m_1 + n_2 . m_2}\right]}{b + a\left[1 - \left(\frac{\delta n_1 . m_1 + \delta n_2 . m_2}{n_1 . m_1 - n_2 . m_2}\right)\right]} \frac{g^*}{\nu_{in}} \tag{3.20}$$

$$V_{pol} = \frac{a(\frac{\delta n_1}{n_1})\left(\frac{1+\frac{\delta n_2 m_2}{\delta n_1 m_1}}{1+\frac{n_2 m_2}{n_1 m_1}}\right)}{b + a\left[1 - \left(\frac{\delta n_1}{n_1}\frac{1+\frac{\delta n_2 m_2}{\delta n_1 m_1}}{1+\frac{n_2 m_2}{n_1 m_1}}\right)\right]} \frac{g^*}{\nu_{in}} \tag{3.21}$$

We now compare the instantaneous altitude profile of velocity obtained from this expression with the fig. 9, which is obtained by numerical simulation. The ratio $\frac{\delta n_2}{\delta n_1}$ given by (3.18) is function of the density and scale height ratios and both depends on altitude and time. Thus the instantaneous altitude variation of ratio $\frac{\delta n_2}{\delta n_1}$ can be evaluated for instantaneous altitude variation of both the ratios. For assumed value of ratio b:a, the instantaneous altitude variation of V_{pol} can then be obtained.
In fig. 11(a,b), the plot is shown for times 500 and 700 seconds respectively. In the plot, the fractional depletion of O^+, i.e., $\frac{\delta n_1}{n_1}$ is chosen as free parameter similar to Ossakow and Chaturvedi [64]. Its values are also shown on the plot. The altitude variation of scale height ratio at these two times are calculated from fig. 6 (a-b). The instantaneous altitude variation of both the densities are assumed of the form:

$$n_i(z,t) = n_i(z_0,t) \exp\left[\frac{(z-z_0)}{L_i(z,t)}\right]$$

The form roughly fits the density variations plotted in fig. 6(a-b). Since the upwelling structure becomes more and more vertically elongated with time as evident from fig. 4 and 5, the b:a ratio is taken lesser at 700s than at 500s.

The comparison of fig. 9 and fig 11 reveal that:
(1) The instantaneous altitude variation of analytically calculated velocity is qualitatively similar to the numerical profile.
(2) The analytical profile corresponding to 50 % degree of depletion at 500s quantitatively similar to the numerical profile at that time.
(3) Similarly the analytical profile corresponding to 80 % degree of depletion at 700s shows the similarity with numerical profile at similar time.

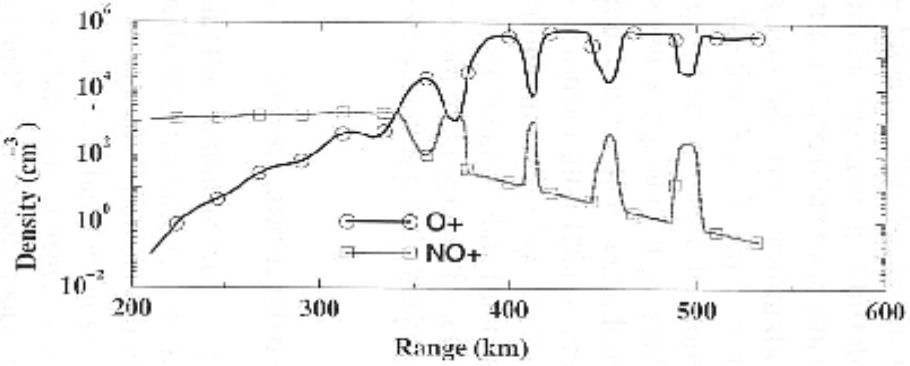

Figure 8.

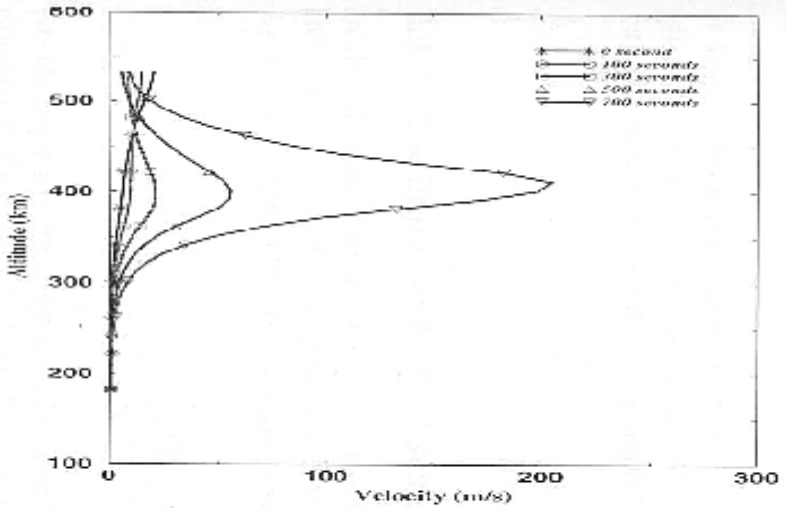

Figure 9.

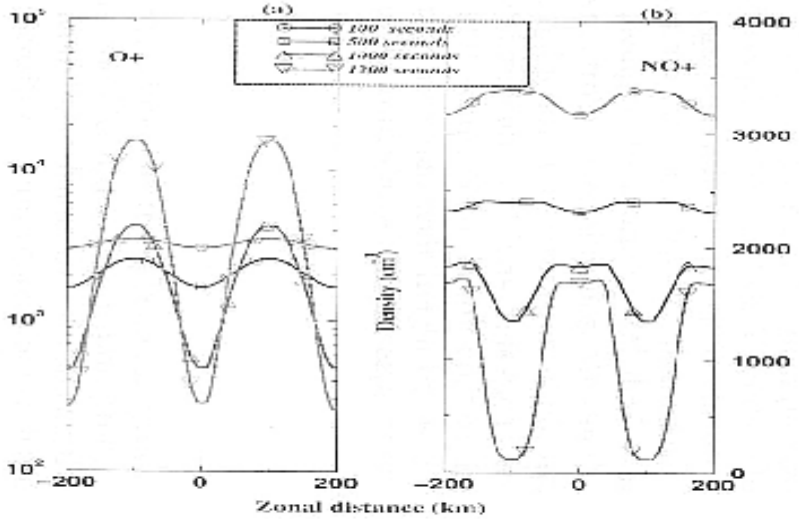

Figure 10.

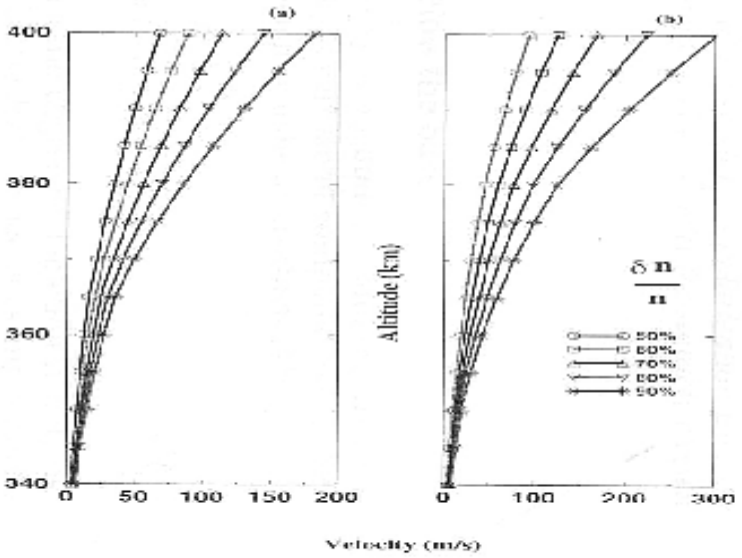

Figure 11.

It is to be noted that the numerically obtained degree of depletion at these two times are in fact 50 % and 80 % as evident from fig. 7(a,b).

It implies from the above findings that the analytical expression for polarization velocity given by (3.21) can be approximated as the nonlinear bubble velocity for suitably chosen value of axis ratio and degree of depletion.

3.3.5 The importance of O^+ scale height below the base

In the altitude region just below the base, where $n_2 \sim n_1$ both δn_1 and δn_2 are positive since L_1 and L_2 are positive. However the δn_2 is very small compared to δn_1 since $L_2 >> L_1$. Thus in this region, the polarization velocity can be approximated by:

$$V_{pol} = a(\frac{\delta n_1}{n_1}) \frac{\left(1 + \frac{n_2 m_2}{n_1 m_1}\right)^{-1}}{b + a\left[1 - \frac{\delta n_1}{n_1}(1 + \frac{n_2 m_2}{n_1 m_1})^{-1}\right]} \tag{3.22}$$

which depends on degree of O^+ depletion. Since the degree of depletion mainly depend on scale height [65], the O^+ scale height just below the base becomes important for transportation of plasma to the higher altitude. In addition it was shown by Anderson and Rusch [3] that the transport process is dominant for NO^+ ions in this region. Thus considerable amount of NO^+ are always available for transport process induced by GRT mechanism. The density fluctuations shown in fig. 10, on the other hand, indicate the considerable growth of instability below the base. Such growth is due to the non-local nature of instability which increases with wavelength of perturbation [112, 53] and could make instability to grow in the region where even negative gradients exist [86]. However we see that such growth becomes considerable only after 1000 seconds. By this time very large O^+ scale height develops on the bottomside owing to the motion of O^+ depletion as seen in fig. 6(a). It prevents the motion of plasma from lower altitudes. We ran the simulation for 1800 seconds and indeed found the reduction in the transport of plasma to the topside after 1200 seconds. In order to supply significant NO^+ ions, thus such fluctuations must develop before the drastic change in O^+ scale height. In this context the O^+ scale height below the base becomes important. The small scale height below the base can make growth faster below the base as implied from above velocity expression. We explore this possibility below under case 4.

3.3.6 Investigations with other cases

So far the nonlinear evolution of GRT instability for two ions-electron plasma is investigated under the case 1. The investigation reveals that the GRT induced transport process causes the advection of both the ions to the topside from bottomside. On the topside, the NO^+ density enhancements are collocated with O^+ density depletion consistent with the observation [60]. However in one of their ion-composition measurement inside the bubble, the O^+ ion density as low as $10^3/cm^3$ and NO^+ ion density as much as $10^3/cm^3$ were

found on the topside. In fig. 13 (a), the zonal density variations of both the ions at 460 km altitude are plotted. The O^+ ions as low as $10^4\ /cm^3$ and NO^+ ions as much as 6 $\times\ 10^2\ /cm^3$ are seen on the topside. These findings are far too close to the observation. Such rare observation indicate that the both the ions must be transported from below the base. The fluctuation shown in fig. 10 (a,b) shows the fringe field effect [112] and if one increase the wavelength of perturbation, efficient transport of theses ions from much lower altitudes can be achieved. Moreover, we discussed the direct impact of O^+ scale height below the base on the V_{pol} in last section which deserve further investigation here. Thus in order to have close agreement, quantitatively, with the observation, one need to take proper background conditions such as density profiles and perturbation parameters mainly the wavelength. We now investigate the GRT instability by varying these parameters as listed in section 3.1.7. The isodensity contours shown in fig. 12 (a,e) for case 2 has feature of enhanced upwelling of isodensity contours of both the ions compared to case 1. The simulation time is chosen to be 900s which is the time of maximum upwelling for case 2. In fig. 13(b), the density variations along zonal direction at 460 km altitude are depicted for both the ions. The comparison with fig. 13 (a) reveal that the degree of depletion (enhancement) in O^+ (NO^+) densities are increased for case 2 compared to case 1. The NO^+ ions as much as $10^3/cm^{-3}$ are found in the topside which was not seen for case 1. This feature, particularly, is consistent with the satellite observation [60]. It is to be noted that the NO^+ scale height for both the cases is kept unchanged while the O^+ scale height is made 5 km for case 2. Moreover base of the F region is shifted to higher altitude to maintain the same F_{peak} altitude as for case I. We feel that similar to the study [65] for single ion case, for double ion case both reduction in scale gradient and higher altitude shift of base could cause the degree of depletion and enhancement to be more for case 2 as compared to case 1.

The isodensity contours of NO^+ and O^+ corresponding to case 3 are shown in fig. 12(b,f) while the density variations along zonal direction are shown in fig. 13(c). The enhanced upwelling compared to case 1 and 2 are seen. Note that the initial O^+ and NO^+ density profiles are same as in case I but wavelength of perturbation is 600 km instead of 200 km. The numerical investigation by Zalesak and Ossakow [112] for single O^+ ion reveal that the longer wavelength causes the large depletion due to supply of O^+ ions from much lower altitude compared to shorter wavelength. We see that $6 \times 10^3 O^+ ions/cm^3$ are seen up to 460km causing large depletion in O^+ (fig. 13(c)). The O^+ ions with density of order of 10^3 was never seen at the peak altitude region for case 1 and case 2.

It was discussed in section 3.3.5 that the O^+ scale height below the base play an important role owing to the large scale height of NO^+ ions. This possibility is explored in case 4 where O^+ scale height below and above the base are chosen as +7 and +5 km respectively. The isodensity contours and density variations are shown in fig. 12(c,g) and 13(d) respectively. Interestingly, the finding of case 4 is very similar to case 3. More O^+ ions from just below the base are transported to much higher altitude compared to case 2. The $6 \times 10^3 O^+ ions/cm^3$ are seen beyond 460 km which was never seen for case with shorter wavelength. The comparison of case 3 and case 4 implies that

the shorter wave perturbation with small scale height below and above the base can give results similar to long wave perturbation with large scale heights. The situation may arise where suitable combination of these parameters could give rise the results similar to that of the rare observation [60]. The variabilities in the occurrence of NO^+ ions inside the depletions [60, 63] can now be attributed to the varying background conditions such as density profiles and seeding perturbation mainly the wavelength.

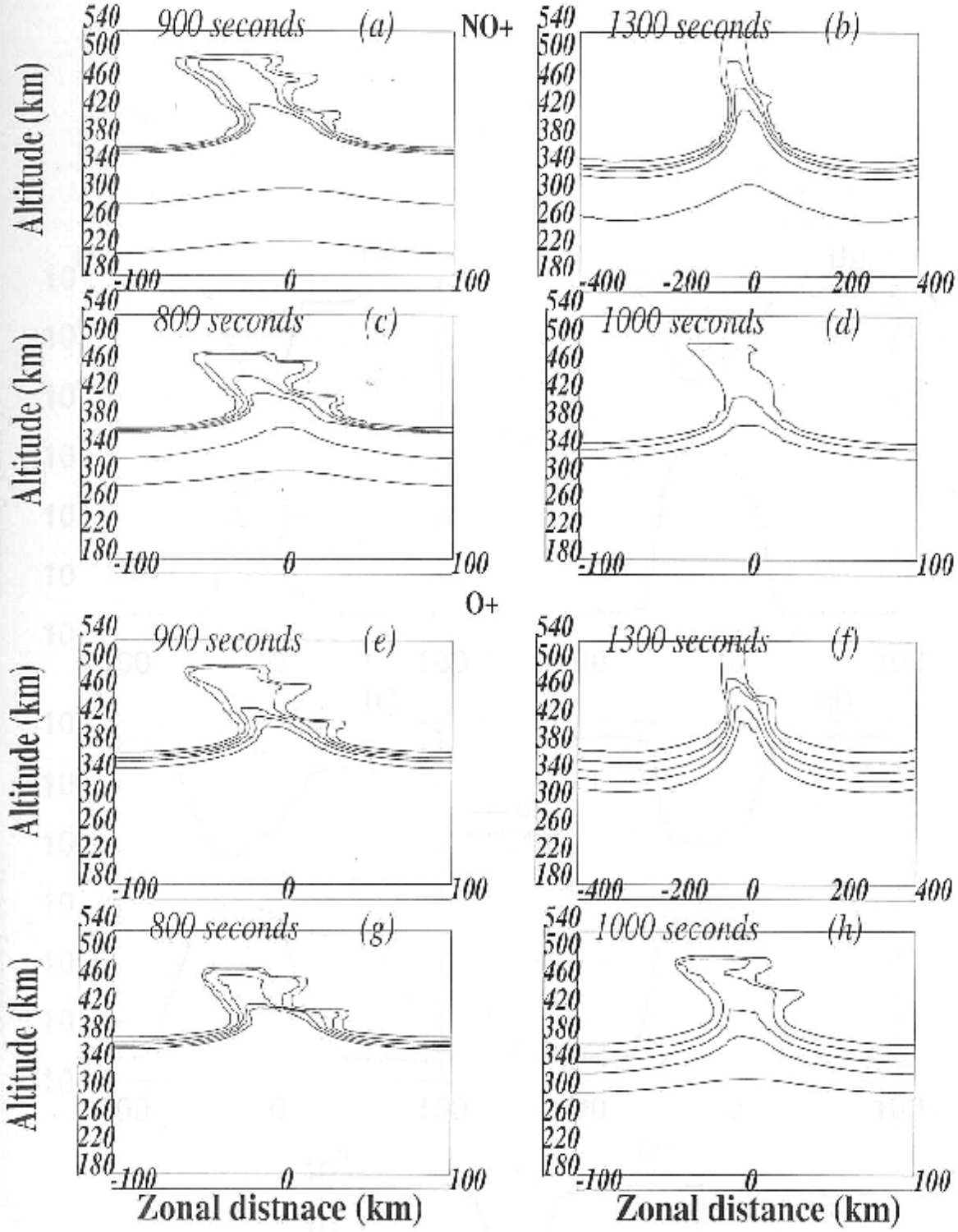

The top two panels correspond to NO^+ ions with similar choice of contours as in fig. 5.
The bottom two panels correspond to O^+ ions with similar choice of contours as in fig. 4.

Figure 12.

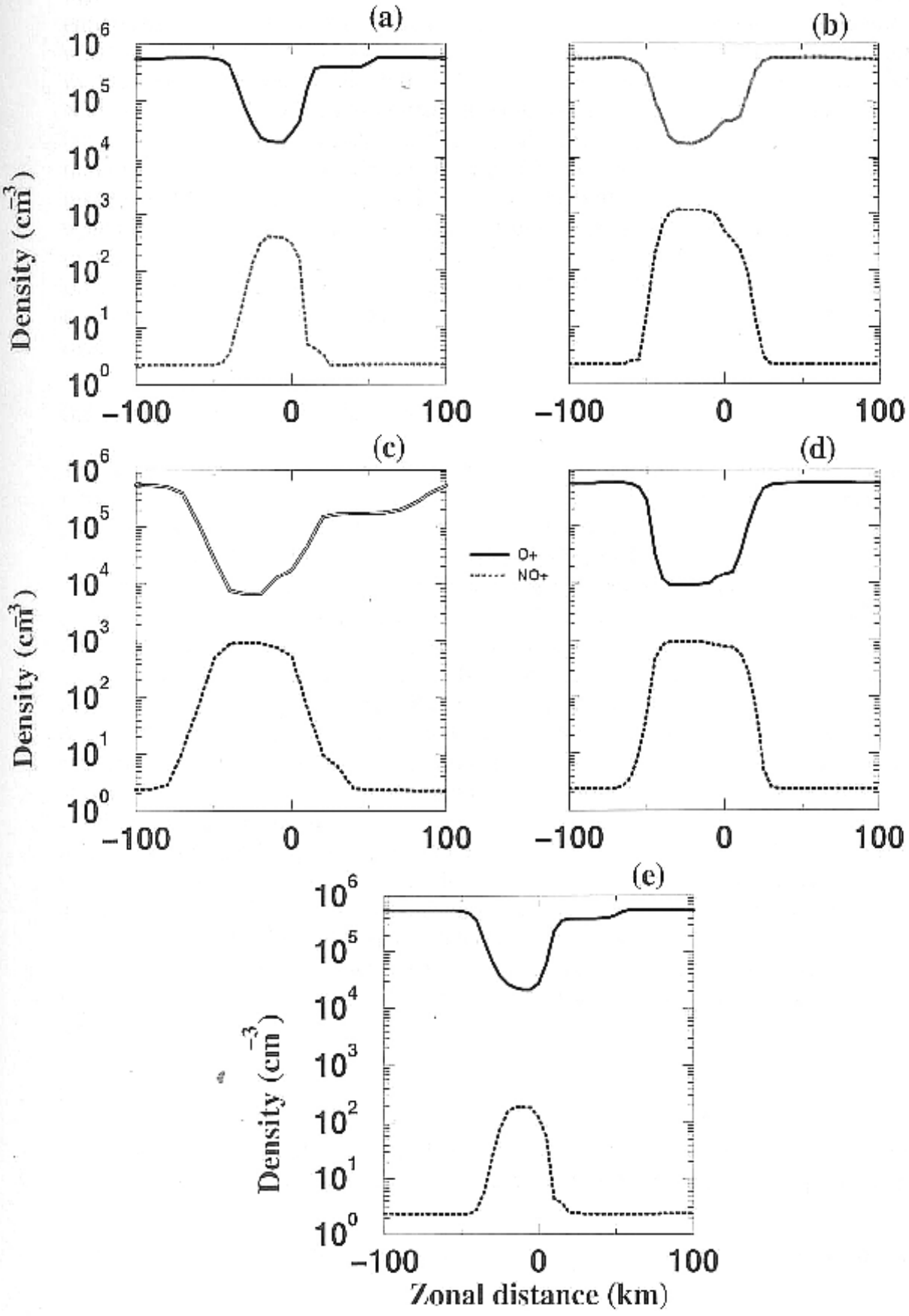

Figure 13.

It was shown by Anderson and Rusch [3] that the prereversal enhancement of the electric field is responsible for supplying the sufficient NO^+ ions up to the base. In all our investigation so far we have taken 50-50% O^+ and NO^+ ions at the base due to the prereversal enhancement. Under case 5 we have studied the situation where relative concentration of O^+ and NO^+ ions is 85-15% at the base. The isodensity contours and zonal density variations at 1000s are plotted in fig. 12(d,h) and 13(e) respectively. The modulations of NO^+ ion density contours are reduced as compared to case 1 while modulations of O^+ ion density contours are unaltered. The zonal density variations also shows the reduction in degree of NO^+ enhancement as compared to case 1. The reason in the reduction in degree of NO^+ enhancement is due to the availability of these ions on the bottomside which is highly reduced for case 5 as seen from initial density profile. Thus *availability of NO^+ ions near the base is also crucial for supplying significant NO^+ ions to the topside.* The availability of NO^+ ions highly depend on the ambient vertical drift [3]. Since its nature varies from day-to-day, the finding of NO^+ ions on the topside also varies as reported [60, 63].

3.4 Summary and conclusion

The investigation of GRT instability in the presence of molecular ions is dealt with different background conditions like different seeding perturbations and varying density profiles. The results of the investigations are as follows:

1. Both O^+ and NO^+ ions from lower heights where NO^+ life time is short, are transported to higher altitude owing to the steep density gradient present in O^+ ions.
2. The depletion in O^+ and enhancement in NO^+ ions are collocated throughout the altitude above the base. The findings has close similarity with the satellite observation [60]. The enhancement in NO^+ is attributed to chemical effects during initial phase of evolution while attributed to transport process during later phase of evolution.
3. The efficiency of transportation depends on density gradients of both the ions, seeding perturbation of wavelength and the nature of background electric field. Their day-to-day variabilities can be attributed to the day-to-day variabilities in occurrence of NO^+ on the topside as observed [60, 63].
3. The longer wavelength can efficiently supply the plasma compared to shorter wavelength from below the base where scale height of dominant NO^+ ions are large.
4. The shorter wavelength of perturbation also can supply enough plasma from below the base in the presence of steep O^+ density gradient below the base.
5. The prereversal enhancement in electric field play a crucial role for supplying the sufficient NO^+ ions up to the base which are then transported to higher altitude by GRT instability.

3.5 Figure captions

- Fig. 1: The density profiles of both the ions in (a), altitude profile of ν_{in} in (b), altitude profile of β in (c) and temporal variation of ambient vertical plasma drift in (d).
- Fig. 2: The density profile of both the ions for case 2 in (a), case 4 in (b) and case 5 in (c).

- Fig. 3: The initial density perturbations at any altitude for both the ions in 3(a) and over the simulation plane in the form of contours in 3(b,c).
- Fig. 4: The time evolution of O^+ isodensity contours.
- Fig. 5: The time evolution of NO^+ isodensity contours.
- Fig. 6: The temporal evolution of density variations of O^+ in 6(a) and NO^+ in 6(b) within the upwelling structures.
- Fig. 7: The temporal evolution of zonal density variations at 400 km altitude for O^+ ions in 7(a,b) and for NO^+ ions in 7(c,d).
- Fig 8: The density variations of both the ions at 1000s along the assumed path.
- Fig. 9: The temporal evolution of velocity profile within the upwelling structures.
- Fig. 10: The temporal evolution of zonal density variations of O^+ ions in 10(a) and NO^+ ions in 10(b) at 340 km altitude.
- Fig. 11: The analytical profile of polarization velocity for different degree of depletions at 500s in 11(a) and 700s in 11(b).
- Fig. 12: The isodensity contours of NO^+ and O^+ ions for case 2 in 12(a,e), for case 3 in 12(b,f), for case 4 in 12(c,g) and for case 5 in 12(d,h).
- Fig. 13: The zonal density variation of both the ions at 460 km altitude for case 1 in 13(a), for case 2 in 13(b), for case 3 in 13(c), for case 4 in 13(d) and for case 5 in 13(e).

Chapter 4

The radar observations of 2.8m scale size irregularities associated with ESF

4.1 Introduction

The ESF phenomenon covers a wide spectrum of scale sizes ranging from few hundreds of kilometers to few centimeters and exhibits a wide range of dynamical behavior as observed through radars [109, 100, 68], optical imagers [105, 93] and in-situ probes [27, 51]. An interesting feature of ESF irregularities which has been recorded using these techniques is the formation of large scale plasma depletions which are commonly referred as plasma bubbles. These bubbles manifest themselves on VHF and UHF radars as vertically rising plume structures. Simultaneous in-situ and radar measurements revealed that the "plumes" as seen by the radars are collocated with the wall of plasma bubbles (depletions) [75, 98, 103] . These plasma bubbles are, numerically simulated [81, 66, 71] by nonlinear evolution of GRT instability.
Dynamically both the ESF irregularities and plasma bubbles exhibit large variabilities. The radar observations, in particular, reveal that the occurrence and morphology of ESF is highly variable on day-to-day basis [109, 100]. The Doppler velocities of ESF structures observed by radar are also variable in nature. The velocities inside the bubbles were found to be upward ranging from few tens of ms^{-1} [60, 100] to an occasional kilometer per second [1]. On occasions, plumes are observed with downward motion larger than the ambient [69].
In order to understand the nature of ESF, we have conducted the observational campaigns during equinoctial period (March-April, 1998-99) using the VHF radar situated at Gadanki (13.5°N, 79.2°E, dip 12.5°). The results obtained by the observations are discussed in this chapter. In first section we discuss the principle of the radar and briefly describe the radar system used for observation. It further enlists the nights on which observations were conducted. The general features of ESF observations are described in the next section. In section 3, we have selected some of the interesting events for detailed discussion. In particular, it deals with the morphology and velocity features and provides further insight to the ESF phenomenon.

4.2 Principle of radar and System Description

4.2.1 Principle of radar

The useful tool for exploring the ionosphere is the scatter radar which works on the principle of the backscattering from the refractive index fluctuations present in the ionosphere. It receives the scattered wave $\vec{k}_s$ according to the law of conservation when trans-

Table 1: Radar parameters used for the spread F experiments

Specifications	VHF (Gadanki)
Location	$13.5^o N$, $79.2^o E$
Magnetic dip	$12.5^o N$
Frequency	53 MHz
Peak Power-Aperture product	3×10^{10} Wm^2
Beam width (3dB)	3^0
Beam direction	14.8^o to due north
Inter-pulse period	4 ms
Pulse width	32 μs
No. of coherent integrations	1
No. of FFT points	256
No. of incoherent integrations	8
Range coverage	84 - 588 km
Range resolution	4.8 km
Velocity range	± 354 ms^{-1}
Velocity resolution	2.76 ms^{-1}

mitted wave, $\vec{k}_t$ is scattered from the fluctuations $\vec{k}_m$ present in medium:

$$\vec{k}_t = \vec{k}_m + \vec{k}_s \tag{4.1}$$

The radar mainly detects the backscattered echos owing to their large amplitudes, i.e., $\vec{k}_s = -\vec{k}_t$. Above condition then implies that the fluctuation components whose planes of constant phase are $\perp$ to k_t and wavelength is just half of the transmitted wave would be received by the radar. Radar would thus provide the information of one particular spatial Fourier component of the fluctuation.
The radar power spectra is rich in information of the signal strength, mean Doppler shift and Doppler spectral width. If the fluctuations are thermal in nature (incoherent scatter radar), the spectra provide the total electron content in the irradiated volume, bulk motion of the ionosphere [18] and the temperature [9]. However if the fluctuations are associated with some plasma instabilities (coherent scatter radar) , the quantities inferred are the strength of irregularities inside the irradiated volume, the line of sight velocities of irregularities and the dispersion in the velocities [107]. The irradiated volume is determined by the antenna beam-width, the transmitted pulse width and the vertical extent of echoing region under consideration.
The ESF irregularities are found to be field aligned [99] i.e they are of high aspect sensitive in nature. Since $k_m \parallel k_t$ for back scattering, the radar line of sight has to be pretty close to the direction transverse to $\vec{B}$ for backscattering by the ESF irregularities.

4.2.2 system Description

The Indian Mesosphere-Stratosphere-Troposphere (MST) radar situated at Gadanki was operated at 53 MHz frequency to detects the 2.8 meter scale size irregularities. For the observations presented here, the radar beam was oriented at 14.8° magnetic north corresponding to the direction transverse to the magnetic field at about 330 km. For the radar half power beam width of 3° the condition for the perpedicularity to the magnetic field is satisfied over the height range of 150-550 km. Some of the important specifications of this radar are presented in Table 1.
Before describing the system, we would like to emphasize some aspects regarding radar specifications. The radar measures the backscattered power, the Doppler spectra and width of the spread F echoes. Spectral observations can be difficult since the radar target is often overspreaded both in altitudes and frequencies. The frequency here is the maximum Doppler shift plus the expected spectral width. The maximum velocity of 3m irregularities are found to be 1-2 km/s [1] so that the correlation time for this irregularities are 2-3 ms or the maximum Doppler shift is 500 Hz. Moreover both upward and downward motions can occur simultaneously which extended this range to 1000 Hz. The Nyquist frequency for these fluctuations is then 500 Hz. In order to satisfy the Nyquist sampling theorem, the sampling rate (reciprocal of IPP) must be of the same order as the Nyquist frequency. In other words the IPP must be within 2-3 ms range to avoid the frequency ambiguity. At the same time since the irregularities are spreaded as high as 1200 km one need to have IPP as large as 8ms [42] to cover it and to avoid the range ambiguity. In present observation we have chosen the IPP as 4 ms which unambiguously measure ± 125 Hz Doppler shift and covers the altitude up to 600 km. The choice of IPP more than 4 ms gives larger Doppler and altitude range but for the low altitude station like Gadanki, maintaining the radar beam direction $\perp$ to B becomes difficult beyond 600 km. The pa-

rameter which directly alters IPP or sampling rate is the coherent integration. It acts as a signal filtering by reducing the sampling rate for fluctuations having longer correlation time than the IPP [107]. In present observation we don't encounter such requirements and so no. of coherent integration is kept one.

The MST radar is a high power coherent pulsed radar operating at 53 MHz whose peak power aperture product can go up to $3 \times 10^{10} W m^2$. The system comprises of (1) a phased antenna array consisting of two orthogonal sets of 1024 three element Yagi antennae arranged in a 32×32 matrix over an area of $130 \times 130 m^2$. (2) 32 high power transmitters with peak power ranging from 20 to 120 KW, adding to a total of 2.5 MW (3) 32 units of transmit-receiver duplexers realized by means of hybrid couplers and pin diodes and (4) a phase coherent receiver with quadrature channels having a band width of 1.7 MHz with a gain of 120 dB. A detailed description of the various subsystems [73] and the observation of equatorial spread F using this radar for the first time [68, 69] were reported earlier.

4.2.3 Data processing

The data are collected in the form of complex time series and subjected to the the process of FFT for on-line computation of the Doppler power spectrum for each range bin (no. of range bins = range coverage/range resolution) of the selected range coverage. A minimum number (here 8) of spectral averaging, incoherent integration, are performed online and stored in magnetic tape for off-line processing. The incoherent integration reduces the unwanted fluctuations significantly and improve the signal detectability. The data are further edited to remove the interference, if any, which might run through the entire range window and is subtracted out by estimating it in a range bin where it dominates over the real signal. The spectral parameters viz., total signal power, weighted mean Doppler velocity and velocity variance are obtained from the three lower order moments of the spectrum. The spectrum contains noise as background and it needs to be removed as a first step to compute the moments. The average noise value for each range bin is estimated following the objective method of Hildebrand and Sekhon [31]. The median noise level is calculated and subtracted from all the range bins of the spectral frame. The next step is to detect the signal and to determine the spectral window. For this, the Doppler bin having the peak power is identified and a seven-point template is run across on either side to find the window limits where the running average falls to 3 dB above the noise level. Once the signal window is fixed, the spectral moments are computed through numerical integration using the expressions give by [107]. The three lower order moments are expressed as follows:

$$M_o = \sum_{i=m}^{n} P_i$$

$$M_1 = \left(\frac{1}{M_o}\right) \sum_{i=m}^{n} P_i f_i$$

$$M_2 = \left(\frac{1}{M_o}\right) \sum_{i=m}^{n} P_i (f_i - M_1)^2$$

where m and n are the lower and upper limit of the Doppler bin of the spectral window.

Table 1: The list of cases chosen for investigation.

	a_1	λ_1 (km)	a_2	λ_2 (km)	$\psi_1 - \psi_2$	Exo/B	Results [Figure no.]
Case 1	0.5%	150	0.0%	600	~	Case I	Periodic depletions and enhancements moving upward and downward. [fig. 2(a,b)].
Case 2	0.0%	150	5.0%	600	~	Case I	Periodic depletion and enhancement moving upward and downward [fig. 2(c,d)].
Case 3	0.5%	150	5.0%	600	0	Case I	AMBB associated with longer wave while depletions associated with short wave . Depletions (50%) during ascending and descending phase of AMBB move downward. much larger than ambient. [fig. 2(e,f)]
Case 4	5.0%	150	0.5%	600	0	Case I	No prominant AMBB. All depletions move upward [fig. 2g].
Case 5	0.5%	150	5.0%	600	0	Case II	Depletions during ascending and descending phase move downward larger than case 3. [fig. 2h]
Case 6	0.5%	150	5.0%	600	90	Case I	Morphology is different from case 3 though AMBB are similar. Degree of depletions and downward velocities considerably differ from case 3. [fig 2i].
Case 7	1.0%	150	5.0%	600	90	Case I	Degree of depletions of downward moving depletions and velocities are larger than case 6. [fig. 2j]
Case 8	0.5%	150	6.0 %	600	90	Case I	Degree of depletions of downward moving depletions are lesser and downward velocities are greater than as in case 6. [fig. 2k]
Case 9	0.5%	300	5.0%	1200	180	Case I	No development of bubbles. [fig. 2l]

P_i and f_i are the powers and frequencies corresponding to the Doppler bins within the spectral window. The zeroth moment, M_o, is just the intensity of fluctuation at any range bin. The signal-to-noise ratio (SNR) in dB is calculated as:

$$SNR = 10log\left[\frac{M_o}{N.L}\right]$$

where N and L are the total number of Doppler bins and mean noise level respectively. The Doppler velocity of the fluctuation can be calculated from the first moment, M_1,:

$$V_D = \lambda_m \times M_1$$

where λ_m is the wavelength of fluctuation and for backscattered echo, and equals to half of the probing wavelength. Doppler width which is taken to be the full width of the Doppler spectrum in our presentation is calculated as :

$$Doppler\ width = 2(M_2)^{1/2}$$

We conducted the observations for 50 nights during equinoctial period (march-april, 98-99) with specification parameters discussed in section (4.2.2). Out of 50 nights observations, we could get the ESF events on 30 nights. In table 2, the salient features of 30 nights observations are enlisted.
The irregularity strength and associated Doppler velocities observed from radar are usually plotted as Range-Time-Intensity (RTI) and Range-Time-Velocity (RTV) maps [109, 100, 42, 68] respectively. We adopt the same method of illustration wherein the x and y axis correspond to time and altitude axes. The intensity are plotted in grey scale while the velocities are plotted by line vectors (positive upward). Since the radar acts as a slit camera [109], the times axis in the plots in fact contain information of the temporal as well as spatial evolution of ESF structures which are moving zonally through the radar line of sight. The spatial features can be inferred by simply multiplying the time to the zonal velocity [45].

4.3 General features

The varieties of ESF features are seen during the observations. Some of the features observed earlier [109, 100] are consistently encountered while few rarely observed features are also seen. In next few sections we discuss these aspects on the light of relevant ESF events.

4.3.1 Morphology of ESF

In fig. 1, the RTI maps on six nights are presented. The morphology of ESF is very similar to the morphology observed over Kwajalein [42]. The bottomside backscattered (BB) structure and plume structures having clear association with BB are commonly observed. However, on nights 18 march 98, 19 april 98,23 march 99, 13 april 99 , the altitude modulations of bottomside backscattering (AMBB) are quite prominent compared to the nights 25 march and 30 march 98. If one assumes the ambient zonal drift equals to 100 m/s, then the wavelengths of these modulations will be in 400-600 km range. In fig. 2, the h'F variation over time i.e, altitude modulation of bottomside F (AMBF) layer, are

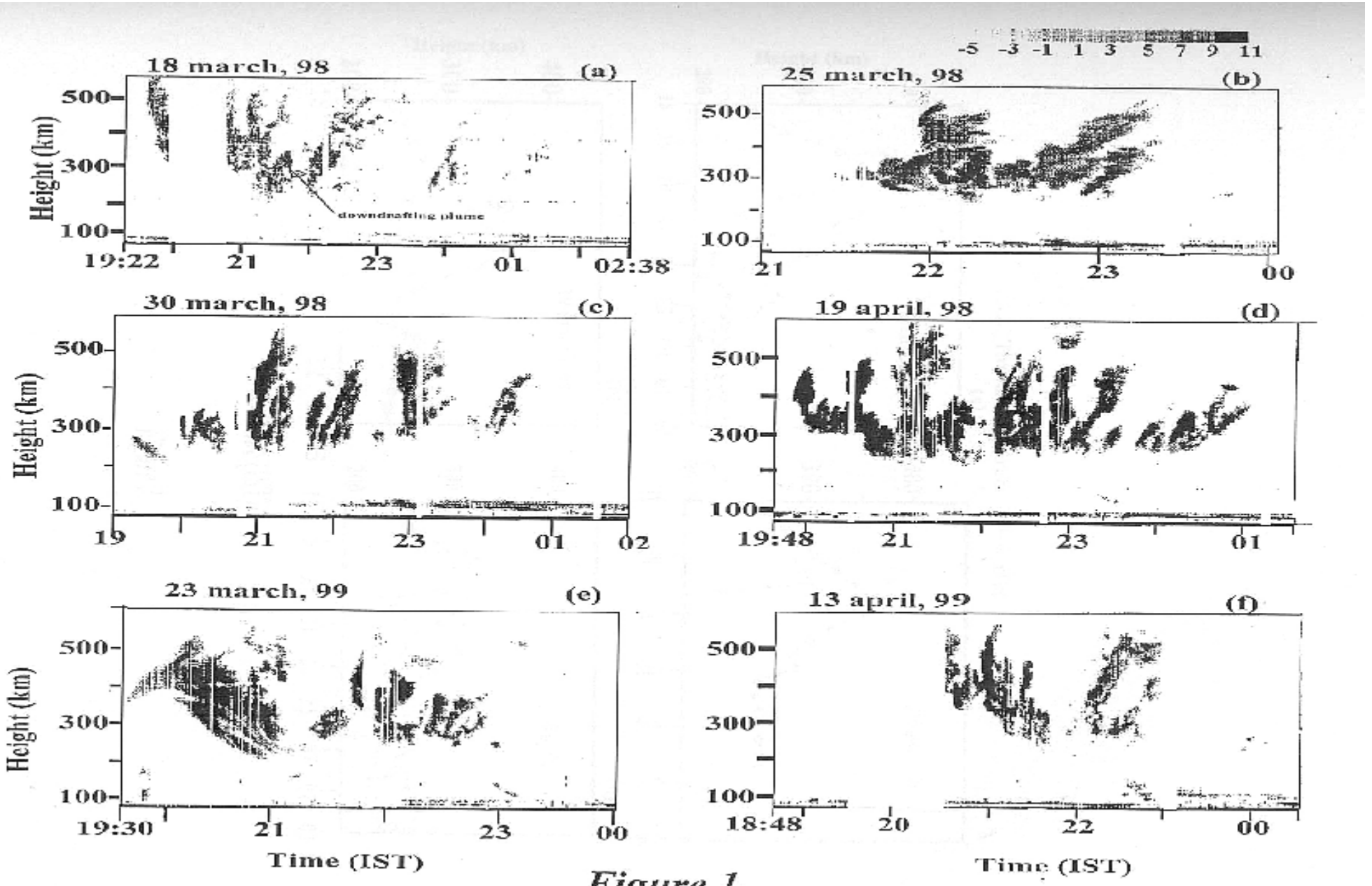

Figure 1.

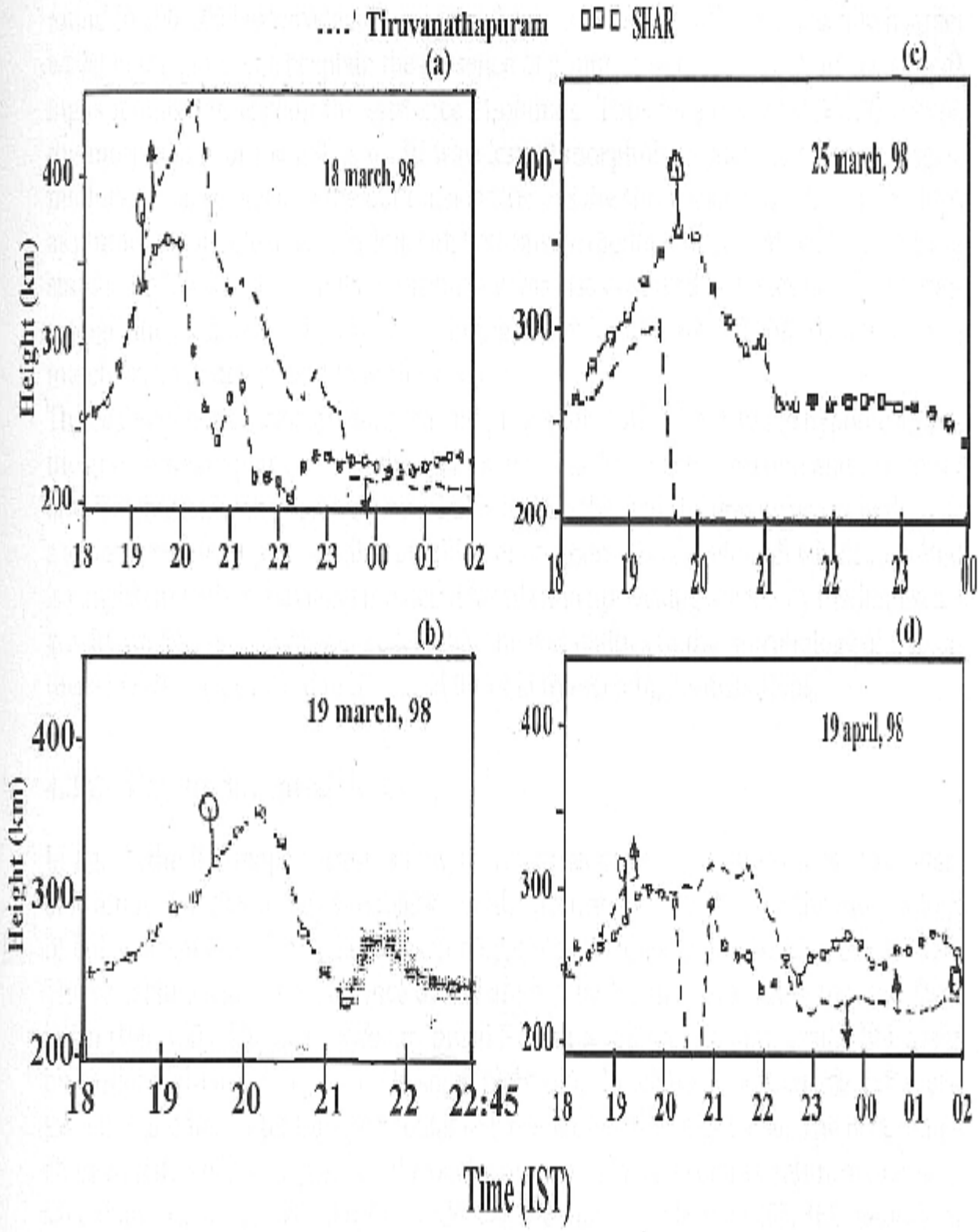

Figure 2.

shown for 18 march, 25 march 98 and 19 april 98. Interestingly the AMBB on all these nights closely follow the corresponding AMBF. Hence *the AMBB could be used as a tracer for bottomside F layer height variation during spread F.* Moreover the AMBF doesn't follow the usual pattern caused solely by ambient zonal electric field on nights when prominent AMBB are seen. The large scale zonal seeding of gravity waves along with the temporal modulation of bottomside F (BF) layer caused by ambient zonal electric field could be responsible for AMBF [48] and so for AMBB on these nights. The plume separations are found in 100-200 km wavelength range and certainly the AMBB, which has much larger wavelength, alone can't explain the presence of plume structures. The short wave seeding is required to explain the existence of plumes. Thus for prominent AMBB events, the morphology of the ESF is **multi wavelength morphology** such that the large scale modulation develops into the bottomside whereas the short scale modulation develops as plumes having clear association with bottomside modulation as verified by numerical simulation [34, 91]. The similar morphology was also observed by Kelley et al [48]. Interestingly the plumes are also observed during descending phase of AMBB structure on 18 march 98, 23 march 99 and 13 april 99.

The scales of bottomside modulation and plume separation leads to the hypothesis that the gravity waves play a role in the seeding process. The wide spectrum and the power law distribution with negative power index associated with the gravity waves make it as a suitable candidates for seeding of ESF phenomenon. The wavelength which we found is consistent with the spacing predicted for plasma up-welling seeded by medium scale gravity waves [48]. Moreover we feel that the variabilities in the morphology of ESF on these nights can be linked to the variabilities in the seeding perturbations.

4.3.2 Day-to-day variabilities

In fig. 3, the RTI maps corresponding to six consecutive nights are shown. Considerable amount of day-to-day variabilities on the occurrence as well as on the morphology of ESF is observed. The variabilities in morphology is already discussed in last section. The variabilities in the occurrence of ESF are regular features over Jicamarca and Kwajalein [109, 100]. The night without spread F event is followed by spectacular ESF event on earlier night and vice versa. On some night (not shown here) bottomside ESF is observed immediate after the spectacular ESF event on earlier night also. The occurrence characteristics of ESF depend on the background parameters such as nature of prereversal enhancement [19, 88], neutral winds [72], seeding perturbations [85, 36], meridional winds [61] and finite E region conductivities. Since the co-ordinated measurements of all these parameters are not available during the campaign, definite conclusion could not be derived. The shear in the zonal plasma along with specific temporal profile of vertical drift are shown [36, 88] to gives rise the confined bottomside ESF. The nature of seeding gravity waves [48, 33, 34] greatly alters the occurrence of spread F [85, 36]. It was shown by sekar et al [85] that for the generation of the bubbles, the amplitude of seeding perturbation must be greater than some threshold which depend on the effective vertical velocity as defined by them. Huang and Kelley [36] have pointed out that the timing of the seed gravity wave and its direction of propagation with respect to the zonal direction are crucial factors for the ESF generation.

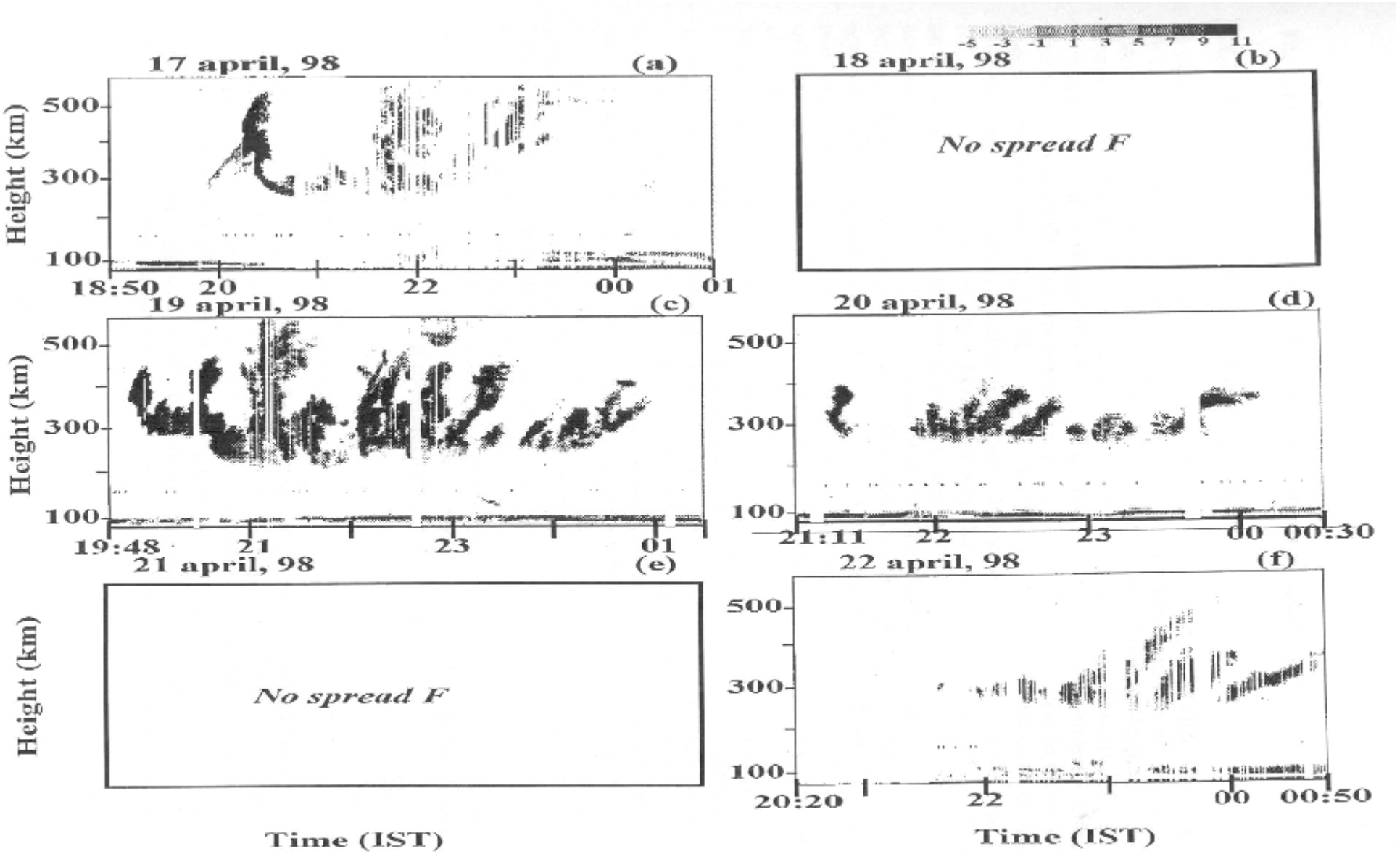

Figure 3.

4.3.3 Vertical erect and tilted plume structures

As clear from fig. 1 that the plumes are generally vertically erect till 22:00 IST while they are found to be westward tilted later. Both eastward and westward tilts are common features observed over Jicamarca [109] while the vertical erect plumes are frequently observed over Kwajalein [42]. Moreover over the Jicamarca the westward tilts of plumes are accompanied by the eastward tilt on the bottomside [109] which are absent in the tilted plumes observed by us. The tilts in the plumes are attributed to the shear in the zonal plasma drift [109, 100, 113]. Heelis et al [30] showed a buildup in velocity shear sometime between 1800:-2300 LT which is experimentally verified by incoherent scatter radar [18, 57, 56] over Jicamarca and by coherent scatter radar [104] over Kwajalein. These observations also reveal the existence of positive shear at lower altitude and negative shear at higher altitudes. The positive (negative) shear at lower (higher) altitudes in eastward flowing plasma was shown [113] to tilt the plumes eastward (westward) which finally resembles the 'C' shaped plume structure observed over Jicamarca. The reversal of zonal plasma drift from westward to eastward takes place during local sunset time. Moreover, the Barium cloud experiment [70] shows the significant positive shear at lower F region altitudes.

The observations presented in fig. 1 show the westward tilted plumes only after 22:00 LT which means that the shear in the zonal plasma drift becomes significant later after 22:00 LT over Indian longitudinal sector. This time is well within the time range given by Heelis et al [30] for build up of a velocity shear. However it differs from observations over Jicamarca which reveal the strong shear right at the local sunset time and continued till premidnight [20]. The absence of 'C' shaped structure of these tilted plumes, on the other hand, indicates that the *shear are not significant at lower F region altitudes in equinoctial period during evening and premidnight sector over Indian longitudinal sector.*

This particular feature of shear is remarkably different from the feature observed over Jicamarca. Though the Barium cloud experiment over Indian longitudinal sector shows the significant positive shear but the experiment is limited to altitude below 300 km at local sunset. In this way, the present observation is important for inferring the temporal and altitude information of shear throughout the F region heights.

4.3.4 The topside electron density

In addition to vertically erect plumes, the *ESF* structures are found to have less zonal extent similar to the observations over Kwajalein [42]. The shears in the zonal plasma drift control the tilt of the *ESF* structures, but not the zonal extent of the structures. However, the zonal extent of the plasma structures in the topside of the ionosphere was shown [84] to depend on the background topside electron densities. In this context, simultaneous topside electron density distributions are needed to make such comparison over the Indian longitudes.

4.3.5 The absence of backscatter in the valley region

The extremely narrow scattering structures in the valley region are often sen over Jicamarca [109]. The absence of such structures in present observation (fig. 1) over Gadanki

is noted earlier also [68, 69] and it is similar to the observations over Kwajalein [42]. The absence of such layered structure over Kwajalein is attributed to the inefficient mapping of them to low latitude station due to the lower altitude of the valley region [42]. The present observation strengthen the above reasoning since Gadanki is more off-equatorial than Kwajalein.

4.3.6 The Doppler velocities

In fig. 4, the RTV maps corresponding to ESF nights shown in fig. 1 are depicted. The nights when the AMBB were prominent, show the remarkably different velocity features compared to nights with less prominent AMBB. On this basis we have discussed the Doppler velocity features separately for prominent and non-prominent AMBB cases in following subsections.

Doppler velocities when AMBB are less prominent

The nights 25 march and 30 march 98 falls under this category. In general, the Doppler velocity maps reveal two different forms for bottom side structures and the plume structures. The bottom side structures usually exhibit oscillatory features with upward and downward polarities alternatively with magnitudes not exceeding a few tens of ms^{-1}. In contrast to that, the Doppler velocities at the center of the plume structures are normally directed upward with the magnitudes varying from 70 ms^{-1} to 350 ms^{-1} from a day to another. These plume structures are usually stronger in signal strength. Such structures have considerable variations within the structure (in the zonal direction) with the central portion having larger upward drift flanking with the lesser downward drift on the edge of the structures similar to the results obtained by the numerical simulation [83].

Doppler velocities when prominent AMBB are present

The bottomside structure, in this case, also exhibit the oscillatory velocity feature as for earlier case. However the magnitudes are remarkably different especially the downward velocities which are observed during the descending phase of AMBB. The velocities are found in 70 -150 m/s range much above the ambient downward motion. The plume structures which are seen during the descending phase of AMBB, sometimes move downward with very large velocities (as in 18 march 98, 13 april 99) or move upward also (as in 23 march 99). The strength of echoes from the downward moving plumes suggests their large degree of depletions. Only few observations [48, 42, 69] revealed such morphology and dynamics of depletions. First attempt to explain the generation of depletion during descending phase of AMBB was made by Kelley et al [48]. Their study revealed that the westward tilt (descending phase) created by some long gravity wave on the bottomside provides the favorable condition for small wave mode to grow as plumes provided zonal winds and ambient vertical electric field are significant. This idea has been verified by Huang and Kelley [34] numerically. These studies emphasize the necessity of one longer and one shorter gravity wave modes consistent with the morphology of the ESF which they observed. However their study was restricted to explain the morphology and not the Doppler velocity features. Our observation shows sometime upward and sometime very large downward velocity of plumes seen during descending phase of AMBB. These unexplained features require more attention and are dealt in the next chapter.

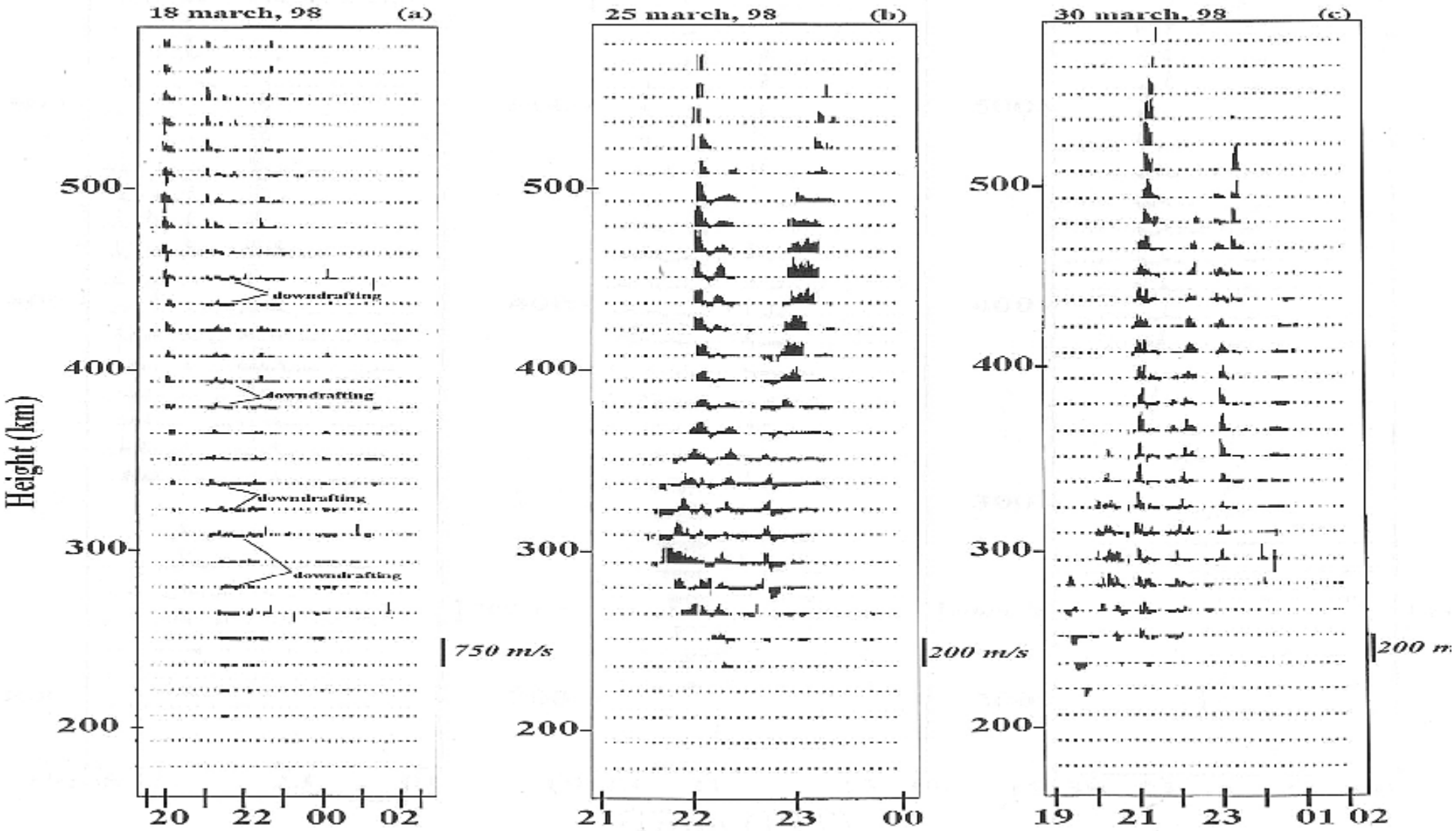

Figure 4.

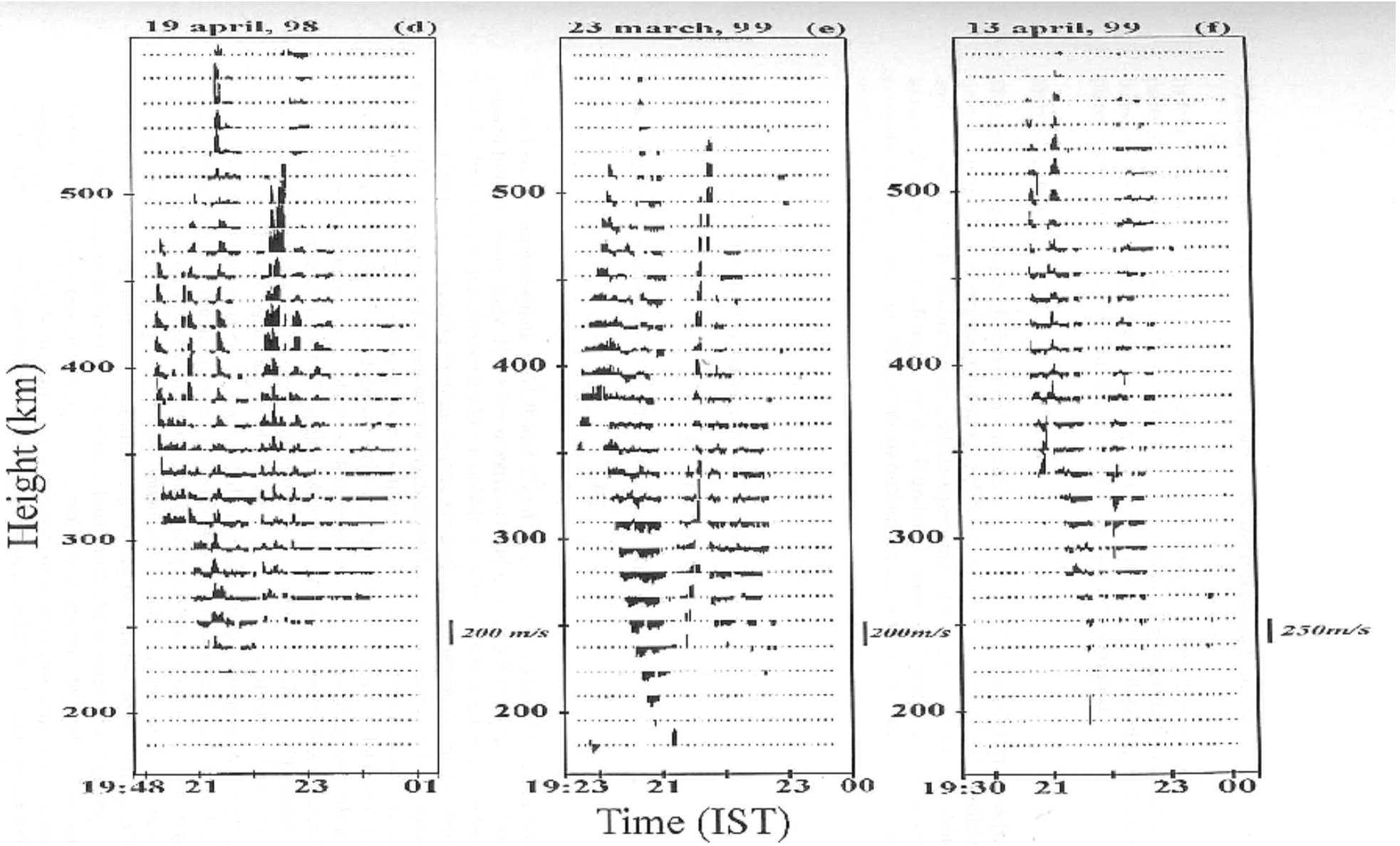

Figure 4.

In following subsection we would like to draw attention on some other interesting aspects of Doppler velocities observed on 18 march 98 and tried to explain them on the basis of nonlinear analytical expression given by [64]. The downward moving highly depleted regions during descending AMBB is also discussed in this context.

March 18, 1998

The motion of plasma depletion or enhancement under the influence of gravity, electric field and neutral winds has been the subject of investigation [24, 67, 64, 2, 58]. Ossakow and chaturvedi [64] have derived the analytic expression for linear and nonlinear bubble uprise velocities. The nonlinear velocity is found to depend on degree of depletion and geometry of the bubble. For elliptical shape bubble, the vertical velocity in the rest frame of ambient plasma is :

$$\vec{V} = \frac{\vec{E}}{B} \times \hat{b} + \frac{E^*}{B} \times \hat{b} \left[\frac{\frac{a\delta n}{n_1}}{b + a(1 - \frac{\delta n}{n_1})} \right] \tag{4.2}$$

where $\vec{E}$ is the electric field in the neutral wind frame i.e.;

$$\vec{E} = \vec{E}_o + B\vec{u} \times \hat{b}$$

E_o is the ambient electric field, E* is effective electric field [64]:

$$\vec{E}^* = \vec{E} + \frac{B\vec{j}}{\nu_{in}} \times \hat{b}$$

$\hat{b}$ is unit vector along magnetic field, B, and 'a' and 'b' are vertical and horizontal dimensions of bubble respectively. The effect of vertical wind is included in the above expression. Laakso et al [58] has derived the linear bubble velocity by including the wind effect. It is seen from the expression that the relative strength and direction of zonal current produced by these three agencies separately decides the vertical velocity of the bubble. The gravity induced bubble motion is always upward since it drives the eastward current. The bubble motion due to zonal electric field and vertical wind field may be upward or downward depending on their polarities. Moreover since the effect of these fields are dominant in the lower altitudes of F region while the gravity induced effects are dominant in the higher altitudes, the significant variation of bubbles velocity over the altitude can occur. The altitude region above which the gravity effects dominate is found near 400 km [64]. However the effect of electric and wind field can be extended to as high as 500 km if one considers the flux tube integrated Pederson conductivity and density [2]. It follows from the bubble velocity expression that bubble may have upward velocity larger than the ambient velocity ($\frac{E_0}{B}$), may have downward velocity larger than the ambient downward velocity but in the lower altitude region, may be pinched off i.e. higher portion moves upward while lower portion moves downward. The upward velocity as high as 300 m/s is commonly observed during prereversal enhancement [109, 100, 69] and can be explained by eq. (4.2). Sometime supersonic velocity of the upwelling bubble is also observed [42, 1]. The enhanced downdrafting of plasma depletion during electric field post-reversal is observed by in-situ probes [58] and Indian MST radar [68]. This aspect in particular, is also explained from (4.2) by considering the westward electric field and upward wind which cause bubble to move downward under the action of CRT instability

[58].
However one needs to be careful in interpreting the radar observation due to the following reason:
(1) The radar doesn't distinguish the depletion and enhancement region.
(2) The VHF radar detects meter size irregularities and thus the Doppler velocities observed should correspond to the motion of this small scale size irregularities rather than the velocities associated with the large scale plasma bubbles.
The coordinated measurements [75, 103, 51] during spread F reveal that the plume structures are indeed the plasma depletion. Therefore so far as the upwelling structures seen by radar are concern they are safely considered as the plasma depletion.
Costa and Kelley [14] suggested that the CRT instability nonlinearly evolves to the vertically steepened structures owing to the vertical advection. The steepened structures of scale size as small as 50m was observed. Near the ion gyro radius these steep density gradients are found to be unstable for collisionless [15] and collisional drift wave [40] causing the generation of small scale irregularities. In collisional regime the collision brings the severe condition on the upper limit of plasma density for growth rate to overcome the ion viscous damping near the ion gyro radius. The study of steepened structures [43, 44] reveal that the zonal component of polarization electric field dominates at large scale while the vertical component dominates at small scale (< 300m). Moreover since the drift waves have slower phase velocities, the mean Doppler shift observed by radar represents the guiding center drifts rather than the drift waves [42]. In other words, the Doppler velocities represent the drift of large scale plasma plasma bubble generated by GRT instability mechanism.

The observation on 18 march 98 reveal several interesting features of motion of plume structures. The vastly different velocity features are noticed in the plume structures observed at different times. In the section 4.3.1 it was discussed that the initial seeding of gravity wave could give rise the regular spaced plume structures. When such wave rides over AMBB caused by some another longer wave then plume structures with different features are generated. The plume structures seen during 19:30-21:00 LT moves upward with velocities as large as 350 m/s. Over Indian sector, the field reversal takes place after 20:00 LT [46, 62]. The combined effect of gravity and eastward electric field as well as higher altitude of F layer gives rise such high velocities [81, 64]. The morphology of the structures seen during 21:00 22:00 LT are quite similar to that of structures observed over Kwajalein [42]. By this time the field changes its polarity to westward. The descending bottomside undulation seen just after the reversal has upwelling structure which also moves downward. In fig. 5, the RTV plot corresponds to descending modulation is only shown. It clearly reveal that the upwelling structure during descending phase moves downward with as large as 100 m/s. The geometry of structure, in fig. 1(a), indicates that it may be originated at the time of field prereversal as a upwelling structure but could not grow to gravity dominated regime due to the reversal of the field which then causes it to move downward as well as confined it to the electric and wind field dominated regime. It is crucial to note that this plume structure must originate just before the post-reversal unlike the earlier plume structures which spent enough time before the reversal takes place. Since seeding of all the plumes are spatial in nature (gravity wave), such situation could occur if seeding is nonuniform spatially i.e.; if the seeding perturbation is superposition of more than one wave. It follows from the nonlinear velocity expression that the maximum downward velocity of 100 m/s near 280 km altitude ac-

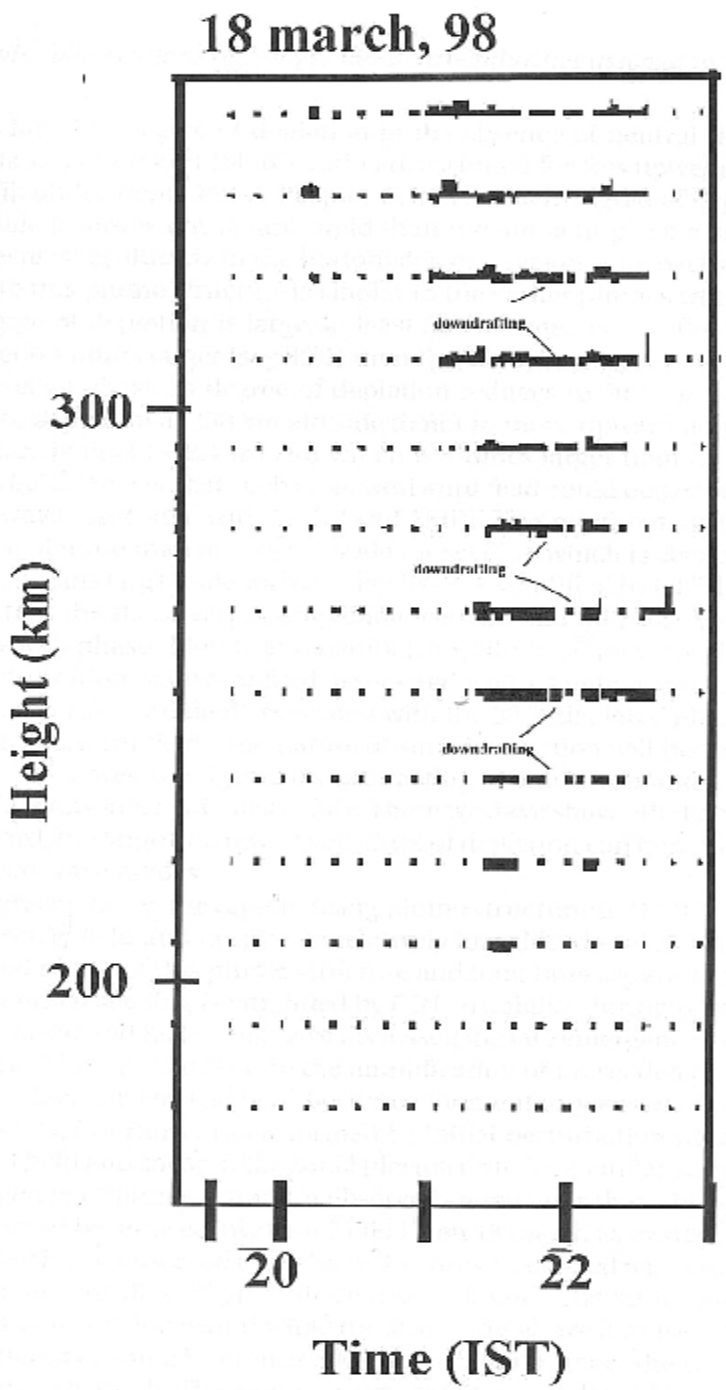

Figure 5.

counts for 50 % degree of depletion in the absence of neutral wind if 20 m/s ambient downward motion and 1:4 axis ratio are assumed for this upwelling structure. However it is difficult for depletion to keep or achieved such degree of depletion in the bottomside while it moves downward rapid than the ambient plasma since density decreases with decreasing altitude in the bottomside of F region. The backscattered echoes correspond to this plume structure is similar to the earlier plumes which implies that indeed the degree of depletion is large, at least 50%. It means that the it acquired the degree of depletion much larger (say 80%) than the 50 % during prereversal phase while during post-reversal phase its degree of depletion reduces to 50%. In order to make the 80% degree of depletion at 350 km altitude to not to move upward requires very strong westward electric field ($\sim$ 2.4 mV/m) which is 3 times larger than the postreversal ambient electric field. We feel that such large westward field could be generated by the large scale gravity wave associated with AMBB and AMBE. This requirement strengthens the view of presence of more than one wave mode for seeding which is also evident from morphology of ESF. This large scale wave, which itself is amplified by GRT instability mechanism, is such that the its corresponding enhancement should pass through the radar during post-reversal phase. Moreover the initial amplitude of the wave should be such that the large polarization westward field associated with its enhancement overcomes the large polarization eastward field associated with the 80 % depleted plume when it adds to the ambient westward field. The nature of such interaction will become more clear in next chapter where we investigated the interaction of one longer and one shorter wave mode under the non-linear GRT instability. There we have shown that even if the ambient field is eastward, the large downward velocities of depletion can be achieved with the interaction of two wave modes.

It is surprising to see the rapidly rising plume structure at 21:00 LT despite the westward zonal electric field and despite its relatively low altitude ($\approx$ 250 km) of origin. The well developed phase of this plume structure and long time separation with last plume suggest that initial seeding is amplified by GRT instability during post-reversal phase itself. Recently Sekar and Kelley [88] have discussed the late emergence of plume observed over Jicamarca. They attributed it to the amplification of preseeded perturbation by GRT instability when the electric field becomes momentarily eastward during late midnight. The preseeded perturbation is formed by initial perturbation which was suppressed by westward field and shear in the zonal plasma drift. The similar situation may account for re-emergence of plume structure observed much later than the prereversal phase. Indeed the field became eastward at 21:00 LT on 18 march as evident from fig. 2(a).

It is interesting to observed the velocity features associated with last plume which is tilted westward and having origin altitude near 250 km. The structures below 300 km predominantly move downward while the structures above it move upward. The very weak backscattered echoing layer near 300 km seems to connect the two structures where velocities are very small. This plume structure seems to follow the morphology of pinched-off bubble [58, 69]. It is to be noted that it is observed during late premidnight sector when the downward wind usually reverses its direction. The structure might be originated during the time when the wind is downward which allows it to grow to gravity dominated regime similar to previous plume. However before it penetrates to the topside the wind field reverses causing the downward motion of the lower portion of the bubble that falls on the electric filed and wind dominated regime. The lower portion is found to move downward as high as 50 m/s near 250 km while the upper detached bubble moves upward with velocity as high as 100 m/s near 350 km. Both the velocities amount for

50 % degree of depletion at their corresponding altitudes if 15 m/s ambient downward motion, 20 m/s upward wind and 1:4 axis ratio are assumed. It is found moreover that the 300-350 km altitude region is cross-over region from electric and wind field to gravity dominated regime. The cross-over altitude region would map to the 350-430 km altitude region at the equator which implies that the local Pederson conductivity and density decides the bubble dynamics rather than the flux integrated quantities. The fourth plume structure which is confined below 400km also has large downward velocity below 350 km altitude. However it didn't show any pinched off morphology may be because it could not find enough time to grow to inertial regime before the electric field reversal takes place.

It follows from the above discussion that the present observation has varieties of phenomenon such as the enhanced downdrafting of depletion, the effect of downward wind to account for rapid rising bubble during post-reversal time and pinched-off bubble. This aspects are explained on the basis of existing theories [64, 58]. However the nonlinear simulation is desired to understand these features.

4.3.7 ESF event of 23 march, 99

The ESF event observed on 23 march 99 night (fig. 1(e)) is quite similar to the ESF observed on March 21, 1979 over Jicamarca [48]. The AMBB is quite prominent on this night compared to 18 march 98. Moreover irrespective of the descending and ascending phase, the velocities inside all the plumes are found to be upward. This feature differ from 18 march 98 event where depletion seen during descending AMBB strictly moves downward. Note that the AMBB is more prominent on this night and one would expect the plume seen during descending phase to move more downward than on 18 march 98 if the interaction of two wave modes are only considered. We feel that along with two modes, one need to take the effects of tilts of the ionosphere in to account which is not incorporated in eq. (4.2).

4.3.8 Late emergence of plume

The ESF event observed on March 19, 1998 (fig. 6(a,b)) shows the late emergence of plume along with early seen layered structure. Except for the first two descending plume structures, the morphology of the ESF during this night is quite similar to the ESF observed over Jicamarca on September 8, 1993 (reproduced in [88]). In their observation an intense bottomside layered structures during 20:30 22:30 LT was observed which formed the base for the spectacular plume structure seen at 22:30 LT. In present observation we observed the weak bottomside layered structure which do not clearly shows any connection with the spectacular plume structure seen at 21:45 LT. It can be attributed to the inefficient mapping of the the layered structure to low latitude station from the equator, the layered structure to low latitude station from the equator, which weakens and may cause the disappearance of the bottomside layered structure. The separation between the plume structures are found to be 100-150 km, which confirms the seeding as due to the gravity wave.

The descending narrow bottomside layer and first two plume structures can be formed if the seeding perturbation do not get enough time to grow before the reversal takes place. Comparison with h'F variation (fig. 2(b)) shows that the bottomside F layer descends

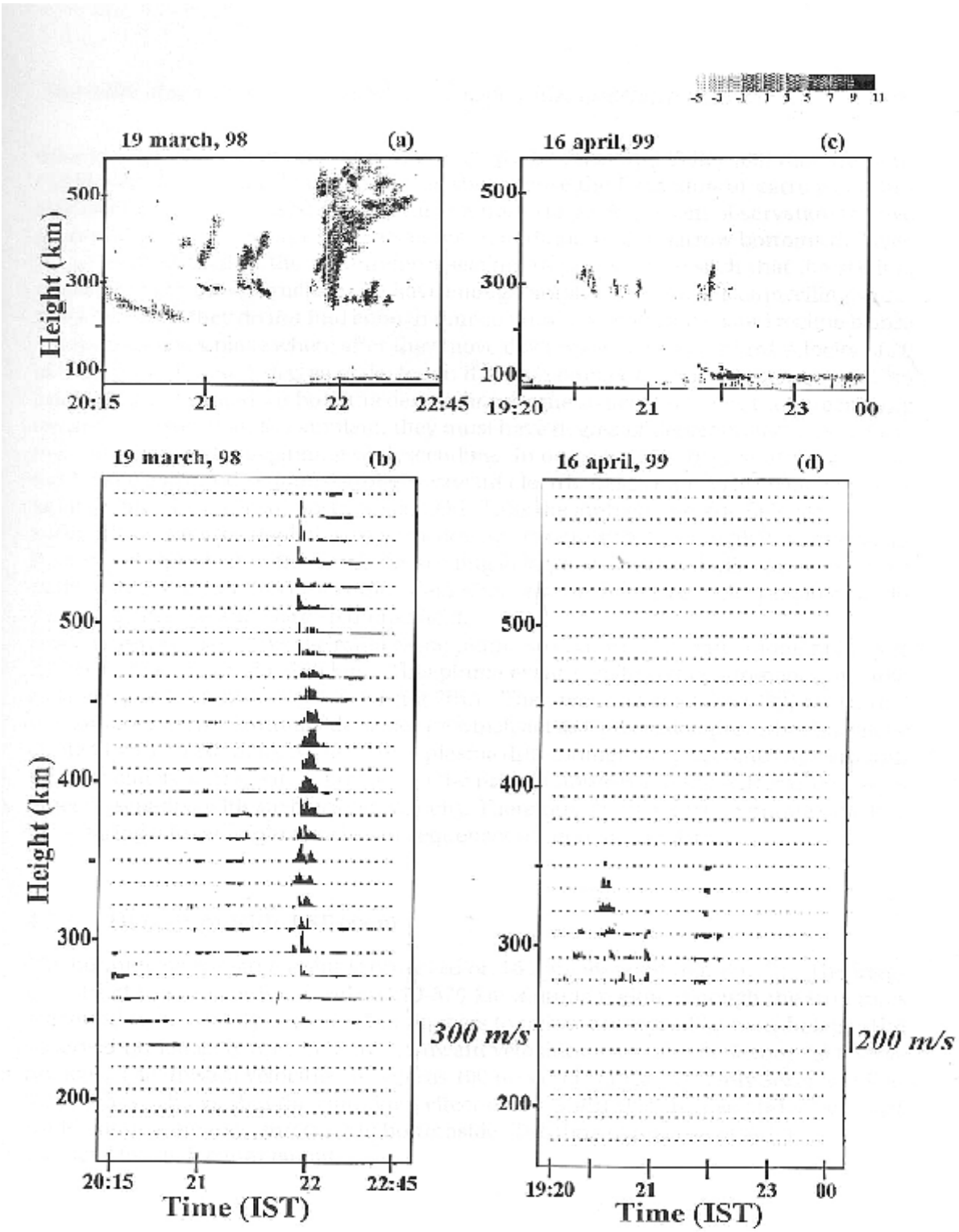

Figure 6.

downward during the observation. It was shown by Sekar and Kelley [88] that the combined effect of westward field and zonal shear cause the formation of narrow bottomside layer provided the seeding amplitude is not to large. In present observation the two descending plume structures are also seen in addition to the narrow bottomside layer. It can be attributed to the non-uniform seeding of gravity wave such that the seeding corresponds to these structures do have enough amplitude to grow as upwelling structures. However they do not find enough time to grow to gravity dominated regime before the reversal takes place where after they move downward. The downward velocity of 40 m/s accounts for 30 % degree of depletion if 30 m/s ambient downward motion and 1:5 axis ratio are assumed for both the descending plume structures. Since they are moving downward faster than the ambient, they must have degree of depletion larger (say 50%) than 30% just at the beginning of descending. In order for 50% degree of depletion to not to move upward requires strong westward electric field (1.8 mV/m) which is twice as large than the ambient postreversal field. Thus the ambient electric field alone is not sufficient to make the depletion to move downward with 40 m/s. Though it is not evident from the morphology of the event, the seeding of large scale wave similar to as discussed in the context of 100 m/s descending depletion seen on 18 March is the possible candidate for giving rise such large required field.
It is interesting to observe the rapid rising plume structure during late midnight in spite its low altitude of origin (250 km). This plume event is followed by momentarily rapid ascending of bottomside of F layer (fig 2(b)). The recent investigation [88] reveal that the confined narrow bottomside structure which act as a preseeded perturbation can be excited by CRT instability if the vertical plasma drift momentarily becomes upward with 40 m/s velocity during late midnight. In the present observation the bottomside F layer indeed ascended with such desired velocity. Therefore, the rapid rising plume structure seen during late midnight may be consequences of such mechanism.

4.3.9 The bottomside ESF event

The bottomside spread F event is observed on 16 april 99 night (fig. 6(c,d)) . The irregular structures are confined within 270-370 km altitude region. Though the structures are found to be zonally detached but appears to follow the wave-like morphology. The observed periodically upward and downward velocities over time do favour such morphology. The upward velocities as large as 100 m/s is observed. Recently Sekar and Kelley [88] have shown that the combined effect of westward electric filed and zonal shear could confine the ESF structures to bottomside. The time of reversal of ambient electric is crucial for such confinement.

4.4 summary and conclusion

We have examined some of the interesting events observed during equinoctial period, 1998-99. The multiwavelength morphology, enhanced downward motion of plumes, pinched-off plumes and late emergence of plume structures are some of the interesting aspects which we have tried to explain on the basis of existing theories. On the basis

of nonlinear analytical expression, it is shown that for enhanced downdrafting of depletions, more than one wave are needed for seeding of CRT instability. The late emergence of plume structures and bottomside spread F are discussed in the light of recent investigation [88].

4.5 Figure captions

- Fig. 1: The RTI maps on six nights: (a) 18 march 98, (b) 25 march 98, (c) 30 march 98, (d) 19 april 98, (e) 23 march 99 and (f) 13 april 99.
- Fig. 2: The temporal variations of bottomside F layer height on: (a) 18 march 98, (b) 19 march 98 (c) 25 march 98 and (d) 19 april 98.
- Fig. 3: The RTI maps on six consecutive nights: (a) 17 april 98, (b) 18 april 98, (c) 19 april 98, (d) 20 april 98, (e) 21 april 99 and (f) 22 april 99.
- Fig. 4: The RTV maps on six nights: (a) 18 march 98, (b) 25 march 98, (c) 30 march 98, (d) 19 april 98, (e) 23 march 99 and (f) 13 april 99.
- Fig. 5: The enlarge RTV plot during 20:00-22:00 LT on 18 march 98.
- Fig. 6: The RTI and RTV maps on 19 march 98 (a,b) and on 16 april 99 (c,d) respectively

Chapter 5

The simulation of multiwavelength morphology and downwelling of plasma bubbles

5.1 Introduction

The morphology and velocity features of ESF observed by Indian MST radar are discussed in previous chapter. The large scale bottomside modulating structure and the riding plume structures with different features during ascending and descending phase of bottomside modulation (BM) are seen on some nights. A similar morphology event was earlier observed and investigated by Kelley et al [48] on the basis of linear theory of GRT instability. The large scale zonal seeding of gravity wave was suggested as the possible candidate for large scale bottomside modulation. The presence of such wave was found to be essential for the generation of plume structures seen during the descending phase of BF layer. The nonlinear investigation [34] reveal that when both a seed gravity wave and a smaller-scale perturbations are used, indeed the large scale gravity wave determines the outer-scale of ESF irregularities and the smaller-scale perturbation results in multiple plumes preferentially located on the west wall similar to the observation [48]. However the investigation is restricted to wavelengths not exceeding more than 200 km and deals mainly with morphology. The earlier observations [48, 42] and observation presented in last chapter indicate the bottomside modulation with 600-1200 km scale size, over which plume structures with regular spacing of 100-200 km ride. Moreover in our observations, the plume structures exhibit lots of variabilities in the velocities. Interestingly the plume structures seen during descending bottomside modulation are some time found to descend with velocity much larger than the ambient. In last chapter, it was argued on the basis of nonlinear analytical velocity expression that the wave mode associated with BM can gives rise the additional westward electric field so that the plume structures associated with short wave mode descend downward much faster than the ambient. Thus its not only the morphology of the event but the velocity features also suggest the presence of more than one wave mode as seeding perturbation. Moreover, it is not always that the plumes observed during descending bottomside modulation moves downward but sometime they are found to move upward also. These are few aspects which need more attention now to understand our observations. In this chapter the interaction of two wave modes, one longer and one shorter, under the GRT instability is investigated. The objective of the investigation is to explain the different velocity features of plumes which were not dealt in earlier investigations.

5.2 Numerical simulation model

In the present investigation, the nonlinear numerical simulation model of ESF [71, 83] is adopted. As the irregularities are Earth's magnetic field aligned (z axis), the model was developed in a two-dimensional plane perpendicular to the geomagnetic field lines over magnetic dip equator. In this model, the basic plasma fluid equations applicable to the equatorial nighttime *F* region were reduced to the following two coupled partial differential equations in m.k.s.units.

$$\nabla.(\nu_{in}.N.\nabla\phi) = B[-g + W_y\nu_{in} + (E_{xo}/B)\nu_{in}]\frac{\partial N}{\partial x} \tag{5.1}$$

$$\frac{\partial N}{\partial t} - \frac{\partial}{\partial x}[(N/B)(E_{yo} + \frac{\partial\phi}{\partial y})] + \frac{\partial}{\partial y}[(N/B)(-E_{xo} + \frac{\partial\phi}{\partial x})] = -\nu_R N \tag{5.2}$$

Here N and ϕ represent the electron number density and the perturbation potential respectively. The symbols g, ν_{in}, ν_R and B correspond to acceleration due gravity, ion-neutral collision frequency, recombination rate and the strength of Earth magnetic field respectively. E_{xo}, E_{yo} and W_y are the background electric field components in zonal (x) and vertical (y) directions and vertical wind respectively. For further investigation, W_y and E_{yo} are not considered.

5.2.1 The simulation plane

The numerical calculations are performed in two-dimensional Cartesian plane where the positive $\hat{x}$ and $\hat{y}$ axes represent westward and upward direction respectively. The differential equations are solved over the region of 300 km east to 300 km west in zonal direction and over 182 to 532 km in vertical direction. The grid sizes are chosen to be uniform with the values of $\Delta x = 3$ km and $\Delta y = 2$ km. The vertical line corresponding to x=0 km is referred as the zero reference longitude for the future discussion.

5.2.2 The boundary conditions and initial conditions

As the problem of interest is to study the growth of the periodic perturbation in ion density in zonal direction, periodic boundary conditions are imposed on N and ϕ in the zonal direction. In vertical direction, transmitive boundary conditions on number density

$$\frac{\partial N}{\partial y} = 0$$

and Neumann boundary conditions on ϕ

$$\frac{\partial \phi}{\partial y} = 0$$

are imposed.

5.2.3 The numerical scheme

The numerical scheme adopted by Sekar [90] is used for present simulation. The potential equation is solved using a line by line successive over relaxation method by maintaining the skew symmetry in the zonal direction.
The continuity equations are solved by explicit finite difference method (Lax-Friedrich and Lax-Wandroff schemes) with flux corrected transport (FCT) technique [111].

5.2.4 The inputs for simulation

The basic inputs required to the simulation are
(1) the altitude profile of ν_{in},
(2) the altitude profile of β,
(3) the altitude profile of electron number density
(4) the temporal variation of zonal electric field E_{xo}.
The altitude profiles of ν_{in} and β are same as in fig. 1 of chapter 3. The altitude profile of the electron density with a minimum scale length of 15km and peak altitude of 410km used in the simulation, is depicted in figure 1a. In figure 1b the ambient vertical plasma drift ($\frac{E_{xo}}{B}$) corresponding to background zonal electric field (E_{xo}), used in the simulation is shown as case I.

5.2.5 The form of initial perturbation

The density perturbation is chosen of the form:

$$N(x,y) = N_0(y)(1 - a\cos[\frac{2\pi}{\lambda}(x+\psi)])$$

for a single wave length mode and

$$N(x,y) = N_0(y)[1. - (a_1\cos[\frac{2\pi}{\lambda_1}(x+\psi_1)] + a_2\cos[\frac{2\pi}{\lambda_2}(x-\psi_2)])]$$

for superposition of two modes.

In the above relations the plasma densities at a given altitude (y) for various zonal distances (N(x,y)) are described in terms of sinusoidal perturbation along zonal direction over the unperturbed plasma densities $N_0(y)$ at that particular altitude while a, λ and ψ denote respectively the amplitude, wavelength and the phase of the initial perturbation. Here the suffixes 1, 2 represent two modes.

5.2.6 Cases considered for investigation

By varying the parameters a, λ and ψ, number of cases are considered for the present investigation. These cases are enlisted in table 1.

5.2.7 Method of illustrations

The continuity equation provides the temporal evolution of zonally perturbed altitude profile of number density of both the ions. Instead of plotting the altitude profile for each zonal distance at any instant of time, the contours of constant density are plotted

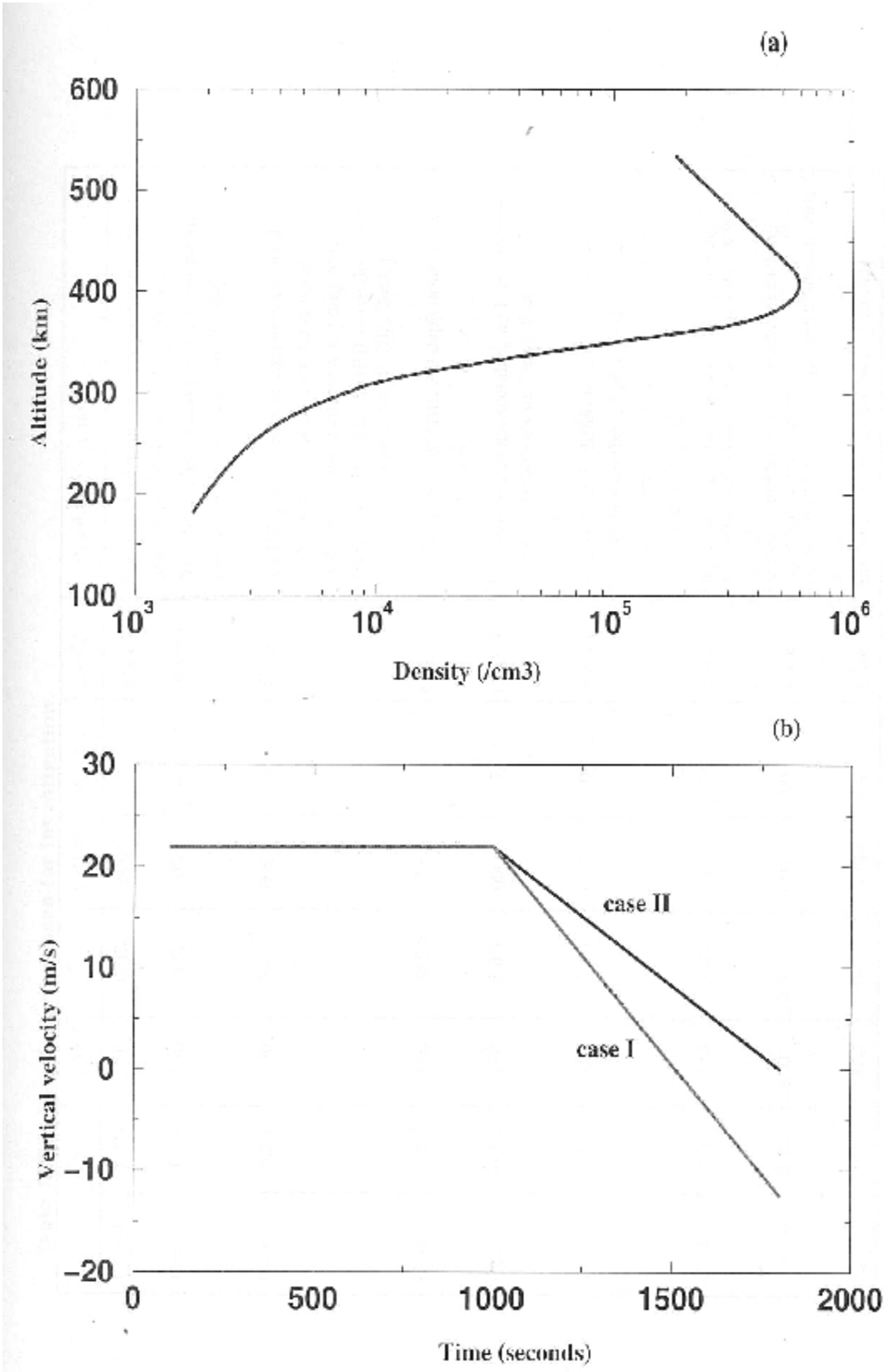

Figure 1.

Table 1: The list of cases chosen for investigation.

	a_1	λ_1 (km)	a_2	λ_2 (km)	$\psi_1 - \psi_2$	Exo/B	Results [Figure no.]
Case 1	0.5%	150	0.0%	600	~	Case I	Periodic depletions and enhancements moving upward and downward. [fig. 2(a,b)].
Case 2	0.0%	150	5.0%	600	~	Case I	Periodic depletion and enhancement moving upward and downward [fig. 2(c,d)].
Case 3	0.5%	150	5.0%	600	0	Case I	AMBB associated with longer wave while depletions associated with short wave . Depletions (50%) during ascending and descending phase of AMBB move downward. much larger than ambient. [fig. 2(e,f)]
Case 4	5.0%	150	0.5%	600	0	Case I	No prominant AMBB. All depletions move upward [fig. 2g].
Case 5	0.5%	150	5.0%	600	0	Case II	Depletions during ascending and descending phase move downward larger than case 3. [fig. 2h]
Case 6	0.5%	150	5.0%	600	90	Case I	Morphology is different from case 3 though AMBB are similar. Degree of depletions and downward velocities considerably differ from case 3. [fig 2i].
Case 7	1.0%	150	5.0%	600	90	Case I	Degree of depletions of downward moving depletions and velocities are larger than case 6. [fig. 2j]
Case 8	0.5%	150	6.0 %	600	90	Case I	Degree of depletions of downward moving depletions are lesser and downward velocities are greater than as in case 6 [fig. 2k]
Case 9	0.5%	300	5.0%	1200	180	Case I	No development of bubbles. [fig. 2l]

over the simulation plane.
The potential equation provides the spatial structure of potential at any instant of time. The velocity defined by

$$\vec{V} = \frac{1}{B^2}(-\nabla\phi \times \vec{B})$$

is plotted instead of plotting the potential contours.
Both isodensity contours and velocity vectors are plotted in same graph. At the same time, by knowing the instantaneous profile of background electron density, the iso density depletion and enhancement contours over the simulation plane are also depicted in few cases. For single wave mode, the instantaneous profile is obtained by running the simulation without perturbation but keeping all other parameter same. However for two wave mode one need to be careful of calculating it. It was seen during the observations presented in previous chapter that the h'F variation follows the longer wave morphology associated with AMBB and AMBB indeed can be used as a tracer for the AMBE Thus for two wave mode perturbation, the instantaneous profile of electron density is obtained by running the simulation with longer wave perturbation.

5.3 The general features of interaction of two wave modes

In order to see the changes which occur in the evolution of GRT instability with seeding of two modes as compared to single wave mode, the single wave modes are also considered.

5.3.1 Results

The results corresponding to case 1 for single shorter mode are depicted in fig. 2(a,b). The up-welling structures in fig.2a corresponds to depletions in fig. 2b. The maximum degree of depletion and upward velocity are found to be 50% and 30 m/s. The up-welling structures or depletions are extended to 400 km much below the F_{peak} altitude which is 450 km at 1800 seconds. The results corresponding to case 2 are shown in fig. 2(c,d). The up-welling structures or the depletions are extended to the 440 km with maximum degree of depletion and upward velocity as 80% and 55 m/s respectively. In both case (1,2), all the depletions move upward while all the enhancements move downward.
In fig. 2(e,f), the results corresponding to case 3 are shown. The morphology of the structure is such that the bubbles are seen with the regular spacing of 150 km which is the wavelength of shorter wave mode. However they seem to ride over the longer wave modulating structure on the bottomside. The bubble which is seen at the center has reached up to 460 km with maximum degree of depletion more than 90%. The bubbles which are seen at $\pm$ 150 km zonal distance have reached up to 400 km with maximum degree of depletion as 10%. Moreover the central bubble moves upward with maximum of 500 m/s while the other two **depletions move downward** with maximum of 30 m/s which is almost two times as large as the ambient downward motion (12.5 m/s at 1800 seconds). Further, the enhancement lying on either side of the central bubble moves downward with maximum velocity of 40 m/s.
The results corresponding to case 4. is depicted in fig. 2g. The well developed bubbles with 150 km spacing are seen with no signature of any prominent bottomside modulation. All the bubbles are moving upward with very large velocities.

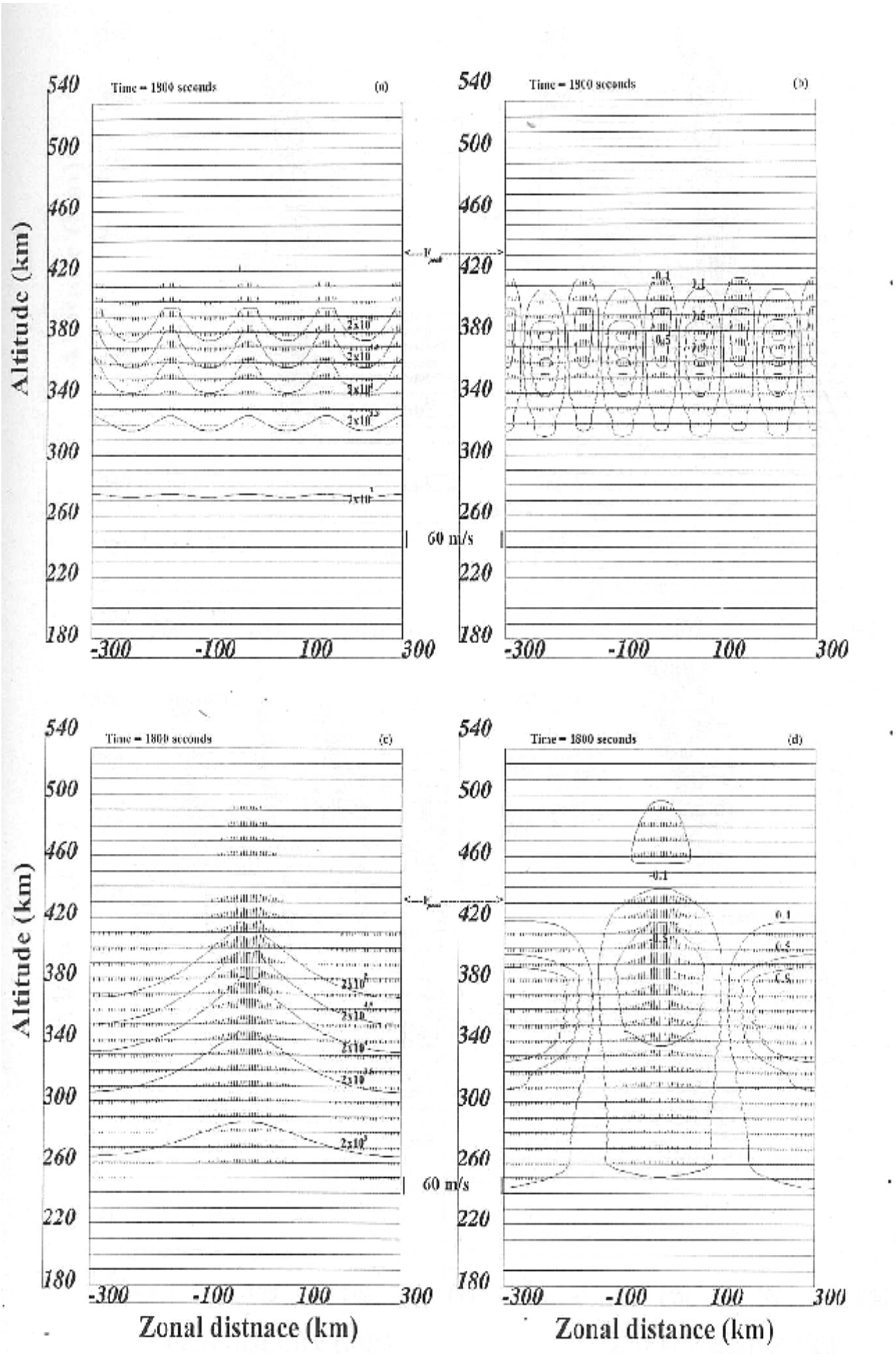

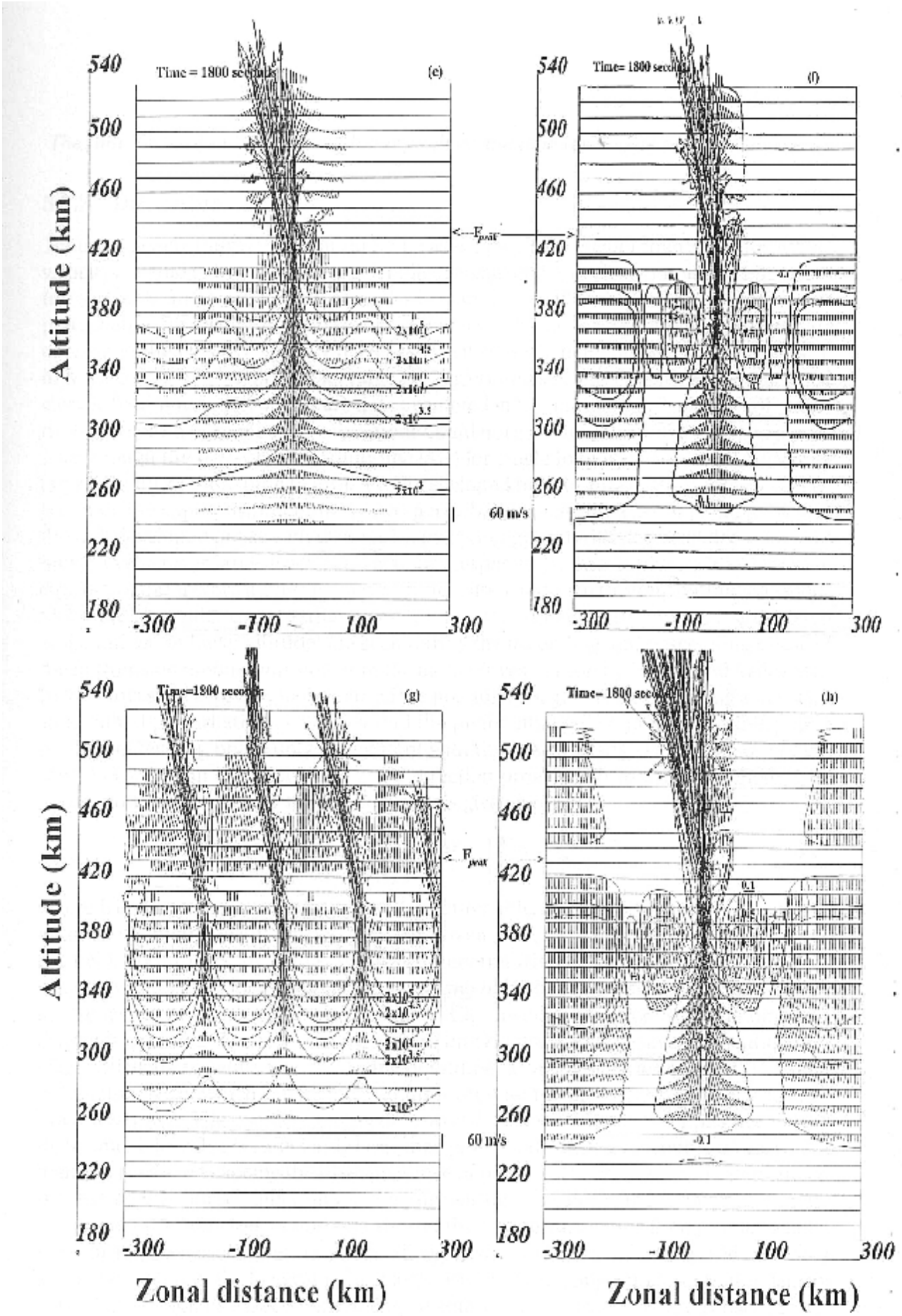

Figure 2.

5.3.2 Discussion

Though the maximum depletions in both cases 1 and 2 are greater than 50%, the bubble velocity is found to be below 60 m/s. It indicates the moderate development of ESF structures in both single wave mode case. Earlier simulation [85] with the 0.5% amplitude of perturbation for small wave mode was shown to evolve as well developed ESF structure only when the effective velocity (effect of gravity,electric field, downward wind) was 70 m/s. However, in present case its value is 22 m/s equals to the velocity due to the zonal electric field since other effects are not considered in the simulation. Thus the ESF structure correspond to single short wave mode could not grow into the well developed phase. Even though the perturbation amplitude (5%) for single long wave mode is sufficiently large, it requires more time to form a well developed bubble, due to the nonlocal effects. However the superposition of these two perturbations, i.e. the case 3, could grow into the well developed phase with distinguish morphology and with degree of depletion and upward velocity as large as 90% and 500 m/s respectively. The bubbles with separation equals to shorter wave mode are seen with clear association to the long bottomside modulation (BM) similar to the earlier investigation [34]. The bubbles (though less depleted and confined to lower altitude) are seen during the ascending and descending phase of the bottomside modulation similar to the earlier investigation by Huang and Kelley [34]. In their investigation, they had explored the possibility of gravity wave seeding along with small initial perturbation also and found the preferential generation of multiple plume on the descending phase only , consistent with the observations. The presence of long wave perturbation propagating in zonal direction provides tilt to the ionosphere. The linear growth rate (γ_{tilt}) for tilted ionosphere is given by [48]:

$$\gamma_{tilt} = \left[\frac{-E_{xo}}{B} + \frac{g}{\nu_{in}}\right]\frac{cos\alpha}{L} + \left[\frac{E_{yo}}{B} - W_x\right]\frac{sin\alpha}{L} \tag{5.3}$$

where L is the gradient scale length on the bottomside, α is the tilt angle positive for an ionosphere tilted upward moving from west to east, E_{xo}, E_{yo} and W_x are westward electric field, upward electric field and westward neutral wind respectively. The tilt angle, α, is negative (positive) for ascending (descending) of bottomside backscatter (BB). Hence its the last term which biases the growth of CRT instability during the ascending and descending phase. The terms in the square bracket are zonal plasma drift and neutral wind which are usually eastward during nighttime. Moreover the former is either equal or less than latter which can be inferred from whether the plumes are vertically erect or tilted westward. The coefficient of $sin\alpha/L$ would be then either zero or positive during nighttime. If its value is sufficiently large then growth rate during ascending phase would highly get reduced causing the disappearance of plumes [48]. In normal circumstances, the plasma drift doesn't differ much from the neutral wind and so the coefficient is small. If one then uses one longer and one shorter density perturbations then plumes will be seen during both ascending and descending phase as one of case investigated by Huang and Kelley [34] reveal. However if the gravity wave is used along with one shorter density perturbation then its associated zonal wind adds to the neutral wind and causes the coefficient to become large. It then suppresses the generation of plumes during the ascending [34]. In our investigation we have not incorporated the effects of vertical electric field and zonal neutral wind and also the effect of tilt angle. Moreover we neither included the gravity wave associated winds in our calculation. In spite of all these, the generation of bubbles are seen both during ascending and descending phase. Moreover these bubbles

are found to move downward similar to our observations. In contrast to case 3, case 4 neither shows any prominent bottomside modulating structure nor the downward moving bubble. These two cases throw some light on how the interaction of two wave mode is operating under CRT instability. The distinct features for these two cases can be attributed to the relative amplitudes of participating wave modes. The amplitude of longer wave mode is 10 times larger than the shorter wave mode in case 3 while it is opposite in case 4. In case 3, the initial large amplitude of longer wave zonally alters the ambient ionosphere by creating the depletion and enhancement. This zonal varying ionosphere acts as an ambient for small amplitude short wave mode. Some of the initially small depletions of short wave mode fall on the large scale ambient depletion now while others fall on the enhancement. Obviously the former become more depleted while latter become less depleted compared to the initial amplitude which is 0.5%. At the same time, the former see the large scale eastward field while latter see the westward field opposite to its own short scale eastward field. Since the short wave mode has smaller initial amplitude than the longer one, the net electric field for latter depletions would be westward. In contrast to it, in case 4, however all the depletions see the net eastward field due to large initial amplitude of shorter wave mode as compared to the longer wave mode. Both the modes now evolve and so as their polarization field under GRT instability. In case 3, longer wave grows faster than shorter wave mode since its amplitude is sufficiently large. The evolution of large scale mode with time would give the prominent bottomside in case 3 as its initial amplitude is sufficient to grow. In case 4, the absence of bottomside modulation confirms this argument since initial amplitude of longer wave mode is not sufficient to grow in this case. With the effect of westward field in the enhancement region, in case 3, some of the depletions of short wave mode then move downward while the other which fall on depleted region safely move upward due to net enhanced eastward field. *In brief, longer mode provides the additional ambient electric field which itself is evolving with time. Its eastward field causes the smaller amplitude short wave mode depletions to evolve in well developed phase which otherwise could not grow as in case 1. At the same time its increasing westward field causes some of the depletions, associated with shorter wave mode, to move downward with less degree of depletions provided its amplitude is sufficiently large.*

The effects of ambient electric field, relative phase, amplitude ratio and wavelength ratio for superposition mode

The result corresponding to case 3 is taken at 1800 seconds which is the time when ambient motion is downward as seen in case I of fig. 1(b). The question could be raised whether the downward motion of weakly depleted regions are mainly due to the ambient westward field or westward field associated with longer wave mode ? In order to distinguish out these two effects, case 5 is chosen for the simulation. Its result is depicted in fig. 2h. In this case, the ambient field is kept eastward till 1800s. Interestingly the weakly depleted regions move downward much faster in this case compared to the case 3. It is now well established [88] that the delay in the reversal of the ambient field causes larger growth of CRT instability. Since in case 5, the electric field reversal takes place later than as in case 3, both the modes evolve to much larger amplitude than earlier. Its effect then would be further prominent bottomside modulation, enhanced downward motion of depletion as well the increase in the degree of depletion of downward moving depletion as we see in fig.2h. This finding strengthen the argument given above that its the

evolving westward polarization field associated with longer mode which causes depletions to move downward.

On the basis of above arguments, one anticipates that the evolution of the ESF structures considerably varies with the variations in the relative phase, ratio of amplitudes and the wavelengths of both the single wave modes. In fig. 2i the result corresponding to case 6 is depicted. The shorter wave mode is shifted by 90° relative to un-shifted longer wave mode while keeping other parameters same as for case 3. The bottomside modulation similar as for case 3 is seen. However, in contrast to single well developed bubble in case 3, two well developed bubbles are seen. Their maximum velocities, though large, never exceed the maximum velocities of well developed bubble seen in case 3. Moreover in contrast to four descending depletions in case 3, two downward moving weak depletions are found during ascending and descending phase of BM. The unaltered bottomside modulation indicates that it is merely due to the longer wave whose parameters are unaltered. Due to phase shifting of shorter wave mode compared to longer wave mode, two of its depletion now falls on depletion of longer wave mode while other depletions fall on enhancement of it. We have investigated the two wave interaction with 180° and 270° relative phase and found the significant difference in morphology of ESF and motion of depletions. The study thus reveal the importance of relative phase between modes to decide the morphology and velocity features of ESF structures. Now we will investigate the effect of relative amplitudes of two modes in the evolution of ESF structures.

In fig. 2j, the results correspond to case 7 is presented. The two well developed bubbles seen in case 6 are grown to further stage in case 7. More interestingly, the enhanced degree of depletions and downward velocities of the depletions seen during the ascending and descending phase of BM are found as compared to case 6. It is to be noted that the amplitude ratio of shorter to longer wave mode is 1:5 in present case while it was 0.5:5 in case 6. It is the increases in the amplitude of the shorter wave mode which causes the increase in the degree of depletion of both well developed bubbles as well as the bubbles seen during ascending and descending phase. By increasing the amplitude of short wave mode and keeping the amplitude of longer wave mode unchanged, one should expect the downward moving bubbles to slow down compared to the case 6 since they have now large eastward field compared to case 6 to oppose the westward field associated with the enhancement of the longer wave mode. We feel that the enhanced downward motion is due to the nonlocal effect. The evolution of two well developed bubbles to further stage in case 7 causes either side of their structures to also develop in further stage and thus increasing their velocities. Thus the increase in amplitude ratio of shorter to longer mode, but still less than unity, produces the higher degree of depletions with larger downward velocities.

The results presented in fig. 2k correspond to case 8. The degree of depletion seen during ascending and descending phase are less than case 6 while the downward velocities becomes larger than as in case 6. It is obvious because the amplitude of longer wave mode is increased which causes the depletions of shorter wave mode, which fall on its enhancement, to diminish as compared to case 6. At the same time its enhanced westward field enhances the motion of this depleted region.

In fig. 2(l), the result corresponding to case 9 is presented. To accommodate the effect of increase in both wavelengths, their phases are also increased by same factor compared to case 6. No bubbles are seen in this case which indicate that the choice of wavelengths are also crucial for nonlinear development of GRT instability. In brief our present investigation reveals that

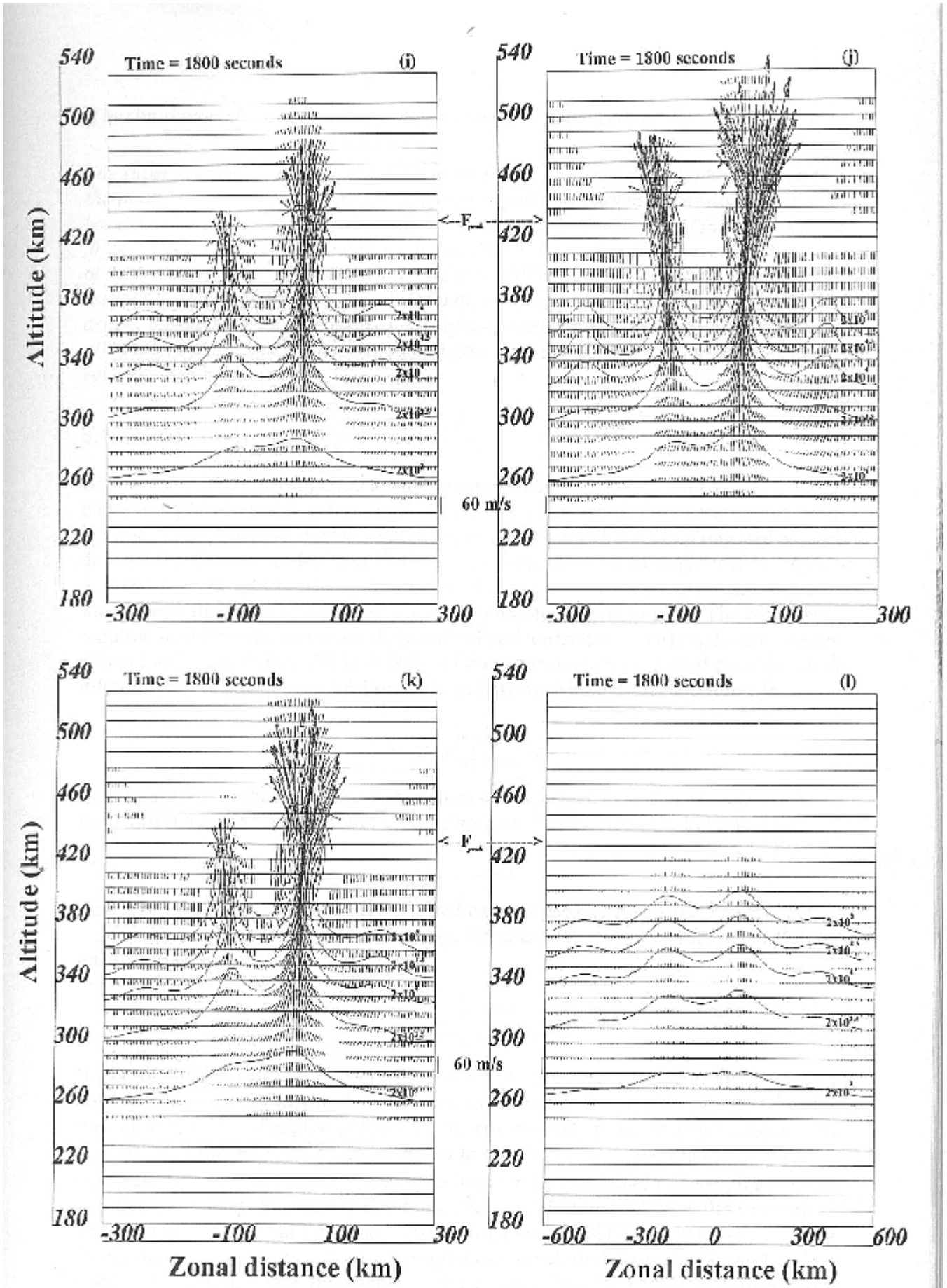

Figure 2.

The superposition of longer and shorter wave modes gives rise the morphology such that the plume structures correspond to shorter wave mode are having clear association with bottomside modulation (BM) due to the long wave mode. The too small initial amplitude ,0.5%, for short wave mode could grow into the bubbles when it falls over the depletion of longer wave mode. At the same time the depletions seen during the descending and ascending phase of BM move downward with varying degree of depletions and velocities depending on the relative phase and ratio of amplitude. By suitable choice of relative amplitude and phase and relative wavelength, the large degree of depletions and downward velocities can be achieved.

5.4 A case study

We now extend our investigation further to explain some of the ESF features observed by patra et al [69] as shown in fig. 3(a,b). The observation reveal the two wave morphology and enhanced down drafting of ESF structures. During descending phase of BM, the descending plumes are also seen. The wave like structures on this night leads to the hypothesis that the gravity wave play a role in the process. The wide spectrum of gravity wave allows the range of waves which could possibly match the data. The parameters required to specify the waves are their vertical and horizontal wave length and frequencies in Earth fixed frame. The knowledge of these parameters for both the waves can be inferred from the dispersion relation of the gravity wave in neutral wind frame [54]:

$$\omega'^2 = \frac{(\omega_g k_x)^2}{(k_x^2 + k_y^2 + 1/4H^2)} \tag{5.4}$$

Here k_x and k_y are the horizontal and vertical wavenumber, H is neutral scale height, ω_g is the Brunt-vaisala frequency and ω' is the frequency in the neutral wind frame,i.e.;

$$\omega' = \omega_o - \vec{k}.\vec{u} \tag{5.5}$$

The ω_o is the earth fixed frequency and $\vec{u}$ is the neutral wind. The horizontal wave vector, k_x, is negative along the eastward direction. We choose the negative root of eq. (5.4) for our search of gravity waves.

$$\omega' = -\frac{(\omega_g k_x)}{(k_x^2 + k_y^2 + 1/4H^2)^{1/2}} \tag{5.6}$$

Hines [32] has shown that viscosity damps out all vertical variations at thermospheric heights with a wavelength less than a minimum vertical scale size. Above E region heights, thus all vertical wavelengths of less than 10 km are likely to be strongly damped. We assume the value of $\lambda_y = \frac{2\pi}{k_y}$ to be 20 km in our calculation. We then solve both the equations for ω' by taking the ω_o and k_x as independent variables and keeping wind, u, as a free parameter. During evening hours, neutral wind usually takes the value in 60 120 m/s range in eastward direction. We choose two values, 60 and 90 m/s for u. In fig. 3(c,d), the iso ω' contours of above two equations are plotted. Instead of k_x and ω_o, horizontal wavelength,λ_x and time period τ_o are plotted. The plot (c) and (d) correspond to 60 m/s and 90 m/s neutral wind values respectively. The values of contours are 0.0002, 0.0003,0.001, 0.0016 s^{-1}. The horizontal parallel lines are solution of eq. (5.6) and curved contours are solution of eq. (5.5). The intersection of contours of same values in $\tau_o - \lambda_x$

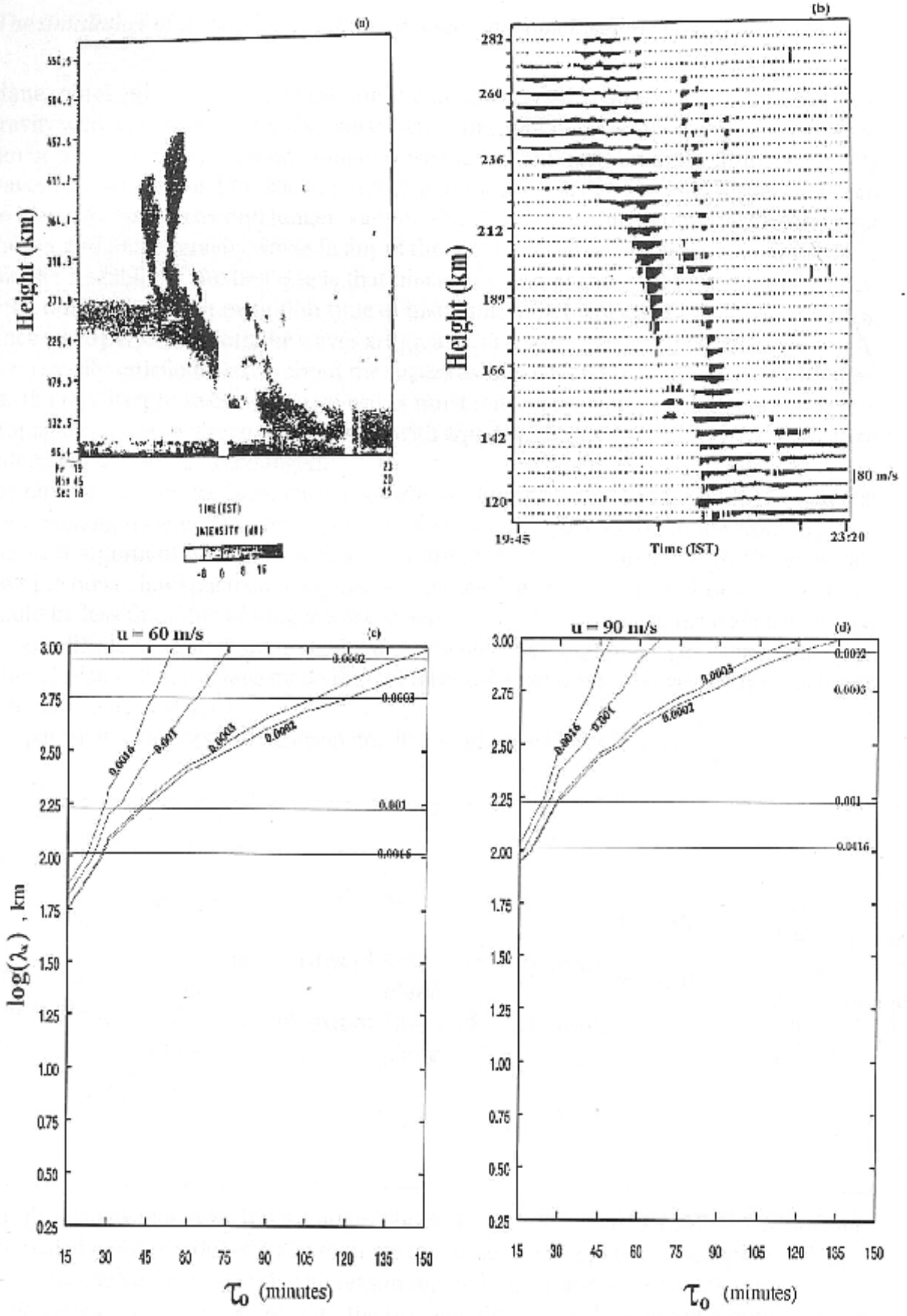

Figure 3.

plane, obtained by two equations, are the possible gravity waves. From fig. 3(c), two gravity waves of wavelengths 120, 600 km and time periods 22.5, 105 seconds respectively can be identified as shorter and longer wave modes. Similarly, from fig. 3(d), two gravity waves of wavelengths 175, 900 km and time periods 22.5, 120 seconds respectively can be identified as shorter and longer wave modes. It is interesting to observe that the both shorter and longer gravity waves in any of the plot fulfilled the two essential requirement for CRT instability. The first one is that phase of either of the waves must remain unaltered during the linear evolution time of instability which is in between 12-15 minutes. Since wave periods of both the waves are greater, al least by factor two, than it, the condition is easily satisfied. Next is about the superposition which must be coherent with time i.e. the relative phase between two waves must remain unchanged. Both chosen waves propagates in same direction, eastward, with equal velocities , $\frac{\omega_r}{k_x}$, thus the relative phase indeed would remain unchanged.

For our simulation, we have chosen shorter and longer wave modes with 100 and 600 km wavelengths which nearly matches the set of gravity waves identified from fig. 3(c). Our next argument is on the amplitudes of these two waves. Since the gravity wave follows the power law spectrum with negative indices, the amplitude of shorter wave mode would be less than that of longer wave mode. In our simulation we have always chosen the amplitude of shorter wave mode to be smaller than that of longer wave mode. Another choice which we have made is that amplitudes of both the waves are decreasing as they propagate eastward.

The parameters for both the chosen gravity waves are enlisted below.

λ_1	λ_2	a_1	a_2	$\psi_2 - \psi_1$	E_{xo}
100 km	600 km	1.0% in eastward plane 3.0% in westward plane	9.0% in eastward plane 12% in westward plane	295-135	case I (in 1(b) but extended till 2400 seconds with same slope.)

Another choice which we have made is about the electron density profile. The bottomside scale height is reduced to 5 km in present case compared to 15 km with which previous cases were investigated. The reason for such reduction is to reduce the width (altitude extent) of the BM. In fig. 4(a), the iso depletion and enhancement contours along with velocities are plotted while in fig. 4(b), the isodensity contours along with velocities are plotted at 2100 seconds. The two depletions penetrating to the topside are seen in fig. 4(a) similar to the observed first two rising plumes in fig. 3(a). The next two depletions are 70 % and 30 % depleted but moving downward. They ride over the enhancement layer which clearly has descending morphology after the first two rising depletions. Moreover just beneath to the 70 % deplered region, the enhancement structure move downward with 60 m/s. These features are very similar to the observation by Patra et al [69] in fig.

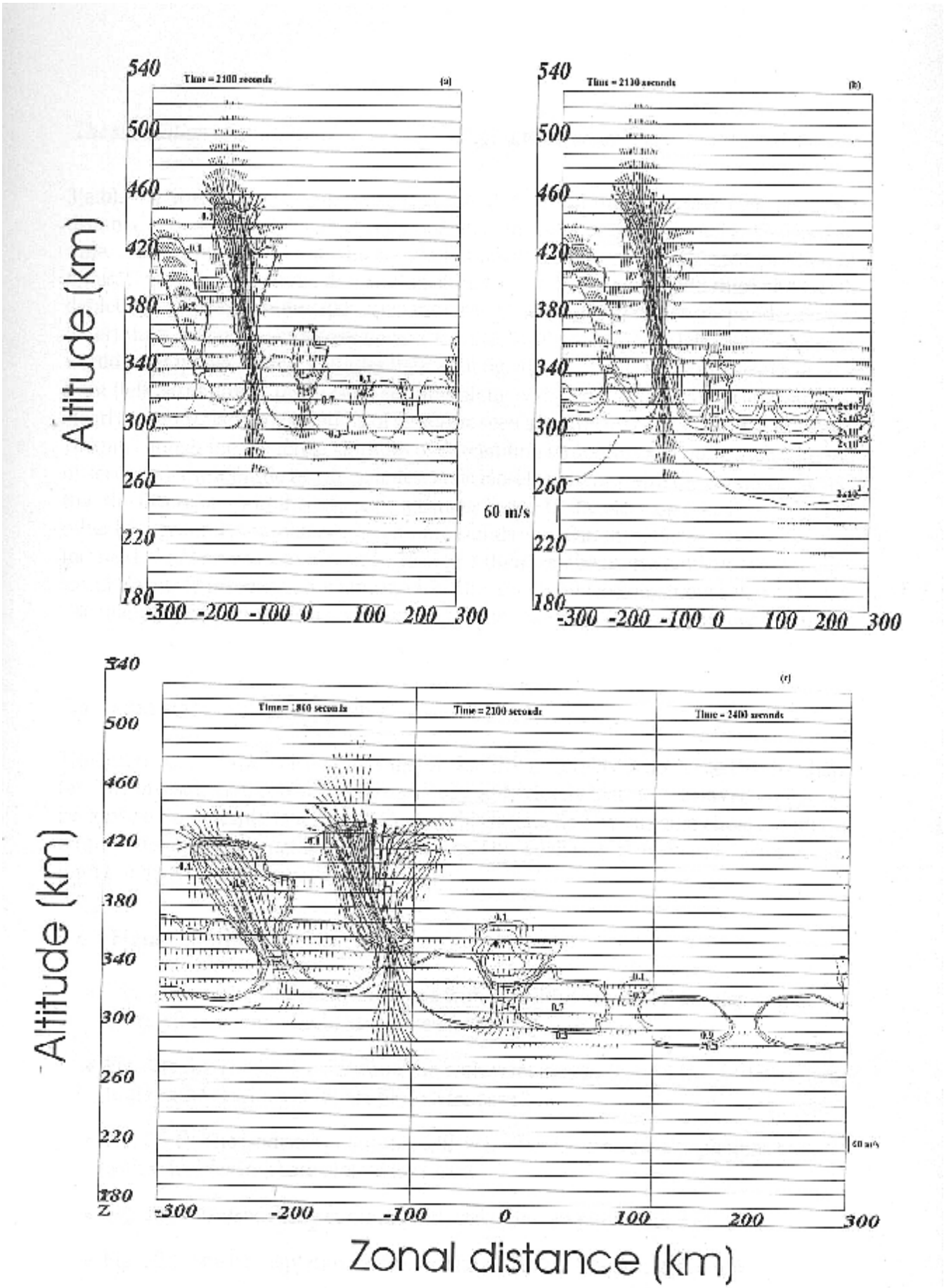

Figure 4.

3(a,b). We would like to emphasize that the plots reveal the structures over the zonal distance at one time while the observation gives the map over both zonal as well as over time. Thus one need to plot the simulation result for different zonal area at different times. If we assume that the descending enhancement layer along with third and fourth depletions are seen at time 2100s, then the structures left (right) to it correspond to earlier (later) time. Since F layer moves downward after 1500 seconds, the left (right) structure would be at higher (lower) altitudes than as in fig. 4(a-b). In fig. 4(c) we have plotted the right (left) structure at 1800 (2400) seconds along with centered structures at 2100s. We clearly see the relative descending of structure seen after the first two rising depletions by 70 km. Though the reference altitudes of descending structure does not match with the observation, the altitude by which it descends closely matches with observation. We feel that the discrepancy in the reference altitudes is due to the electron density profile and other background parameters taken for the simulation. Our investigation is restricted to interaction of two wave modes only. However there can be more than two wave modes simultaneously present in the ionosphere. The interaction among them self would give rise many other interesting features which are not emerged from present investigation.

5.5 summary and conclusion

The interaction of two wave modes under the CRI instability is discussed in the chapter. The investigation reveal that morphology and velocity features observed on few occasions could be explained on the view of this interaction by suitable choice of phase, amplitudes and wavelengths of the two waves. One such case is dealt and the results are found to match the observations closely.

5.6 Figure captions

- Fig. 2(a,b): The isodensity contours with velocities in (a) and iso-depletion contours with velocities in (b) are plotted for case 1.
- Fig. 2(c,d): The isodensity contours with velocities in (c) and iso-depletion contours with velocities in (d) are plotted for case 2.
- Fig. 2(e,f): The isodensity contours with velocities in (e) and iso-depletion contours with velocities in (f) are plotted for case 3.
- Fig. 2(g): The isodensity contours with velocities are plotted for case 4.
- Fig. 2(h): The iso-depletion contours with velocities are plotted for case 5.
- Fig. 2(i-l): The isodensity contours with velocities are plotted for case 6-case 9 respectively.
- Fig. 3 (a-d): The RTI map and RTV map observed by Patra et al; [69] are reproduced in (a) and (b) respectively. The gravity wave dispersion relation for $u_x = 60$ m/s in (c) and 90 m/s in (d) is plotted in frequency-zonal wavelength plane.

- Fig. 4(a-c): The iso-depletion contours with velocities in (a) and isodensity contours with velocities in (b) are plotted for case study. In (c), the depletion-enhancement contours are plotted at three different times such that left most, center and right most simulation plane correspond to 1800, 2100 and 2400 seconds.

Conclusions and Future Outlook

In conclusion, this thesis reports the effects of different background conditions on the ESF. After the introduction, first two chapters unfold few aspects regarding the role of different ion compositions on GRT instability. In particular the role of NO^+ and Fe^+ ions are discussed. It is found that the significant NO^+ ions can be transported to the topside by GRT instability in spit their small life time. However, the supply to the topside depends on the background conditions like ions compositions on the bottomside and the seeding wavelengths. The results are close in agreement with the observations. In chapter 3 some of the aspects like multiwavelength morphology and downdrafting of plasma bubbles generated by GRT instability are emerged from our observation of 2.8-m scale size irregularities associated with ESF. These aspects are discussed there on the basis of existing theories which reveal that more than one wave mode is essential to explain them. In last chapter, these aspects are simulated under nonlinear analysis. The investigation reveal that different forms of seeding perturbations can give rise different morphology of ESF. More than one wave mode is found to be essential for making the depletions to move downward with very large velocities.

The dynamics of the plasma bubble depends on the number densities [84] of background topside ionosphere. Further, the transition from dominant O^+ to dominant H^+ ions occurs in the topside of F-region of ionosphere beyond 650 km. On the basis of our investigation of GRT instability with molecular ions, we expect that the large mass ratio of these ions can give rise interesting dynamical aspects of *ESF* irregularities. This requires further investigation. Further, the VHF radar observations reveal the connection between E-region $\mathbf{E} \times \mathbf{B}$ instability and F-region instabilities. Moreover in the E-region the dominant ions are molecular ions. Thus the present numerical simulation model for F-region in the presence of two ionic species must be extended to accommodate the dynamics of E-region as well as the H^+ ions on the topside.

References

[1] Aggson T.L., Burke W.J., Maynard N.C., Hanson W.B., Anderson P.C., Slavin J.A., Hoegy W.R. and Saba J.L., 1992b, *J. Geophys. Res.*, **97**, 8581.

[2] Anderson D.N. and Haerendel G., 1979, *J. Geophys. Res.*, **84**, 4251.

[3] Anderson D.N. and D.W. Rusch, 1981, *J. Geophys. Res.*, **85**, 569.

[4] Balsley B.B., G. Haerendal and R.A. Greenwald, 1972, *J. Geophys. Res.*, **77**, 5625.

[5] Basu S., S. Basu, J. Aarons, J.P. McClure and M.D. Cousins, 1978, *J. Geophys. Res.*, **83**, 4219.

[6] Basu S., J.P. McClure, S. Basu, W.B. Hanson and J. Aarons, 1980, *J. Geophys. Res.*, **85**, 5119.

[7] Bernhardt P.A., M.B. Pongratz, S.P. Gary and M.F. Thomsen, 1982, *J. Geophys. Res.*, **87**, 2356.

[8] Booker H.G. and H.W. Wells, 1938, *Terres. Magn.*, **43**, 249.

[9] Bowles K.L., 1958, *Phys. Rev. Lett.*, 1, 454.

[10] Brinton H.C., H.G. Mayr and G.P. Newton, 1975, *Eos. Trans. AGU*, **56**, 1038 .

[11] Cahndrasekhar S., 1970, *Hydrodynamic and Hydromagnetic stability*, Clarendon Press.

[12] Chaturvedi P.K. and P.K. Kaw, 1976, *J. Geophys. Res.*, **81**, 3257.

[13] Chiu Y.T. and J.M. Straus, 1979, *J. Geophys. Res.*, **84**, 3283.

[14] Costa E. and Kelley M.C., 1978a, *J. Geophys. Res.*, **83**, 4359.

[15] Costa E. and Kelley M.C., 1978b, *J. Geophys. Res.*, **83**, 4365.

[16] Dungey, 1956, *J. Atmos. and Terr. Phys.*, **9**, 304.

[17] Farley D.T., Balsley B.B., Woddman R.F. and McClure J.P., 1970, *J. Geophys. Res.*, **75**, 7199.

[18] Fejer B.G., 1981, *J. Atmos. and Terr. Phys.*, **43**, 377.

[19] Fejer B.G., L. Scherliess and E.R. de Paula, 1999, *J. Geophys. Res.*, **104**, 19859.

[20] Fejer B.G., E. Kudeki and D.T. Farley, 1985, *J. Geophys. Res.*, **90**, 12249.

[21] Gary S.P., 1980, *Phys. Fluids.*, **23**, 1193.

[22] Gary S.P. and M.F. Thomsen, 1982, *J. Plasma Phys.*, **28**, 551.

[23] Gary S.P., P.A. Bernhardt and T.E. Cole, 1983, *J. Geophys. Res.*, **88**, 2103.

[24] Haerendel G., Lust R. and Rieger E., 1967, *Planet. Space. Sci.*, **15**, 1.

[25] Haerendel, 1973, Theory of equatorial spread F, Unpublished report, Max-Plank Institut fur Physik and Astrophysik, Garching, F.R.G.

[26] Hanson W.B. and S. Sanatini, 1970, *J. Geophys. Res.*, **75**, 5503.

[27] Hanson W.B. and S. Sanatini, 1971, *J. Geophys. Res.*, **76**, 7761.

[28] Hanson W.B., D.L. Sterling and R.F. Woodman, 1972, *J. Geophys. Res.*, **77**, 5530.

[29] Hanson W.B., B.L. Cragin and A. Dennis, 1986, *J. Atmos. and Terr. Phys.*, **48**, 205.

[30] Heelis R.A., P.C. Kendall, R.J. Moffet, D.W. Windle and H. Rishbeth, 1974, *J. Geophys. Res.*, **21**, 743.

[31] Hildebrand P.H. and R.S. Sekhon, 1974, *J. Appl. Meterol.*, **13**, 808.

[32] Hines, C.O., 1974, *Geophys. Monogr. Ser., AGU*, **18**.

[33] Huang C.S. and M.C. Kelley, 1996, *J. Geophys. Res.*, **101**, 283.

[34] Huang C.S. and M.C. Kelley, 1996, *J. Geophys. Res.*, **101**, 293.

[35] Huang C.S. and M.C. Kelley, 1996, *J. Geophys. Res.*, **101**, 303.

[36] Huang C.S. and M.C. Kelley, 1996, *J. Geophys. Res.*, **101**, 24521.

[37] Huba J.D., P.K. Chaturvedi, S.L. Ossakow and D.M. Towle, 1978, *Geophys. Res. Lett.*, **5**, 695.

[38] Huba J.D. and S.L. Ossakow, 1979, *J. Geophys. Res.*, **84**, 6697.

[39] Huba J.D., P.A. Bernhardt, S.L. Ossakow and S.T. Zalesak, 1996, *J. Geophys. Res.*, **101**, 24553.

[40] Huba J.D. and S.L. Ossakow, 1981a, *J. Geophys. Res.*, **86**, 829.

[41] Hudson M.K. and C.F. Kennel, 1975, *J. Geophys. Res.*, **80**, 4581.

[42] Hysell D.L, M.C. Kelley, W.E. Swartz and D.T. Farley, 1994, *J. Geophys. Res.*, **99**, 15085.

[43] Hysell D.L, M.C. Kelley, W.E. Swartz, R.F. Pfaff and C.M. Swenson, 1994, *J. Geophys. Res.*, **99**, 8827.

[44] Hysell D.L., Seyler C.E. and Kelley M.C., 1994, *J. Geophys. Res.*, **99**, 8841.

[45] Hysell D.L, M.C. Kelley, W.E. Swartz and R.F. Woodman, 1990, *J. Geophys. Res.*, **95**, 17253.

[46] Jaychandran B. et al, 1993, *J. Geophys. Res.*, **98**, 13741.

[47] Kelley M.C. et al, 1976, *Geophys. Res. Lett.*, 3, 448.

[48] Kelley M.C., M.F. Larsen, C. LaHoz and J.P. McClure, 1981, *J. Geophys. Res.*, **86**, 9087.

[49] Kelley M.C., Livingstone R.C., Rino C.L. and Tsunoda R.T., 1982, *J. Geophys. Res.*, **87**, 5217.

[50] Kelley M.C., 1989, The Earths ionosphere: Plasma physics and electrodynamics, Academic press.

[51] Kelley M.C. et al, 1986, *J. Geophys. Res.*, **91**, 5487.

[52] Keskinen M.J., S.L. Ossakow, E.P. Szuszczewicz and J.C. Holmes, 1981, *J. Geophys. Res.*, **86**, 5785.

[53] Kherani E.A., R. Sekar and R. Raghavarao, 2001, *submitted in J. Atmos. and Solar Terr. Phys.*.

[54] Klostermeyer J., 1978, *J. Geophys. Res.*, **83**, 3753.

[55] Krishnamurthy B.V., 1966, *J. Geophys. Res.*, **71**, 4527.

[56] Kudeki E., S. Bhattacharyya and R.F. Woodman, 1999, *J. Geophys. Res.*, **104**, 28145.

[57] Kudeki E., B.G. Fejer, D.T. Farley and H.M Ierkic, 1981, *Geophys. Res. Lett.*, **8**, 377.

[58] Laakso H.T., Aggson L., Pfaff R.F. and Hanson W.B., 1994, *J. Geophys. Res.*, **99**, 11507.

[59] LaBelle J., M.C. Kelley and C.E. Seyler, 1986, *J. Geophys. Res.*, **91**, 5513.

[60] McClure J.P., W.B. Hanson and J.H. Hoffman, 1977, *J. Geophys. Res.*, **82**, 2650.

[61] Mendillo et al, 1992, *J. Geophys. Res.*, **97**, 13865.

[62] Namboothiri S.P., B. Jaychandran, N. Balan and P.B. Rao, 1988, *J. Atmos. and Terr. Phys.*, **50**, 1087.

[63] Narcisi R. and E.P. Szuszczewicz, 1981, *J. Atmos. and Terr. Phys.*, **43**, 463.

[64] Ossakow S.L. and Chaturvedi P.K., 1978, *J. Geophys. Res.*, **83**, 2085.

[65] Ossakow S.L., S.T. Zalesak, B.E. McDonald and P.K. chaturvedi, 1979, *J. Geophys. Res.*, **84**, 17.

[66] Ossakow S.L., 1981, *J. Atmos. and Terr. Phys.*, **43**, 437.

[67] Ott E., 1978, *J. Geophys. Res.*, **83**, 17 .

[68] Patra A.K., V.K. Anandan, P.B. Rao and A.R. Jain, 1995, *Radio Sci.*, **30**, 1159.

[69] Patra A.K., P.B. Rao, V.K. Anandan and A.R. Jain, 1997, *J. Atmos. and Terr. Phys.*, **59**, 1633.

[70] Raghavarao R. et al, 1987, *J. Atmos. and Terr. Phys.*, **49**, 485.

[71] Raghavarao R., R. Sekar and R. Suhasini, 1992, *Adv. Space. Res.*, **12**, 227

[72] Raghavarao R. et al, 1999, *J. Atmos. and Solar Terr. Phys.*, **61**, 607.

[73] Rao P.B. et al, 1995, *Radio Sci.*, **30**, 1125.

[74] Rao P.B. et al, 1997, *Radio Sci.*, **32**, 1215.

[75] Rino C.L. et al, 1981, *J. Geophys. Res.*, **86**, 2411.

[76] Rishbeth H. and O.K. Garriot, 1969, Introduction to Ionospheric physics, Academic press.

[77] Rosenbluth M.N., N.A. Krall and N. Rostokar, 1962, *Nucl. Fusion. Supplement*, **143**, .

[78] Rottger J., 1973, *J. Atmos. and Terr. Phys.*, **35**, 1195.

[79] Rottger J., 1976, *J. Atmos. and Terr. Phys.*, **38**, 97.

[80] Rottger J., 1978, *J. Atmos. and Terr. Phys.*, **40**, 1103.

[81] Scannapieco A.J. and Ossakow S.L., 1976, *Geophys. Res. Lett.*, **3**, 451.

[82] Sekar R., R. Raghavarao, 1987, *J. Atmos. and Terr. Phys.*, **49**, 981.

[83] Sekar R., R. Suhasini and R. Raghavarao, 1994, *J. Geophys. Res.*, **99**, 2205.

[84] Sekar R. and R. Raghavarao, 1995, *Geophys. Res. Lett.*, **22**, 3255.

[85] Sekar R., R. Suhasini and R. Raghavarao, 1995, *Geophys. Res. Lett.*, **22**, 885.

[86] Sekar R., R. Sridharan and R. Raghavarao, 1997, *J. Geophys. Res.*, **102**, 20063.

[87] Sekar R. et al, 2000 *Indian Journal of Radio and Space Physics*, **29**, 262.

[88] Sekar R. and M.C. Kelley, 1988, *J. Geophys. Res.*, **103**, 20735.

[89] Sekar R. and E.A. Kherani, 1999, *J. Atmos. and Solar Terr. Phys.*, **61**, 399.

[90] Sekar R., 1991, Ph. D. thesis.

[91] Sekar R., E.A. Kherani, P.B. Rao and A.K. Patra, 2001, communicated in *J. geophys. res.*

[92] Simon A., 1963, *Phys. Fluids.*, **6**, 382.

[93] Sinha H.S.S., Shikha Raizada and R.N. Misra, 1999, *Geophys. Res. Lett.*, **26**, 1669.

[94] Spitzer L, 1962, *Physics of Fully Ionized Gases*, Interscience, New York.

[95] Sridharan et al, 1997, *J. Atmos. and Terr. Phys.*, **59**, 2051.

[96] Szuszczewicz E.P., 1978, *J. Geophys. Res.*, **83**, 2665.

[97] Szuszczewicz E.P., R. Tsunoda, R.T. Narcisi and J.C. Holmes, 1980, *Geophys. Res. Lett.*, 7, 537.

[98] Tsunoda R.T. and D.P. Towle, 1979, *Geophys. Res. Lett.*, **6**, 873.

[99] Tsunoda R.T., 1980, *J. Atmos. and Terr. Phys.*, **42**, 743.

[100] Tsunoda R.T., 1981, *J. Geophys. Res.*, **86**, 139.

[101] Tsunoda R.T. and B.R. White, 1981, *J. Geophys. Res.*, **86**, 3610.

[102] Tsunoda R.T., 1982, *J. Geophys. Res.*, **87**, 712.

[103] Tsunoda R.T., R.C. Livingston, J.P. McClure and W.B. Hanson, 1982, *J. Geophys. Res.*, **87**, 9171.

[104] Tsunoda R.T., R.C. Livingston and C.L. Rino, 1981, *Geophys. Res. Lett.*, **8**, 807.

[105] Weber E.J., J. Buchau, H. Eather and S.B. Mende, 1978, *J. Geophys. Res.*, **83**, 712.

[106] Whitehead J.D., 1971, *J. Geophys. Res.*, **76**, 238.

[107] Woodman R.F., 1985, *Radio Sci.*, **20**, 1185.

[108] Woodman R.F and T. Hagfors, 1969, *J. Geophys. Res.*, 74, 1205.

[109] Woodman R.F and C. LaHoz, 1976, *J. Geophys. Res.*, **81**, 5447.

[110] Woodman R.F., Pingree J.E. and Swart W.E., 1985, *J. Atmos. and Terr. Phys.*, **47**, 867.

[111] Zalesak S.T., 1979, *J. Comput. Phys.*, **31**, 335..

[112] Zalesak S.T., Ossakow S.L., 1980, *J. Geophys. Res.*, **85**, 2131.

[113] Zalesak S.T., Ossakow S.L. and Chaturvedi P.K., 1982, *J. Geophys. Res.*, **87**, 151.

[114] Zergham S. and Seyler C.E., 1987, *J. Geophys. Res.*, **92**, 10073.